Two-Phase Eulerian Averaged Formulation of Entropy Production for Cavitation Flow

By

Joseph Sun

A Thesis Submitted in Partial Fulfillment of

The Requirements for the Degree of

Doctor of Philosophy

In

The Faculty of Graduate Studies

Department of Mechanical and Manufacturing Engineering

University of Manitoba

Winnipeg, Canada

Abstract

This research is focused on formulating a new model of entropy production for two-phase flow, including cavitating turbulent flow. In particular, it focuses on the following aspects of the fluid dynamics and the potential contribution of the model to fluid device design. It includes (i) developing a new turbulent entropy model, (ii) a new formula of entropy production rate for two-phase flow including cavitating turbulent flow based on the second law, (iii) applying the technique to study a NACA hydrofoil, and (iv) conducting associated performance analysis of a propeller using post-processing of the CFD results and demonstrating that entropy production of two-phase cavitating flow around the propeller can be correlated to the loss of power output.

The first stage consists of formulating the entropy production for laminar channel flow using Gibb's free energy. This model is validated through the analytically solved Navier-Stokes equations. Subsequently, the single-phase turbulent flow is formulated in a similar manner, but the validations are carried out by comparing the prediction of the model with DNS results. Then, the model of entropy production for two-phase turbulent flow is derived from Gibb's equation and a version of the Reynolds averaged Navier-Stokes (RANS) equations. The k- ε model is employed to represent the turbulent properties of single phase and two phase flows. A developed inter-phase slip algorithm mixture model is applied to control over coupling of phases. The Rayleigh-Plesset equation is used to model the rate of mass generation of vapour at the inter phase. The standard k-ε turbulence equations are used to describe turbulence in the cavitation flow.

The validations of CFD predictions include exploring the force and cavitation characteristics of the NACA 4412 hydrofoil section. The application of this entropy

production model in engineering design is presented via the comparisons between CFD results and the experimental data for the velocity distributions behind propeller P5168.

Contents

List of tables

List of figures

List of symbols, abbreviations and nomenclature

C	Mass fraction
C_a	Cavitation number
C_D	Drag coefficient
C_L	Chord length $[m]$
d_v	Diameter of vapour $[m]$
e	Internal energy [J]
D	Diffusion coefficient $[m^2/s]$
$\mathbf{g}$	Gravitational acceleration $[m/s^2]$
h	Length of half channel $[m]$
J	Advance ratio
k	Kinetic energy of turbulence $[m^2/s^2]$
K	Thermal conductivity $[W/(m \cdot K)]$
m	Mass $[kg]$
m_b	Rate of change of bubble mass $[kg/s]$
$\mathbf{M}$	Momentum source $[\mathbf{N}/m^3]$
N_B	Number of bubbles per unit volume
p	Pressure $[\mathbf{N}/m^2]$
p_v	Vapour pressure $[\mathbf{N}/m^2]$
$\dot{Q}$	Heat transfer rate $[W]$
Re	Reynolds number
t	Time $[s]$
U_∞	In flow speed $[m/s]$

U_x Normalized axial velocity $[m/s]$

U_t Tangential velocity $[m/s]$

U_r Radial velocity $[m/s]$

$\mathbf{u}$ Velocity $[m/s]$

$\mathbf{u}_{Il}$ Local instant velocity of liquid phase $[m/s]$

$\mathbf{u}_{Iv}$ Local instant velocity of vapour phase $[m/s]$

$\mathbf{u}_{Fl}$ Fluctuating component of the velocity of liquid phase $[m/s]$

$\mathbf{u}_{Fv}$ Fluctuating component of the velocity of vapour phase $[m/s]$

$\mathbf{u}_{l}$ Average velocity of liquid phase l $[m/s]$

$\mathbf{u}_{v}$ Average velocity of vapour phase v $[m/s]$

$\mathbf{u}_{lv}$ Velocity of vapour phase v relative to the liquid phase $[m/s]$

$\mathbf{u}_{m}$ Velocity of the mixture mass center $[m/s]$

$\mathbf{u}_{Ml}$ Diffusion velocity (liquid velocity relative to the mixture mass center) $[m/s]$

$\mathbf{u}_{Mv}$ Diffusion velocity (vapour velocity relative to the mixture mass center $[m/s]$

V_B Bubble volume $[m^3]$

V_c Control volume $[m^3]$

v''' Specific volume $[m^3/kg]$

w Surface velocity $[m/s]$

x Coordinate in horizontal direction

y Coordinate in vertical direction

Greek letters

α	Volume fraction
δ	Boundary thickness $[m]$
α_0	Angle of attack $[Degree]$
ε	Dissipation rate of turbulent kinetic energy $[m^2/s^3]$
μ	Dynamic viscosity $[kg/m \cdot s]$
μ_{Tm}	Mixture turbulent eddy viscosity $[kg/m \cdot s]$
μ_m	Dynamic viscosity for the mixture $[kg/m \cdot s]$
σ	Surface tension $[\mathbf{N}/m]$
ρ_l	Density of liquid $[kg/m^3]$
ρ_v	Density of vapour $[kg/m^3]$
$\boldsymbol{\tau}$	Stress tensor $[\mathbf{N}/m]$
Γ	Rate of mass transfer $[kg/m^3 \cdot s]$

Symbols and subscripts

B	Bubble
c	Control
D	Drag
l	Liquid
L	Length
m	Mixture
r	Radial
t	Tangent
T	Turbulent

v	Vapour
x	Normalized axial
Fl	Fluctuating liquid phase
Fv	Fluctuating vapour phase
Ll	Local liquid phase
Lv	Local vapour phase
lv	Vapour phase relative to liquid phase
Ml	Liquid relative to mixture
Mv	Vapour relative to mixture
Tm	Mixture turbulent

Acknowledgments

I am very grateful to many people who helped me in obtaining the Ph.D. First and foremost, I particularly thank my advisors, Dr. Greg Naterer and Dr. David Kuhn, for providing this great opportunity to work under their supervisions. Their valuable guidance in every stage of the research assisted me in completing this thesis. I am also grateful for the kindness and help of my former advisor, Dr. Dan Fraser, and express my condolences to his family on his death.

Many thanks also to the committee members, Dr. Chao Zhang, Dr. Jay Doering and Dr. Robert Derksen, for their helpful and valuable advices on thesis revision.

I thank my friend and mentor, Dr. Redwan Moqbel, for his continued encouragement, especially when I was discouraged. I do not mourn to his death but celebrate his glittering life.

I would also like to thank Blue Energy Canada, Inc., Martin Burger, and Jon Ellison for offering the computer facility for numerical simulations.

I want to thank my current supervisor, Kenneth Chin, the Senior Engineering Manager, at Emerson Process Management Valve Automation, who gave me continued encouragement and supported me through the final step.

Very special thanks to my wife, Hongling Deng, for her endless support and encouragement in what I have chosen to pursue.

Chapter 1

Introduction

1.1 Background

1.1.1 Efficient energy utilization

Over the past few decades, we have witnessed the growth of renewable energy. Along with the evolution of new energy sources, there has been a corresponding evolution of the technology for more efficient energy use to address the issue of the world's limited energy sources and environmental challenges; thus, efficient energy use has become increasingly important.

In the early days, engineers and researchers had to scrutinize thermal and mechanical energy systems or devices to achieve optimal design and possible improvement in as many aspects as possible. Later, conventional technology was adapted for generally identified energy losses on a system scale or a global scale, such as a single-loss coefficient, to attain desired energy efficiency.

As computer technology developed, the new computer-based technologies rapidly infiltrated the aspects of diverse industrial fields including thermal and mechanical energy systems. For example, commercial professional software for design optimization and numerical simulations have been developed and marketed. Those technological advancements have achieved great successes, but it is obvious that this impetus is pushing the limits of locally improving energy efficiency for existing devices.

More recently, advances in memory, processor, and parallel-computing technology have allowed computers to numerically solve large scale and complex partial differential equations. These equations are the cornerstones that the science of thermal

and fluid dynamics is built on. Particularly in the last few years, technological advances in hardware and software have opened a new way to explore more efficient energy use. Computer-Aided Design (CAD) and simulating programs are in wider use now more than ever. For examples, contemporary commercial Computer-Aided Engineering (CAE) packages provide a platform, on which, researchers and engineers can perform 3D modeling, mesh generating, and flow simulation to investigate the dynamic behavior and heat transfer of liquids and gases in extensive industrial applications. This tendency indicates that a more functional methodology for locating energy loss is essential and is possible with current computing power capable of highly parallel tasks. As a result, the emergence of new paradigms in energy saving is inevitable. This new technology developed in recent years is known as entropy-based design. Local entropy production is determined based on Computational Fluid Dynamics (CFD) results and this local entropy mapping is used to identify areas for system efficiency improvement. One of the examples of entropy based design is the application to systematically improving efficiency of fuel cells, since entropy production of both electrochemical and thermo-fluid irreversibilities can be formulated based on the second law [1].

1.1.2 Entropy and the second law of thermodynamics

The first and second laws of thermodynamics govern all processes of energy conversion and have become the main foundations for analysis of energy systems while playing different roles in thermodynamics. The first law addresses quantity of energy while the second law characterizes the quality of energy in terms of exergy since exergy is the maximum useful work which could be generated by the energy. The second law can be used to calculate phase transition properties, transport coefficients and entropy. In

a closed thermodynamic system energy can be exchanged between the system and its surrounding. But some of the thermal energy cannot be used to do work which entropy can be a tool quantifying amount of them. In a human-engineered or a natural life support system that facilitates the life of the biosphere in a sustainable manner, entropy can be an indicator of the life state. [2]. From the point of view of sociologists, the entropy-based measures of social and economic inequality can also be used to describe racial and income diversity, and social isolation [3].

In conjunction with the physical systems, entropy is related to other functions, including computational analysis of energy systems.

Entropy production identifies the instantaneous change in a particular position of the system over time. This concept has been mathematically formulated and has become a valuable and important parameter to assess irreversible losses locally, rather than globally. It is believed that entropy production provides a unique way of characterizing the energy efficiency of any thermo-fluid system or device. For a complex engineering system, a large rate of entropy production in a device would identify an area of concern. Those regions need to be treated in particular by designers for improvements. It is a commonly desired goal to improve a device's efficiency by reducing entropy production. This is the universally expected goal, regardless of applications, flow patterns or system conditions. The benefit of entropy has been widely presented in various applications especially in thermo science and fluid mechanics. It was recognized that entropy is more than just the irreversibility in a thermodynamic system.

1.1.3 CFD and entropy-based design

Newton's second law of motion combined with the first law of thermodynamics establish the foundation of fluid and thermal dynamics. From them, the Navier-Stokes momentum equations and the energy equation have been derived. This set of nonlinear partial differential equations describes the flow of fluids and energy. The motion of liquids and gases are handled by the equations on the macro-level with continuum in the structure. All variables are considered continuous functions of space coordinates and time. This mathematical model can be used to simulate the weather, atmospheric motion, ocean currents, water flow in the pipeline, and many other fluid-flow phenomena. To model entropy production, the required parameters must be obtained by solving the Navier-Stokes equations over the domain. These parameters may include velocity gradient, temperature gradient, kinetic energy dissipation, eddy viscosity, and so on. For multiphase flows that involve friction due to the relative velocity between phases and mass transfer resulting from phase change, more parameters are needed to account for the role of various factors on entropy production.

Reynolds-averaged Navier-Stokes (RANS) equations are the most broadly used approach to turbulent fluid flow modelling. The Reynolds stress term in the RANS equations must be modelled to close the RANS equation for solution. Numerous RANS based turbulence models have been proposed to solve the Reynolds stress term including algebraic models, one equation models and two equation models. Two equation turbulence models, such as the k-ε model and the k-ω model, are widely used for turbulence modeling. In this research, the k-ε model is chosen to model the turbulent two-phase flow. The k-ε model includes two extra transport equations to represent the

turbulent properties of the flow. The transported variables include turbulent kinetic energy and the kinetic energy dissipation rate. The second variable epsilon can be used for determining the scale of the turbulence including length scale or time scale.

With the development of high-speed computers, the RANS differential equations have been numerically solved using a variety of discrete methods including an element-based finite volume method for discretizing the spatial domain to a mesh. The mesh constructs the finite volumes used to conserve relevant quantities such as mass, momentum, and energy. This area of study is called computational fluid dynamics (CFD). CFD numerically solves the equation set, and the solutions are given in the form of data. The data files can be obtained from CFD post-processing, thus the entropy production, according to the developed entropy model can be determined in the whole domain of predicted flow or temperature. CFD post-processing is designed to allow easy visualization and quantitative analysis of the simulation results, thereby plotting the entropy production. Aimed at minimizing loss of work, one of the new technologies is entropy based design which serves a function allowing engineers to modify locally a device's geometries or structure and improve overall performance. For a multi-objective genetic algorithm, an entropy-based design is based on an application of concepts from the statistical theory of gases [4]. The design of a two-bar truss and a speed reducer demonstrated the effectiveness of the methodology [4].

1.1.4 Application in entropy-based design

One application of entropy-based design is marine propellers, which transmits power by converting rotational motion into thrust. A pressure difference established between the forward and rear surfaces produces the thrust; consequently, a fluid is

accelerated behind the blade. For marine propeller optimization problems, the main goal is to achieve the highest energy efficiency. While blades are the dominant factors in a propeller's performance, it is not possible to successfully develop an optimal design by analytical methods alone because of complexity of the flow field. The objective function is difficult to define analytically because of the 3-D curved blade surfaces and equations of fluid mechanics in terms of rotating blades. In addition, a large number of design variables of interest for optimization lead to a problem that is expensive and computationally intensive. The technique of entropy-based design of propellers can be considered a new optimization method. This method has more potential advantages than a conventional objective function method in dealing with such problems. It can potentially offer a useful new way of higher system efficiency in local entropy production mapping. Using entropy-based mapping for the visualization of "problem areas," the technique gives an intuitive visualization that can provide unique insight into the real optimum design process. Consequently, it can capture promising regions of modification and efficiently identify the optimum local design. Along with an application of CFD solvers, the technique provides an opportunity to explore the geometry of many numerical techniques and obtain the solution without applying mathematical algorithms.

Because the marine propeller operates in flow conditions in which high velocity and low pressure coexist, cavitation can occur behind the blades. This type of cavitation is significant because it restricts the speed at which the propeller can be operated. For effective operation of the marine propeller, highly efficient performance should be achieved while limiting or eliminating cavitation. Developing a model that predicts entropy production in two-phase flow (including cavitating flow) can provide propeller

designers with an efficient methodology to scrutinize flow irreversibility locally, rather than globally. The entropy-based design method can actively incorporate the local rates of entropy production for design modifications of the propeller.

1.2 Objectives

This study examines the role of entropy production and the second law in the development of new design tools to improve fluid machinery performance. It aims to relate entropy production to the local losses and energy efficiency of the system. Entropy-based design for two-phase flow has promising potential in a variety of engineering systems, but no previous models of turbulent entropy production in two-phase flows have been developed.

The objectives of this study are as follows:

1) Development of new turbulent entropy models incorporating dissipation due to eddy viscosity;
2) Formulation of a new model of entropy production for two-phase flow, including cavitating turbulent flow;
3) Application of the new entropy production models to study a NACA 4412 hydrofoil; and
4) Conduct associated performance analysis of a propeller using post-processing of the CFD.

1.3 General approach

Relevant entropy and fluid machinery and cavitation literature is reviewed in Chapter 2. In Chapter 3, the Eulerian averaging method with two-phase flow analysis for the basic governing equations is presented. Consequently, the fundamental

thermodynamic relation of entropy is introduced. The governing equations for the two-phase flow include continuity and momentum equations for the mixture model along with the slip velocity algebra equation.

In Chapter 4, the entropy production for laminar channel flow using Gibb's free energy is presented. This model is validated through the analytically solved Navier-Stokes equations. Subsequently, the new predictive model of entropy production for two-phase flow is formulated in terms of the time-averaged governing and constitutive relations. The validations are carried out by comparing the prediction of the model with DNS results.

In Chapter 5, the model of entropy production for two-phase turbulent flow is derived from Gibb's equation and Reynolds averaged Navier-Stokes (RANS) equations. A developed inter-phase slip algorithm mixture model is applied to control over coupling of phases. The Rayleigh-Plesset equation is used to model the rate of mass generation of vapour at the inter phase. The standard k-ε turbulence equations are used to describe turbulence in the cavitation flow. The validations of CFD predictions include exploring the force and cavitation characteristics of the hydrofoil NACA 4412 section.

In Chapter 6, the application of this entropy production model in engineering design is demonstrated via the comparisons between CFD results and the experimental data for the velocity distributions behind propeller P5168.

1.4 Significance of this study

Currently, there are no mathematical models of entropy production for two-phase flow, including cavitation flow, and relatively few studies exist on the improvement of

operation of kinetic turbines by using an entropy-based design method. The formulation of entropy production in two-phase flow (including cavitation flow) could be a new milestone in fluid dynamics. The mathematical model will reveal the mechanism of entropy production due not only to the dynamic and eddy viscosity but also to the phase relative velocity and mass transfer. In addition, the applications in entropy-based design will demonstrate the new design paradigm in both engineering and academics to enhance the optimum design opportunity and improvement possibilities. This is a significant contribution using the second law of thermodynamics which affects not only the advanced fluid mechanics learned by graduate students but also acquisition of advanced design skills and knowledge for experienced engineers and project decision makers who have worked for many years in mechanical engineering and energy industry. This research identifies important areas in which fundamental knowledge should be updated.

The goal of the research is to formulate a general theory of entropy production in a mathematically usable form, making it available to the field of fluid dynamics with sufficient accuracy to help students and engineers better understand the second law of thermodynamics and develop academic and design skills in the mechanical engineering and energy sector. The output of this study is mathematical formulas that can be used to estimate local loss for both single-phase turbulent flow and two-phase cavitation flow. The case study of entropy-based design combined with CFD will expose the power of this new technology. The four most significant contributions to this work are:

1) The development of two new turbulent entropy production models that account for eddy viscosity more precisely;
2) The development of a two phase entropy production model that can be used to

improve fluid machinery performance;

3) Demonstration and validation of the two phase entropy model to NACA 4412 hydrofoil and propeller P5168; and
4) Concise set of the equations for use in local entropy based design.

The derivation of these equations for entropy production in two-phase flow is considerably more complicated than that of single-phase flow due to the unknown position of the liquid-vapor interface. The difficulties originate from the complex nature of two-phase flow arising from the existence of multiple, deformable, and moving interfaces and discontinuities of fluid properties and complex flow patterns near the interface.

Chapter 2

Literature review

2.1 Entropy and the second law

The first law of thermodynamics states that the total energy of an isolated system is constant; energy can be transformed from one form to another, but cannot be created or destroyed. The first law characterizes energy conservation associated with all systems. However, it does not indicate that energy conversion has a preferred direction. This direction is characterized through the second law of thermodynamics and entropy. The second law of thermodynamics states that the entropy of an isolated system does not decrease. Carnot made the original statement that losses of moment of activity exist in any machine due to accelerations and shocks of moving components [5]. A change in entropy in a system can be defined as the transfer of heat across a boundary, divided by the equilibrium temperature of the system [6].

Entropy production characterizes a loss of mechanical energy from a system through dissipation or friction. The lost energy reduces the amount of useful work that can be performed [5]. Entropy production has a key role in the thermodynamics of irreversible processes because it affects the performance of thermal systems [7]. The importance of reduction of entropy production was recognized by Carnot, who conceived an ideal engine in which heat converted to work could be rolling back by reversing the motion of the cycle [8]. However, Carnot cycle reversibility cannot be realized by an actual heat engine.

Clausius first used the term *entropy* and indicated that, in any irreversible process, a small quantity of heat is incrementally dissipated across the system boundary [9]. This

concept can be stated and expressed in a brief way. In reality, once the thermodynamic state of a system and its surroundings has been changed, it cannot be accurately reinstated to the initial state without doing work. This is an irreversible process which increases the entropy of the system. The second law of thermodynamics indicates which processes are possible. [10].

Boltzmann introduced a statistical perspective of entropy, in which entropy was defined as a measure of disorder. The second law expresses that disorder tends to increase [11]. Later, statistical entropy was defined by the Gibbs entropy formula [12]. James Maxwell then presented a hypothetical concept of entropy in relation to the second law. This model of entropy persisted throughout the development of statistical and quantum physics, information theory, and computer science [13].

Further, Lucia clarified irreversibility through observation of the phenomena. In a thermodynamic system, if the molecules interacted each other shift from one state to another, the arrangement of the atoms and molecules will change and cannot be predicted [14]. A certain amount of energy must be used to do work for the state transformation of the molecules or atoms [15]. This transformation will lead to a certain amount of thermal heat loss or dissipation due to the friction and collisions between the molecules or atoms and the lost energy will no longer be recovered.

The foundations of the second law of thermodynamics are based on statistical thermodynamics of intermolecular exchange. Its influence, however, extends from the microscopic scale to the macroscopic scales of engineering systems, even the environment and the earth. Dincer presented a detailed study that outlines the key role of exergy, or the energy which can perform useful work in environmental sustainability of

energy systems [16]. Rosen and Dincer indicated that the environmental impact of waste emissions and power generation systems can be effectively characterized by methods of exergy analysis [17]. At the microscopic level, a close relationship exists between the concepts of entropy and probability [11]. The concavity property of entropy is directly related to a given probability distribution function for a fluid. The Clasius–Duhem inequality represents the irreversible increase of entropy as determined by the second law of thermodynamics. It is a supplemental equation in the analysis of fluid mechanics [1]. By relating entropy directly to a probability distribution function, one can show that a non-equilibrium version of the entropy function (and a modified Clasius–Duhem inequality) can be obtained.

From a statistical view, entropy and probability are closely related. Jaynes asserts that probability is logic of science so that the probability theory is far more useful as it fundamentally expresses logical interference pertaining to individual cases. [18]. Applying the questions or problems from one scientific field, in terms of concepts and principles, to another field can be useful and helpful. Such issues include establishing criteria for numerical techniques based on physical principles in the logical framework of probability theory, as well as deriving practical mathematical expressions and formulae for implementing the results. Because kinetic theory uses many concepts and principles of probability and statistics, a wealth of ideas are available from this field and they can serve as inspiration for other applications [1].

Today entropy has a vital role in our understanding of many diverse phenomena. Its importance is evident in different areas, such as the use of energy and the source of order and complexity in nature [19]. It serves as a foundation for formulations of

engineering fluid mechanics, thermodynamics, information, coding theory, economics, and biology [1]. Watanabe realized entropy minimization is a powerful pattern recognition tool associated with the principle of simplicity [20]. Sasaki et al. have shown a transform process of the eigenvectors from the second moment of the spectroscopic data into a set of vectors [21], based on solving Shannon's entropy minimization problem [22]. Zhang studied discrete spectra and mass spectra by using an entropy minimization algorithm to reconstruct pure component spectra from mixture spectra [23]. Furthermore, Waele investigated cryocoolers and related thermodynamic systems based on the first and second laws of thermodynamics using enthalpy flow, entropy flow, and entropy production. These systems and machines use an oscillating gas flow [24]. In addition, Johannessen and Kjelstrup applied optimal control theory by taking temperature of the cooling/heating medium as the variable to minimize the entropy production rate in plug flow reactors [25]. Finally, Røsjorde minimized the total entropy production of a process for dehydrogenation of propane. This work showed that entropy production can be effectively used as an objective function in chemical engineering process optimization studies [26].

Kapur and Kesavan provided a comprehensive and detailed procedure for generalized entropy optimization principles [27]. Bejan presented a method of entropy generation minimization for thermodynamic optimization and design [28]. Moorhouse and Hoke [29] used entropy in designing a complete flight vehicle by considering an integrated propulsion system. The work involved exergy and thermo-economics in a system-level analysis. By doing the analysis of exergy, the gap between maximum exergy and the actual work which is involved in a series of steps of energy exchange can be

examined [30]. Consequently, the exergy values can be used to estimate the efficiencies of the systems and the irreversibilities or during the energy conversion process [31], [32]. Entropy equations can be constructed in different way but relating the equations to exergy may have other benefits [33]. Camberos asserted that the degradation of work potential stemmed from irreversible losses can be expressed in terms of units of energy, which may have a more straightforward interpretation [34], [35]. Singh presented new entropy-based techniques for parameter estimation in hydrology, particularly probability distribution functions applied in water science [36]. Further, Cervantes and Solorio investigated entropy generation in a plane turbulent jet [37]. An extra term was added to Bejan's analysis to account for the experimentally observed oscillations [28]. Johannessen presented a theoretical proof that entropy production from heat exchange in a heat exchanger could be minimized when local entropy production is constant in all parts of the system [38]. The solution for attaining the minimum is independent of the value of the heat transfer coefficient.

Entropy generation minimization (EGM) is an analytical method for second law analysis which involves fluid mechanics, heat transfer, material constraints, and geometry to obtain relations between entropy generation and the optimal configuration. By carrying out EGM, a mathematical expression of the entropy production rate for certain physical process needs to be derived [39], [40]. Then the conventional optimization methods like calculus can be used for finding the extremum that corresponds to a minimum entropy generation. Since the application of analytical methods for obtaining the extremum are often limited to simple geometries and flow patterns, Naterer extended analytical EGM to

numerical and experimental methods of analysis [1]. Kapur and Kesavan generalized a procedure in detail for generic entropy optimization principles [27].

2.2 Use of CFD with the second law

As numerical methods and algorithms behind CFD (Computational Fluid Dynamics) improve and computing become increasingly fast, it is possible to emerge applications in design of engineering thermo fluid system in terms of the second law [33]. For complex problems and geometries, CFD is a design tool that enhances and improves the optimization of second-law-based design because entropy production can be obtained by post-processing of the predicted flow fields [41]. The combination of EGM with CFD is an emerging technology for design optimization. As an application, in order to identify the entropy generation rates related to the fluid friction and irreversibility of heat transfer, Natalini and Sciubba took FEA and two-equation turbulence model solving the Navier–Stokes equations and the energy equations for the design of blades for a gas turbine [42]. Furthermore, the distribution of the key parameters in the flow field for pitched turbine blades [43] can be plotted using a CFD post processor to identify regions of high local losses, thereby leading engineers to modify the blade profile to reduce the entropy rate. Prediction of entropy production rate involved a wide range of applications, such as laminar and turbulent flow through a smooth duct [44], [45], [46], mixed convection in a vertical channel with transverse fin arrays [47], free convection in inclined enclosures [48], flow in concentric cylinder annuli with relative rotation [49], and diffusers [50]. These studies are examples of how entropy production computations can successfully complement CFD technology.

The flow problems in industrial application usually involve turbulent flow. Moore and Moore numerically solved the turbulent flow to predicting entropy production. This work was considered as the first development of a numerical model for entropy production in turbulent flow [51]. The mean local entropy production in an elbow can be predicted using Moore's model [52]. Also a turbulent plane oscillating jet [37], and a jet impinging on a wall [53] have been successfully resolved with the model. Based on the time-averaged turbulence equations, Kramer-Bevan used another method, the finite volume method to predict the entropy production in turbulent flows associated with mean viscous dissipation [54].

Entropy production can be interpreted alternatively in computational terms, including physical process like heat transfer and viscous dissipation. Due to lack of oscillations, uniqueness, and other unusual behavior of numerical procedures, solutions of differential equations might not satisfy an entropy condition [55], [56], and numerical procedures may also produce or destroy entropy through many factors such as discretization errors, and nonphysical numerical results [57], [58]. Those included several significant works done by researchers. For example, Cox and Argrow used a finite difference method to compute the local loss for compressible flow [57]. Jansen [59] and Hauke [60] carried out an entropy based stability analysis to turbulent flows. Jansen took a linear combination of equations to solve the Navier–Stokes equations for compressible flow and presented an entropy inequality [59]. Due to the solution sensitivity to variables with the numerical algorithm [58], it was difficult to evaluate the quality of results whether or not agree with reality.

As a valuable design tool, CFD is used for the analysis of thermal/fluid systems. This present study uses post-processed results from CFD to determine and analyze entropy production throughout a flow field. Past entropy studies using numerical methods involving various geometries and flow conditions have been conducted by various researchers. Ko and Cheng reported numerical investigation of entropy generation for developing laminar forced convection in a wavy channel [61]. Herpe analyzed the entropy production rate taking 3D unsteady laminar flow for longitudinal vortex generators on the fins of a compact heat exchanger [62]. Ko used CFD to investigate three-dimensional laminar forced convective flow and entropy generation in a 180^{o} curved rectangular duct with longitudinal ribs on the heated wall [63]. The development of secondary vortices, temperature, and local entropy generation distributions as well as overall entropy generation, including the entrance and fully developed region, were analyzed.

Furthermore, Kock and Herwig analyzed systematic entropy production in incompressible turbulent shear flows of Newtonian fluids, incorporating it into a CFD code [64]. Based on asymptotic wall functions, the four different mechanisms of entropy production were developed: dissipation in a mean and fluctuating velocity field; and heat flux in a mean and fluctuating temperature field.

Entropy production is usually enhanced in turbulence with variation of fluid density. Compressible flow represents one of the important types of CFD problem where fluid density undergoes changes in both time and space. During the early period of CFD prediction of the second law, the applications were mainly related compressible flows [65]. Lax documented many of the techniques and sample results for compressible flows

[66]. Borth and Argrow analyzed compressible flow solutions in complex flow fields in view of the second law [67]. The stable algorithms of turbulence modeling with the consideration of compressible flow were developed by Herard [68]. By employing the turbulence closures the numerical stability could be maintained through the iterative implementation to avoid magnifying small errors that could result in divergence. This model employs entropy characterizations and considers a more robust compressible flow solver by using a splitting technique in accordance with entropy inequalities.

The entropy production of phase change is encountered in a variety of practical applications, such as materials processing, casting solidification, extrusion, and injection molding [69] . Naterer carried out the experimental studies where heat–entropy analogies are applied to problems involving phase change heat transfer with fluid flow [70].

Chu and Liu used a CFD code to analyze a 2D jet flow with radiation and convection heat transfer at high temperature as well as entropy generation to optimize the second law performance of energy conversion for the device [71]. Iandoli and Sciubba determined the entropy generation rate in turbomachinery passages from the computed velocity and temperature fields [72]. In addition, the sources of entropy production in turbo machinery flows were discussed by Denton [73]. Paulus presented a mathematical model of entropy production in compressors [74]. Finally, Iandoli and Sciubba investigated the flow field and local entropy generation rates in a radial compressor stage by means of a commercial CFD code [75]. Naterer and Camberos presented a review of the diverse roles of entropy and the second law in computational thermo–fluid dynamics [33]. In the early time of this field, Courant, Freidrichs, and Lewy made a major contribution to numerical analysis of thermo-fluid problems as the stable condition they

set up established a criterion in time step restriction for linear differential equations [76]. Baytas presented applications involving entropy production with natural convection in cavities [48].

Various formulations of entropy production have been derived over the past few decades for different physical processes. Naterer and Schneider asserted that entropy generation must be nonnegative under the condition of presence of discontinuities such as on-dimension shockwaves [77]. The maximum value of the specific entropy across the shock wave depends only on the upstream Mach number and the ratio of specific heats [77]. Poulikakos et al. [39] established a theoretical framework for the minimization of entropy generation in extended fin surfaces, when selecting the optimal fin geometries and dimensions. Adeyinka and Naterer developed new formulations of incompressible viscous turbulent flow in the entropy transport equation [78], where the entropy transport equations are derived for both gases and liquids. Kock and Herwig identified four different mechanisms of entropy production based on the time-averaged entropy balance equation and formulated to mathematical equations [79]. Dumouchel [80] developed a maximum entropy formalism to predict the drop-size distribution of liquid sprays, based on characteristic features of the liquid atomization process. McEligot et al. [81] used direct numerical simulations (DNS) to predict entropy generation in the viscous layer of turbulent channel flow at a high Reynolds number. A comparison was made between two approaches for the prediction of local entropy generation rate in the viscous layer.

The entropy generation in numerical analysis undergo the discretization process based on the transport form of the second law. Naterer suggested that when calculating entropy in terms of the solution variables, piecewise constant values of the conservation

variables should be used, thereby assuming a type of quasi-equilibrium condition to ensure the positive definite form [82]. The numerical stability issue of fluid flow simulations was recognized and addressed [83] [32]. Merriam suggested a more stringent condition imposed on different CFD model is necessary and sufficient to ensure a positive entropy production rate in each grid and eliminate nonlinear instability for discrete scalar equations [83].

2.3 Fluid machinery and cavitation

Flow around turbine or propeller blades may involve cavitation at certain flow conditions. Numerical simulation methods have successfully been applied to cavitation predictions for rotating machinery [84]. Rhee et al. studied propeller cavitation with a single-fluid multi-phase flow method [85]. Lindau et al. investigated cavitation flow around a marine propeller using a RANS computational model of homogeneous multiphase flow [86]. Medvitz et al. evaluated centrifugal pump performance over a wide range of flow coefficients and cavitation numbers [87]. When cavitation occurs, the mixture density of water and vapour can change rapidly with the formation of vapour bubbles. The component density, contrary to a mixture, does not change significantly. For cavitating flows, it is advantageous to formulate the mass fraction conservation equation in terms of a volume-fraction equation so the mixture density no longer appears in the conservation equation [88]. (CFD) technologies can also be used for analysis and evaluation of the cavitation occurrence in propeller design. Chiharu Kawakita, Reiko Takashima and Kei Sato applied this technology to energy-saving devices optimization to improve the propulsive performance [89].

The cavitation model in this study is a full cavitation model because it accounts for all physical effects of mass transfer, bubble dynamics, and turbulence. It employs the Rayleigh-Plesset equations of bubble dynamics to predict the phase-change processes for vapor generation and condensation in the cavitating regions. The model is suitable for 3D simulations of cavitating flows in a number of actual industrial processes. Past studies with this model have been documented in previous literature. Singhal [90] derived a full cavitation model accounting for the formation and transport of vapor bubbles and the turbulent fluctuations of pressure and velocity. Athavale [91] used the full cavitation model for performance predictions of engineering equipment under cavitating flow conditions. A vapor transport equation was used for the vapor phase, and it was coupled with the turbulent Navier-Stokes equations.

Cavitation can be described as a type of two-phase flow in which the flow phenomena are dominated by the fluid phase and quantity of vapour bubbles. Because of the influence of the vapour phase on the fluid dynamic behaviour of the mixture and its importance in a cavitation process, the vapour phase cannot be neglected or simplified to represent the cavitating flow as a single-phase flow. It is important to develop a two-phase flow model that represents the cavitating flow phenomenon realistically. Different modeling approaches for two-phase flow have been developed, depending on the formulation of the equations used to determine the velocity differences. Zuber and Findlay [92] determined the value of void fraction from assumed profiles of the void fraction and total volumetric flux for a bubbly or slug flow. Islii [93] presented the macroscopic formulations in terms of the two-fluid model and drift-flux model. This

thesis aims to provide new insight and predictive models for entropy generation in two-phase flows involving cavitation.

2.4 Summary

The second law of thermodynamics and its application has been studied for years in various disciplines. For the scientist, there is a wealth of published literature on the thermo science, fluid mechanics and energy conservation and utilization. For the researchers or students, there is a wealth of published literature and publications that teach and instruct on a wide variety of program development and sustainability topics.

However, based on the literature review, what appears to be lacking and missing is the study on entropy production in the form of macro scale for bubbly two phase flow that has practical significance in both scientific and industrial fields. The gap between entropy for single phase flow and two phase flow needs to be filled.

Chapter 3

Formulation of two-phase fluid flow equations and the second law

3.1 Local instant characteristics

In this thesis, the Leibniz-Reynolds' transport theorem is used to recast derivatives of integrated quantities and formulate the basic equations of continuum mechanics. This theorem is expressed in the form of an integral as follows:

$$\frac{d}{dt}\int_{V_a} \Phi(\boldsymbol{x},t)\,dV = \int_{V_a}\left[\frac{\partial \Phi}{\partial t} + \nabla\cdot(\boldsymbol{w}\Phi)\right]dV \tag{3.1}$$

where V_a is a material volume, which is a volume of fluid that contains the same fluid as it moves and $\Phi(\boldsymbol{x},t)$ is some fluid property per unit volume with respect to time as a material volume deforms. The surface velocity is denoted by $\boldsymbol{w}$.

Furthermore, the Reynolds transport theorem is a special case of Leibniz rule given by [93].

$$\frac{d}{dt}\int_{V} \Phi(\boldsymbol{x},t)dV = \int_{V}\frac{\partial \Phi}{\partial t}dV + \int_{A}\Phi\boldsymbol{u}\cdot\boldsymbol{n}dA \tag{3.2}$$

where $V(t)$ is an arbitrary volume bounded by $A(t)$ and $\boldsymbol{u}\cdot\boldsymbol{n}$ is the surface displacement velocity of $A(t)$.(See Fig 3-1)

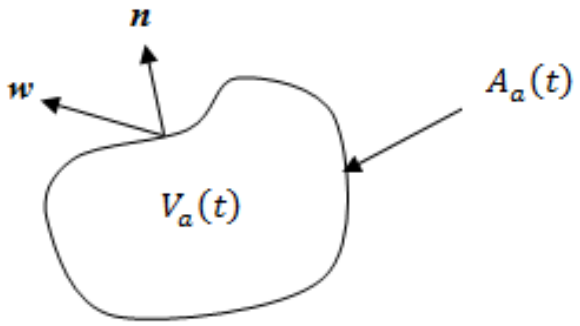

Figure 3-1: Arbitrary material volume

In view of the above, the quantities associated with phase k are subject to the following equation.

$$\rho_k \frac{D\psi_k}{Dt} = -\nabla \cdot J_k + \rho_k \Phi_k \tag{3.3}$$

where ψ_k is defined as the arbitrary quantity for an unit mass, ρ_k is the fluid density, J_k is the efflux, and Φ_k is the body force.

In the above equation the first term is the change of the quantity in time rate per unit volume. The second term is the convection rate. And the right-hand side terms represent the surface flux and the volume source [93].

The equations of fluid dynamics can be solved using conservation laws applying to a fluid continuum. The general form of the transport equation will be used as a base to reduce the continuity and momentum equations.

3.1.1 Continuity equation for single phase flow

The principle of continuity is the mass conservation and it can be expressed in a differential form:

$$\rho_k \frac{D\psi_k}{Dt} = -\nabla \cdot J_k + \rho_k \Phi_k$$

$$\psi_k = 1, \Phi_k = 0, J_k = 0 \tag{3.4}$$

Because there is no surface or volume source of mass with respect to the control volume, we obtain the continuity equation from the general balance equation:

$$\rho_k \frac{D\psi_k}{Dt} = 0 \tag{3.5}$$

where ρ_k and $\boldsymbol{u}_k$ are the density and velocity of phase k.

3.1.2 Momentum equation

The momentum equation is Newton's second law that relates the sum of the forces acting on the control volume of fluid to its acceleration or rate of change of momentum [93]. The equation can be obtained from Eq. (3.3) by introducing the surface stress, $\boldsymbol{\tau}_k$, and the body force, $\mathbf{g}_k$; thus, we set

$$\psi_k = \boldsymbol{u}_k\,, \quad \Phi_k = \mathbf{g}_k \qquad J_k = p_k\mathbf{I} - \boldsymbol{\tau}_k \tag{3.6}$$

where **I** is the unit tensor, which is expressed as follows:

$$\mathbf{I} = \begin{bmatrix} 1 & 0 & 0 \\ 0 & 1 & 0 \\ 0 & 0 & 1 \end{bmatrix} \tag{3.7}$$

In view of Eq. **(**3.3), we have

$$\rho_k \frac{D\boldsymbol{u}_k}{Dt} = -\nabla p_k + \nabla \cdot \boldsymbol{\tau}_k + \rho_k \mathbf{g}_k \tag{3.8}$$

To meet the requirement of conservation law, the change in momentum of the fluid in the control volume over time must be equal to the net downstream impulse plus the net flux of momentum during the time period. In above equation, $\boldsymbol{\tau}_k$, is the stress tensor, which includes normal and shear stresses,and $\rho_k \mathbf{g}_k$ is the body force.

3.2 Eulerian averaging method in connection with two-phase flow analysis

Both Eulerian time and spatial averaging can be used in order to study two-phase flow systems. A comparison of the two averaging methods is provided by Lee et al. [94]. Experimentalists consider a two-phase mixture as a quasi-continuum. This quasi-continuum is used for treating the discontinuous media as continuous in order to apply Jacobian transformation when describing the "general" local attributes of the flow. In fact, it is not necessary to take into account of the microscopic details of the fluid motions for

solving an engineering problem, whereas, the macroscopic aspects of the flow are much more preferred. Hence, the description of the local attributes depends on the mathematical expression of macroscopic properties of the flow instead of microscopic characteristics [93].

This straightforward idea stems from the theory of homogeneous flow, but fluid can involve more than two media, such as a mixture of alcohol and water. Such a media mixture has its own property and evenly continuous feature without moving interfaces. It can be treated as a "new" synthetic fluid. The methodology for transforming a bubbled flow to a "mixture" is similar, but there are specific differences due to the phase state.

We usually obtain the mean values of fluid motions and properties by eliminating local instant fluctuations. The averaging procedure is to exclude unwanted high frequency of local instant fluctuations. However, these statistical properties of high frequency fluctuations have significant impacts on the macroscopic phenomena and they have to be taken into account for the averaging formulation. To derive the governing equations which are suitable to multiphase flow, the local characteristics of the flow must be described using some of closures.

3.3 Continuity and momentum equations

In this present research, a modified slip mixture model is derived and described in detail. This model was first introduced by Ishii [95]. Later, Manninen and Taivassalo [96] provided a more general formulation that forms the basis for the implementation in the commercial CFD codes.

The model assumes the presence of a continuous medium containing a dispersed vapour phase and it behaves as a single fluid. The fluid properties depend on the

quantities of dispersed phases. The slip velocity can be calculated from algebraic equations involving only local variables that independent of other partial differential equations. It can handle two phases by solving the momentum and continuity equations for the mixture, then the volume fraction equation for the vapour phase, and an algebraic expression for the relative velocity.

The algebraic slip model is expressed in terms of four field equations: mixture continuity; momentum; vapour continuity, and algebraic equations, which include the slip velocity of the vapour phase relative to the fluid phase instead of momentum of the vapour phase. The most readily evaluated term is the mixture density, ρ_m. The density of each phase, vapour, ρ_v, and liquid, ρ_l, is assumed constant. This assumption is applicable for most practical two-phase flow problems, because the transverse pressure gradient is relatively small [97]. Under the above simplifying assumptions, the mixture density becomes

$$\rho_m \equiv \alpha_v \rho_v + (1 - \alpha_v)\rho_l \tag{3.9}$$

where α_v refers to the volume fraction of the vapour phase. Although the component densities for vapour and liquid are constant, ρ_m varies with α_v. Then, the mixture velocity is defined by

$$\mathbf{u}_m \equiv \frac{\alpha_v \rho_v \mathbf{u}_v + (1-\alpha_v)\rho_l \mathbf{u}_l}{\rho_m} \tag{3.10}$$

The mass fraction of the vapour phase is defined as

$$c_v = \frac{\alpha_v \rho_v}{\rho_m} \tag{3.11}$$

Then, the governing equations for continuity and momentum of the mixture are

$$\frac{\partial}{\partial t}(\rho_m) + \nabla \cdot (\rho_m \mathbf{u}_m) = 0 \tag{3.12}$$

$$\rho_m \frac{D\mathbf{u}_m}{Dt} = -\nabla p_m + \nabla \cdot (\boldsymbol{\tau}_m + \boldsymbol{\tau}_{Tm}) + \nabla \cdot \boldsymbol{\tau}_{Dm} + \rho_m \mathbf{g} \tag{3.13}$$

The momentum equation of the vapour phase can be rewritten as follows:

$$\alpha_v \rho_v \frac{D\mathbf{u}_v}{Dt} = -\alpha_v \nabla p_v + \nabla \cdot [\alpha_v(\boldsymbol{\tau}_v + \boldsymbol{\tau}_{Tv})] + \alpha_v \rho_v \mathbf{g} + \mathbf{M}_v \tag{3.14}$$

where the momentum source term, $\mathbf{M}_v$, is given by

$$\mathbf{M}_v = \alpha_v(\rho_v - \rho_m)\left[\frac{D\mathbf{u}_m}{Dt} - \mathbf{g}\right] \tag{3.15}$$

The following approximations were used to derive the equation [96]:

$$p_v = p_l = p_m \tag{3.16}$$

$$(\mathbf{u}_v \cdot \nabla)\mathbf{u}_v \approx (\mathbf{u}_m \cdot \nabla)\mathbf{u}_m \tag{3.17}$$

$$\tau_v = 0, \tau_m = 0, \text{ and } \tau_{Dm} = 0 \tag{3.18}$$

In addition, it is assumed that the inter-phase momentum transfer is approximated from drag on spherically shaped particles (bubbles) [98]:

$$\mathbf{M}_v = -\frac{3}{4} C_D \frac{\alpha_v \rho_l |\mathbf{u}_{lv}| \mathbf{u}_{lv}}{d_v} \tag{3.19}$$

where d_v is the diameter of the bubbles and C_D is the drag coefficient. The drag coefficient depends on the bubble Reynolds number, Re_v which is defined as follows:

$$\mathrm{Re}_v = \frac{d_v \rho_l |\mathbf{u}_{lv}|}{\mu_l} \tag{3.20}$$

where, $\mathbf{u}_{lv}$ is the slip velocity between liquid and vapour phase. A general expression for the drag coefficient is given as follows [99]:

$$C_D = \begin{cases} \frac{24}{\mathrm{Re}_v}(1 + 0.15\mathrm{Re}_v^{0.687}) & Re_v < 1000 \\ 0.44 & Re_v \geq 1000 \end{cases} \tag{3.21}$$

The slip velocity is written as [100]

$$|\mathbf{u}_{lv}|\mathbf{u}_{lv} = \frac{4}{3}\frac{d_v}{\alpha_v \rho_l C_D}\left\{\alpha_v(\rho_v - \rho_m)\left[\mathbf{g} - (\mathbf{u}_m \cdot \nabla)\mathbf{u}_m - \frac{\partial \mathbf{u}_m}{\partial t}\right]\right\} \tag{3.22}$$

Then, the continuity equation for the vapour phase can be expressed in terms of $\mathbf{u}_{lv}$ as follows:

$$\rho_v \frac{D\boldsymbol{\alpha}_v}{Dt} = \Gamma_v - \nabla \cdot [\alpha_v \rho_v \mathbf{u}_{lv}(1 - c_v)] \tag{3.23}$$

where the diffusion stress, $\boldsymbol{\tau}_{Dm}$, can be expressed as a function of $\mathbf{u}_{lv}$ [96]:

$$\boldsymbol{\tau}_{Dm} = -\rho_m c_v(1 - c_v)|\mathbf{u}_{lv}|\mathbf{u}_{lv} \tag{3.24}$$

In the next section, this formulation will be adapted for turbulent two-phase flow.

3.4 Turbulence formulation

Generalized stress includes the influence of both viscous shear stress and turbulent stress, which can be expressed as follows [101]:

$$\boldsymbol{\tau}_{Dm} = \boldsymbol{\tau}_m + \boldsymbol{\tau}_{Tm} \tag{3.25}$$

$$\boldsymbol{\tau}_{Gm} = (\mu_m + \mu_{Tm})\left[(\nabla \mathbf{u}_m + \nabla \mathbf{u}_m^T) - \frac{2}{3}(\nabla \cdot \mathbf{u}_m)I\right] - \frac{2}{3}\rho_m k_m I \tag{3.26}$$

where I is a unit tensor and $k_m$is the turbulent kinetic energy density for the mixture phase. The dynamic viscosity for the mixture μ_m is defined as

$$\mu_m = \alpha_v \mu_v + (1 - \alpha_v)\mu_l \tag{3.27}$$

The coefficient of the turbulent eddy viscosity for the mixture can be written in the following form as a single-phase flow:

$$\mu_{Tm} = \frac{C_{\mu m}\rho_m k_m^2}{\varepsilon_m} \tag{3.28}$$

Transport equations for the standard k-ε model for k (turbulent kinetic energy) and ε (dissipation rate of turbulent kinetic energy) are as follows [101]:

$$\rho_m \frac{Dk_m}{Dt} - \nabla \cdot \left[\mu_m + \frac{\mu_{Tm}}{\sigma_{km}}\right]\nabla k_m = P_k + P_b - \rho_m \varepsilon_m - Y_M + S_k \tag{3.29}$$

For dissipation ε,

$$\rho_m \frac{D\varepsilon_m}{Dt} - \nabla \cdot \left[\mu_m + \frac{\mu_{Tm}}{\sigma_{\varepsilon m}}\right] \nabla \varepsilon_m = C_{1\varepsilon} \frac{\varepsilon_m}{k_m}(P_k + C_{3\varepsilon} P_b) - C_{2\varepsilon} \rho_m \frac{\varepsilon_m^2}{k_m} + S_\varepsilon \quad (3.30)$$

Production of k is expressed

$$P_k = -\rho_m \overline{\mathbf{u}'_m \mathbf{u}'_m} \nabla \mathbf{u}_m^T \quad (3.31)$$

$$P_k = \mu_{Tm} S^2 \quad (3.32)$$

where S represents the modulus of the mean rate of strain tensor, which is defined as

$$S \equiv \sqrt{2\boldsymbol{S}\boldsymbol{S}} \quad (3.33)$$

and the effect of buoyancy is written as

$$P_b = \beta \mathrm{g} \frac{\mu_{Tm}}{\mathrm{Pr}_{Tm}} \nabla T \quad (3.34)$$

where Pr_{Tm} is the turbulent Prandtl number for energy and g is the component of the gravitational vector. From experimental data, the default value of Pr_{Tm} has an average value of 0.85, but ranges from 0.7 to 0.9 depending on the Prandtl number of the fluid in question [102]. β is the coefficient of thermal expansion, which is defined as

$$\beta = -\frac{1}{\rho_m}\left(\frac{\partial \rho_m}{\partial T}\right)_p \quad (3.35)$$

The model constants have the following default values:

$$C_{\mu m} = 0.09, C_{1\varepsilon} = 1.44, C_{2\varepsilon} = 1.92, \sigma_{km} = 1.0, \sigma_{\varepsilon m} = 1.3 \quad (3.36)$$

Cavitation is a process involving two-phase flow with a fluid phase and vapour bubbles. To describe turbulence in a cavitating flow, the standard k-ε turbulence equations can be used. The formulation will use the turbulent viscosity in terms of k and ε in the mixture momentum equation. The onset of flow cavitation is characterized by the cavitation number, defined as follows [103]:

$$C_a = \frac{p - p_v}{{}^1\!/_2 \rho_l u_l^2} \quad (3.37)$$

Thus, the total inter-phase mass transfer rate per unit volume can be derived from the Rayleigh-Plesset equation [103]:

$$\Gamma_v = \frac{3\alpha_v \rho_v}{d_v}\sqrt{\frac{2}{3}\frac{p_v - p}{\rho_l}} \tag{3.38}$$

3.5 Transport equations for individual phases

The local instant velocity of phase k is denoted by $\mathbf{u}_{Ik}$. The average velocity based on weighting the velocity with the local density ρ_{Ik} can be defined as [93]

$$\mathbf{u}_k = \frac{\overline{\rho_{Ik}\mathbf{u}_{Ik}}}{\overline{\rho_{Ik}}} = \frac{\overline{\rho_{Ik}\mathbf{u}_{Ik}}}{\rho_k} \tag{3.39}$$

where, ρ_k is the average material density.

The continuity and momentum equations for each phase k are defined as follows:

$$\rho_k \frac{D\alpha_k}{Dt} = \Gamma_k \tag{3.40}$$

$$\rho_k \frac{D(\alpha_k \mathbf{u}_k)}{Dt} = -\alpha_k \nabla p_k + S \cdot [\alpha_k(\boldsymbol{\tau}_k + \boldsymbol{\tau}_{Tk})] + \alpha_k \rho_k \mathbf{g} + \mathbf{M}_k \tag{3.41}$$

where α_k is the volume fraction of phase k. The term Γ_k represents the rate of mass generation of phase k at the interface, and $\mathbf{M}_k$ is the average interfacial momentum source for phase k. $\boldsymbol{\tau}_k$is the average viscous stress tensor. The turbulent stress tensor $\boldsymbol{\tau}_{Tk}$ is given by [93]

$$\boldsymbol{\tau}_{Tk} = -\overline{\rho_{Ik}\mathbf{u}_k'\mathbf{u}_k'} \tag{3.42}$$

where $\mathbf{u}'$ is the fluctuating component of the velocity, that is, $\mathbf{u}_k' = \mathbf{u}_{Ik} - \mathbf{u}_k$.

3.6 Continuity equation for the mixture

From the continuity Eq. (3.40) for phase k, we obtain the following by summing over all phases:

$$\frac{\partial}{\partial t}\sum_{k=1}^{n}(\alpha_k \rho_k) + \nabla \cdot \sum_{k=1}^{n}(\alpha_k \rho_k \mathbf{u}_k) = \sum_{k=1}^{n}\Gamma_k \tag{3.43}$$

Because the total mass is conserved,

$$\sum_{k=1}^{n} \Gamma_k = 0 \tag{3.44}$$

and the continuity equation of the mixture can be obtained:

$$\frac{\partial \rho_m}{\partial t} + \nabla \cdot (\rho_m \mathbf{u}_m) = 0 \tag{3.45}$$

Here, the mixture density and the mixture velocity are defined as

$$\rho_m = \sum_{k=1}^{n} (\alpha_k \rho_k) \tag{3.46}$$

$$\mathbf{u}_m = \frac{1}{\rho_m} \sum_{k=1}^{n} (\alpha_k \rho_k \mathbf{u}_k) = \sum_{k=1}^{n} (c_k \mathbf{u}_k) \tag{3.47}$$

$$\mathbf{u}'_{\boldsymbol{m}} = \frac{1}{\rho_m} \sum_{k=1}^{n} (\alpha_k \rho_k \mathbf{u}'_{\boldsymbol{k}}) = \sum_{k=1}^{n} (c_k \mathbf{u}'_{\boldsymbol{k}}) \tag{3.48}$$

The mixture velocity $\mathbf{u}_m$ represents the velocity of the mass center. Thus, the mass fraction of phase k is defined as follows:

$$c_k = \frac{\alpha_k \rho_k}{\rho_m} \tag{3.39}$$

3.7 Momentum equation for the mixture

The momentum equation for the mixture follows from (3.41) by summing over the phases:

$$\frac{\partial}{\partial t} \sum_{k=1}^{n} (\alpha_k \rho_k \mathbf{u}_k) + \nabla \cdot \sum_{k=1}^{n} (\alpha_k \rho_k \mathbf{u}_k \mathbf{u}_k) = -\sum_{k=1}^{n} (\alpha_k \nabla p_k) + \nabla \cdot \sum_{k=1}^{n} [\alpha_k (\boldsymbol{\tau}_k + \boldsymbol{\tau}_{Tk})] + \sum_{k=1}^{n} (\alpha_k \rho_k \mathbf{g}) + \sum_{k=1}^{n} \mathbf{M}_k \tag{3.40}$$

Using the definitions (3.46) and (3.47) of the mixture density ρ_m and the mixture velocity $\mathbf{u}_m$, the second term of (3.40) can be rewritten as

$$\nabla \cdot \sum_{k=1}^{n} (\alpha_k \rho_k \mathbf{u}_k \mathbf{u}_k) = \nabla \cdot \sum_{k=1}^{n} (\rho_m \mathbf{u}_m \mathbf{u}_m) + \nabla \cdot \sum_{k=1}^{n} (\alpha_k \rho_k \mathbf{u}_{Mk} \mathbf{u}_{Mk}) \tag{3.41}$$

where $\mathbf{u}_{Mk}$ is the diffusion velocity, that is, the velocity of phase k relative to the center of the mixture mass

$$\mathbf{u}_{Mk} = \mathbf{u}_k - \mathbf{u}_m \tag{3.42}$$

In terms of the mixture variables, the momentum equation takes the form

$$\rho_m \frac{D\mathbf{u}_m}{Dt} = -\nabla p_m + \nabla \cdot (\boldsymbol{\tau}_m + \boldsymbol{\tau}_{Tm}) + \nabla \cdot \boldsymbol{\tau}_{Dm} + \rho_m \mathbf{g} + \mathbf{M}_m \tag{3.43}$$

The three stress tensors are defined as

$$\boldsymbol{\tau}_m = \sum_{k=1}^{n} (\alpha_k \boldsymbol{\tau}_k) \tag{3.44}$$

$$\boldsymbol{\tau}_{Tm} = -\sum_{k=1}^{n} \left(\alpha_k \overline{\rho_{Ik} \mathbf{u}_k' \mathbf{u}_k'} \right) \tag{3.45}$$

$$\boldsymbol{\tau}_{Dm} = -\sum_{k=1}^{n} (\alpha_k \rho_k \mathbf{u}_{Mk} \mathbf{u}_{Mk}) \tag{3.46}$$

and represent the average viscous stress, turbulent stress, and diffusion stress due to the phase slip, respectively. In Eq. (3.43), the pressure of the mixture is defined by the relation

$$\nabla p_m = \sum_{k=1}^{n} (\alpha_k \nabla p_k) \tag{3.47}$$

Thus, the influence of the surface tension forces on the mixture is defined as

$$\mathbf{M}_m = \sum_{k=1}^{n} \mathbf{M}_k \tag{3.48}$$

3.6 Continuity equation for a phase

Use of the definition of the diffusion velocity (3.42) to eliminate the phase velocity in the continuity Eq. (3.40) gives

$$\frac{\partial}{\partial t} (\alpha_k \rho_k) + \nabla \cdot (\alpha_k \rho_k \mathbf{u}_m) = \Gamma_k - \nabla \cdot (\alpha_k \rho_k \mathbf{u}_{Mk}) \tag{3.49}$$

If the phase densities are constants and phase changes do not occur, the continuity equation reduces to

$$\frac{\partial}{\partial t} \alpha_k + \nabla \cdot (\alpha_k \mathbf{u}_m) = \frac{\Gamma_k}{\rho_k} - \nabla \cdot (\alpha_k \mathbf{u}_{Mk}) \tag{3.50}$$

The diffusion velocity must be determined through the relative (slip) velocity, which is defined as the velocity of the dispersed phase relative to the velocity of the continuous phase:

$$\mathbf{u}_{Ck} = \mathbf{u}_k - \mathbf{u}_c \tag{3.51}$$

The diffusion velocity of a dispersed phase *l*, $\mathbf{u}_{Ml} = \mathbf{u}_l - \mathbf{u}_m$, can be presented in terms of the relative velocities:

$$\mathbf{u}_{Ml} = \mathbf{u}_{Cl} - \sum_{k=1}^{n}(c_k \mathbf{u}_{Ck}) \tag{3.52}$$

If only one dispersed phase *p* is present, its diffusion velocity is given by

$$\mathbf{u}_{Mp} = (1 - c_p)\mathbf{u}_{Cp} \tag{3.53}$$

where c_p is the mass fraction of dispersed phase p defined as

$$c_p = \frac{\alpha_p \rho_p}{\rho_m} \tag{3.54}$$

3.7 Constitutive equations

The generalized stress includes the influence of both viscous shear stress and turbulent stress, identified as follows:

If only one dispersed phase is present, Eq. (3.45) simplifies to

$$\boldsymbol{\tau}_{Dm} = -\rho_m c_p (1 - c_p)|\mathbf{u}_{Cp}|\mathbf{u}_{Cp} \tag{3.55}$$

If the more generalized stress, $\boldsymbol{\tau}$, includes the influence of viscous shear stress, turbulent stress, and diffusion stress, then

$$\boldsymbol{\tau} = \boldsymbol{\tau}_m + \boldsymbol{\tau}_{Tm} + \boldsymbol{\tau}_{Dm} = (\mu_m + \mu_{Tm})\left[(\nabla \mathbf{u}_m + \nabla \mathbf{u}_m^T) - \frac{2}{3}(\nabla \cdot \mathbf{u}_m)\mathbf{I}\right] -$$

$$\rho_m \left[\frac{2}{3} k_m \mathbf{I} + c_p (1 - c_p)|\mathbf{u}_{Cp}|\mathbf{u}_{Cp}\right] \tag{3.56}$$

The momentum equation of the mixture (3.42), can be written as

$$\frac{\partial}{\partial t}(\rho_m \mathbf{u}_m) + \nabla \cdot (\rho_m \mathbf{u}_m \mathbf{u}_m) = -\nabla p_m + \nabla \cdot \boldsymbol{\tau} + \mathbf{F} \tag{3.57}$$

where, **F** is body force,

$$\mathbf{F} = \rho_m \mathbf{g} + \mathbf{M}_m \tag{3.58}$$

Thus, Eq. (3.56) can be written as

$$\rho_m \frac{D\mathbf{u}_m}{Dt} = -\nabla p_m + \nabla \cdot \boldsymbol{\tau} + \mathbf{F} \tag{3.59}$$

In Eq. (3.59), $\boldsymbol{\tau}$ is a stress tensor.

3.8 Formulations of the second law of thermodynamics

The second law of thermodynamics is to express the tendency of entropy to increase. While the quantity of energy remains constant, the quality of energy deteriorates gradually over time. The law explains the phenomenon of irreversibility in nature from the equilibrium state. The impact of entropy extends from the microscopic scale to the largest scales of engineering systems, the environment and the earth.

According to Clausius equality, for a reversible process [9],

$$\oint \frac{\delta Q}{T} = 0 \tag{3.60}$$

Eq.(3.60) indicates the line integral $\int_L \frac{\delta Q}{T}$ is path independent. A state function s can be defined, which satisfies the following:

$$ds = \frac{\delta Q}{T} \tag{3.61}$$

Equation (3.61) can be integrated with the initial condition, s = 0 at absolute zero so that the entropy can be considered as a state function of a thermodynamic system. Its property depends only on the present state of the system. Equation (3.61) can also be used to measure the amount of energy multiplying by a local temperature for a reversible process. In this process if the system gives up energy ΔE and its entropy falls by Δs, a quantity of energy $T\Delta s$ will dissipate to the surroundings of the system with the form of heat, where

T is the surrounding temperature of the system. In this research, this thermodynamic definition of entropy is the object that will be focused on throughout.

3.9 The fundamental thermodynamic relation

The change in entropy can be related to the change in internal energy and specific volume and can be represented as follows:

$$de = Tds - Pdv \tag{3.62}$$

where e is internal energy. Eq. (3.62) is a form of the Gibbs equation which provides a relationship to determine the specific entropy, s, in terms of other thermodynamic state variables [104].

3.10 Entropy change

Entropy of an ideal gas may change with volume, pressure, and temperature. The two equations for calculating the entropy change, Eqs. (3.63) and (3.64), can be used for any process, i.e. they are not restricted to a process of constant specific heat and volume. If the specific heat changes with the temperature, the value of the specific heat at the mean temperature should be used.

$$\Delta s = C_v ln\frac{T}{T_0} + R\, ln\frac{V}{V_0} \tag{3.63}$$

or

$$\Delta s = C_p ln\frac{T}{T_0} - R\, ln\frac{P}{P_0} \tag{3.64}$$

where C_v is the specific heat at constant volume, C_p is the specific heat at constant pressure, and R is the ideal gas constant.

Chapter 4

Formulations of entropy production rate for single-phase flow

In this chapter, the entropy production for laminar flow is formulated as a validation case study. Subsequently, the turbulent flow method is formulated, and the analysis is performed with the Direct Numerical Simulation (DNS) data of turbulent channel flow. Two turbulent flow entropy production terms are derived based on Reynolds decomposition and approximated using a turbulent viscosity / dissipation or Reynolds shear stress approach. The basic conception of RANS equations is to decompose an instantaneous quantity into its time-averaged and fluctuating quantities. These equations can give approximate time-averaged solutions to the Navier–Stokes equations. Based on the solutions, the expression of the mean entropy production regarding other quantities of mean flow can be developed. This new model of entropy production incorporates the eddy viscosity into a total shear stress. In addition, the Reynolds shear stress is used as an alternative formulation. Results for solutions of the entropy transport equations are presented and discussed for both laminar and turbulent flow problems.

A direct numerical simulation (DNS) numerically solves the Navier-Stokes equations without modeling for turbulence. DNS can be used for solving the turbulence in a large range of spatial and time-based scales in a computational mesh. The large range covers the scales from the smallest dissipative to the integral scale, associated with the flow motions that contain large amount of the kinetic energy. The memory requirement for a DNS increases very fast with the increase in Reynolds number. In order to obtain an accurate solution, the time step Δt must be small enough to capture a fluid particle

moving only a fraction of the mesh spacing. Consequently, the required number of time steps grows rapidly as a power law of the Reynolds number.

Even at low Reynolds numbers the computational resources required by a DNS is costly. For resolving the problems in most industrial applications it exceeds the capacity of most powerful computers. However, DNS provides a useful tool in turbulent fundamental research as it directly performs numerical simulation. Usually it is difficult or impossible to extract information from lab experiment but is possible to perform "numerical experiments" using DNS, which allows a better understanding of the mechanism of turbulence.

In this chapter, DNS data of turbulent channel flow is used for validating the entropy model to obtain accurate predictions. The DNS data is also used to validate the numerical results from RANS.. Wall-bounded single-phase flows have been widely applied in industries. It is important to investigate the irreversibility of flow due to viscous frictions and kinetic energy dissipation. Especially, wall-bounded turbulent flows at high Reynolds numbers have become an increasingly active area of research in recent years. In this chapter, the case studies deal with exergy destructions for both laminar and turbulent single-phase flow from the view of entropy production.

4.1 Problem formulation and governing equations

The continuity equation for mass conservation and the momentum equation are written as follows:

$$\frac{\partial \rho}{\partial t} + \nabla \cdot (\rho \mathbf{u}) = 0 \tag{4.1}$$

$$\frac{\partial}{\partial t}(\rho \mathbf{u}) + \nabla \cdot (\rho \mathbf{u}\mathbf{u}) = -\nabla p + \nabla \cdot \boldsymbol{\tau} + \rho \mathbf{g} \tag{4.2}$$

The total energy equation is given by

$$\rho \frac{D}{Dt}\left(e + \frac{1}{2}\mathbf{u}^2\right) = -\nabla \cdot \boldsymbol{q} - \nabla \cdot (p\mathbf{u}) + \nabla \cdot (\boldsymbol{\tau} \cdot \mathbf{u}) + \rho \mathbf{u} \cdot \mathbf{g} + \dot{q} \tag{4.3}$$

where e, $\boldsymbol{q}$,and $\dot{q}$ represent the internal energy, heat flux, and body heating, respectively. The mechanical (kinetic) energy equation can be obtained by taking the dot product of the momentum equation and velocity, yielding

$$\frac{1}{2}\rho \frac{D\mathbf{u}^2}{Dt} = -\nabla \cdot (p\mathbf{u}) + p\nabla \cdot \mathbf{u} + \nabla \cdot (\boldsymbol{\tau} \cdot \mathbf{u}) - \boldsymbol{\tau} : \nabla \mathbf{u} + \rho \mathbf{u} \cdot \mathbf{g} \tag{4.4}$$

Note that the following identical equation for a symmetrical stress tensor is used here:

$$\boldsymbol{\tau} : \nabla \mathbf{u} \equiv \nabla \cdot (\boldsymbol{\tau} \cdot \mathbf{u}) - \boldsymbol{u} \cdot \boldsymbol{\nabla} \cdot (\boldsymbol{\tau}) \tag{4.5}$$

To express the second law of thermodynamics, it is necessary to introduce temperature T and specific entropy, s. Using the Clausius–Duhem inequality [93], the entropy transport equation can be expressed as

$$\frac{\partial}{\partial t}(\rho s) + \nabla \cdot (\rho s \mathbf{u}) + \nabla \cdot \left(\frac{\boldsymbol{q}}{T}\right) - \frac{\dot{q}}{T} \equiv \dot{P}_s \geq 0 \tag{4.6}$$

where $\dot{P}_s$ is the rate of entropy production.

The Gibbs free energy measures the useful work available from the thermodynamic state at a given temperature and pressure. In Gibbs equation, enthalpy and entropy are combined together and form a single variable. The change of free energy is equal to the sum of enthalpy plus the product of the temperature and entropy of the system. The Gibbs free energy is defined as follows:

$$G(p,T) = e + pV - Ts \tag{4.7}$$

where e is the internal energy, p is pressure, V is volume, T is the temperature, and s is the entropy.

Taking the differential form of Eq. (4.7), the transport form of the equation becomes

$$\frac{Ds}{Dt} = \frac{1}{T}\frac{De}{Dt} - \frac{p}{T}\frac{D}{Dt}\left(\frac{1}{\rho}\right) \tag{4.8}$$

Multiplying by ρ gives

$$\rho\frac{Ds}{Dt} = \frac{\rho}{T}\frac{De}{Dt} - \frac{p\rho}{T}\frac{D}{Dt}\left(\frac{1}{\rho}\right) \tag{4.9}$$

Thus, entropy transport equation (4.6) can be expressed as

$$\rho\frac{Ds}{Dt} + \nabla\cdot\left(\frac{\mathrm{q}}{\mathrm{T}}\right) - \frac{\dot{\mathrm{q}}}{\mathrm{T}} = \dot{\mathrm{P}}_{\mathrm{s}} \tag{4.10}$$

Substituting Eq. (4.9) into (4.10), the following expression is obtained:

$$\dot{P}_s = \frac{\rho}{T}\frac{De}{Dt} - \frac{p\rho}{T}\frac{D}{Dt}\left(\frac{1}{\rho}\right) + \nabla\cdot\left(\frac{\mathbf{q}}{T}\right) - \frac{\dot{\mathbf{q}}}{T} \tag{4.11}$$

The transport equation of internal energy can be obtained from Eqs. (4.3) through (4.4):

$$\rho\frac{De}{Dt} = -\nabla\cdot\mathbf{q} - p\nabla\cdot\mathbf{u} + \boldsymbol{\tau}:\nabla\mathbf{u} + \dot{q} \tag{4.12}$$

Substituting Eq. (4.12) into (4.11) gives

$$\dot{P}_s = \frac{1}{T}\{-\nabla\cdot\mathbf{q} - p\nabla\cdot\mathbf{u} + \boldsymbol{\tau}:\nabla\mathbf{u} + \dot{q}\} - \frac{p\rho}{T}\frac{D}{Dt}\left(\frac{1}{\rho}\right) + \nabla\cdot\left(\frac{\mathbf{q}}{T}\right) - \frac{\dot{q}}{T} \tag{4.13}$$

In Eq. (4.13),

$$\nabla\cdot\left(\frac{\mathbf{q}}{T}\right) = \frac{T\nabla\cdot\mathbf{q} - \mathbf{q}\cdot\nabla T}{T^2} \tag{4.14}$$

Applying standard Fourier's Law

$$\mathbf{q} = -K\cdot\nabla T \tag{4.15}$$

and noting

$$\frac{D}{Dt}\left(\frac{1}{\rho}\right) = -\frac{1}{\rho}\nabla\cdot\mathbf{u} \tag{4.16}$$

Eq. (4.13) becomes

$$\dot{P}_s = \frac{1}{T}(\boldsymbol{\tau}:\nabla\mathbf{u}) + \frac{K\nabla T\cdot\nabla T}{T^2} \tag{4.17}$$

For near isothermal flow, i.e. $\nabla T = 0$, Eq. (4.17) yields

$$\dot{P}_S = \frac{1}{T}(\boldsymbol{\tau}: \nabla \mathbf{u}) \tag{4.18}$$

4.2. Hydrodynamic irreversibility in channel flows

The channel flow is widely used in broad industrial applications and it has stimulated plentiful studies on kinetic energy loss in flow. The second-law analysis is important in understanding the entropy generation attributed to the thermodynamic irreversibility and useful for the optimum operating conditions in a system design with less entropy generation or exergy destruction. Viscous dissipation in laminar flow is the main source of entropy generation while in turbulent flow the irreversibility involves kinetic energy dissipation due to the eddy viscosity. The present study is aimed to compare the characteristics of entropy generation rate for single phase in wall-bounded channels and to set up the foundation of validation method, the energy balance. Also, it explores the alternative model of entropy production for turbulent channel flow. The relative deviations between the models are analysed for scrutinizing the changes entailed in the entropy generation due to the combination of the effect of viscous dissipation and other dissipation terms which come with the solutions of DNS and RANS for turbulent channel flow.

4.2.1 Formulation of entropy generation

A steady, incompressible laminar flow between two infinite parallel horizontal plates is shown in Fig.4-1. The analytical solution of the velocity profile is a well-known parabolic profile as follows [105]:

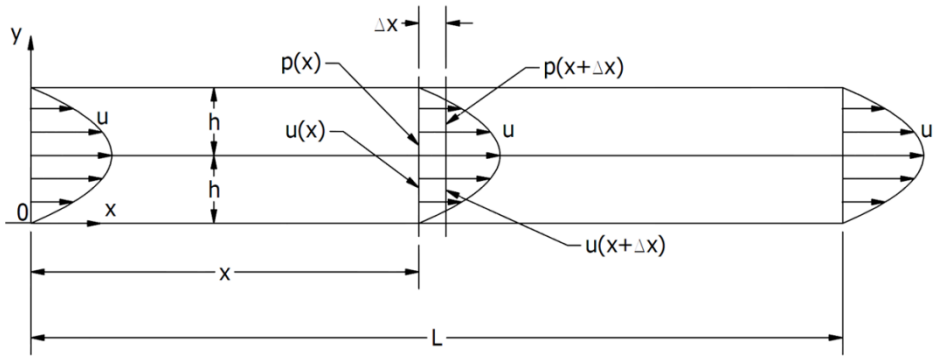

Figure 4-1: Laminar flow between fixed parallel plates

$$u = \frac{1}{2\mu}\frac{\partial p}{\partial x}[(y-h)^2 - h^2] \tag{4.19}$$

For a Newtonian fluid, the viscous stress tensor, $\boldsymbol{\tau}$, is expressed as [106]

$$\boldsymbol{\tau} = \mu(\nabla \mathbf{u} + \nabla \mathbf{u}^{\mathbf{T}}) \tag{4.20}$$

where μ is the constant dynamic viscosity. Eq. (4.18) can be written as

$$\dot{P}_s = \frac{\mu}{T}(\nabla \mathbf{u} + \nabla \mathbf{u}^{\mathbf{T}}) : \nabla \mathbf{u} \tag{4.21}$$

Using the velocity profile, the local distribution of entropy production rate for laminar flow between fixed parallel plates can be obtained as follows:

$$\dot{P}_s = \frac{1}{T}\frac{1}{\mu}\left(\frac{\partial p}{\partial x}\right)^2 (y-h)^2 \tag{4.22}$$

For a constant temperature, $\dot{P}_s$ is a function of y only because of the fully developed flow pattern. This profile is plotted in the cross-stream direction y in Fig. 4-2, showing that the peak value occurs at the wall in contrast with the velocity curve, which could be seen by comparing Eqs. 4.19 and 4.22.

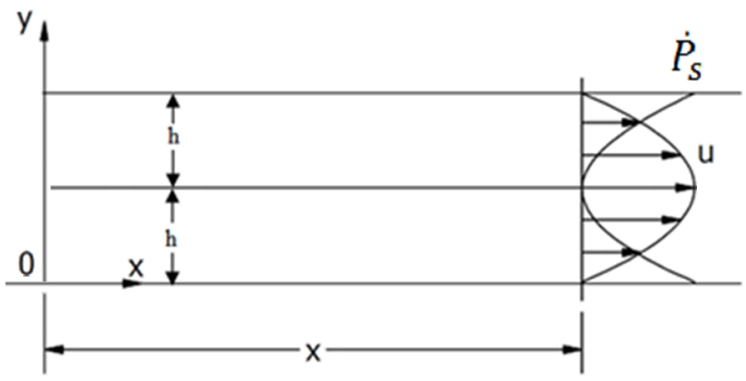

Figure 4-2: Entropy production rate of laminar flow between fixed parallel

Entropy generation gradually increases from zero at the centre of the channel to a maximum value at the wall. This trend indicates that the maximum entropy produced at the wall is mainly due to the fluid friction irreversibility contributed by the high near wall velocity gradient whereas towards the centre of the channel with zero velocity gradient, the entropy generation due to fluid friction. Equation 4.22 also shows that the entropy production rate at certain location is proportional to a constant, the square of pressure gradient.

4.2.2 Validation by an energy balance method

To validate this prior result by an energy balance, the kinetic energy loss due to friction between the layers must be converted to internal energy. This energy conversion is compared with the irreversibility determined by the second law of thermodynamics and model of entropy production rate. In Fig. 4-1, at an arbitrary position x, we investigate the destroyed exergy due to the entropy production. To form a control volume, we take a unit length in the z direction, Δx along the x-axis, and $2h$ in the y direction to construct the cuboids, and then apply the first law of thermodynamics to the control volume as follows:

$$\dot{Q} = \dot{m}[u(x+\Delta x) - u(x)] + \dot{m}\left[\frac{p(x+\Delta x)}{\rho} - \frac{p(x)}{\rho}\right] + \Delta\dot{E}_k \tag{4.23}$$

where $\dot{Q}$ is the heat transfer rate, $\dot{m}$ is the mass flow rate passing through the control volume, and $\Delta\dot{E}_k$ is defined as the difference of kinetic energy between the left and right sides of the control volume. The mass flow rate can be obtained by integrating the velocity across the channel section.

$$\dot{m} = \frac{2}{3}\frac{\rho}{\mu}\left(-\frac{\partial p}{\partial x}\right)h^3 \tag{4.24}$$

The kinetic energy can be determined by integration over the cross-section of the flow. Because the flow is fully developed in the channel, the velocity profile u is a function of *y* only. Consequently,

$$\Delta\dot{E}_k = 0 \tag{4.25}$$

Similarly, the first item of the right side in Eq. (4.23) is zero, so the equation can be simplified as follows:

$$\dot{Q} = \Delta x \frac{\dot{m}}{\rho}\frac{p(x+\Delta x)-p(x)}{\Delta x} \tag{4.26}$$

Note that the pressure gradient in the flow direction, *x*, is constant, and after substituting Eq. (4.24) into (4.26), the heat transfer rate, $\dot{Q}$, becomes

$$\dot{Q} = -\Delta x \frac{2}{3\mu}\left(\frac{\partial p}{\partial x}\right)^2 h^3 \tag{4.27}$$

where the negative sign means that heat is transferred from the system to the external.

The symbol $\dot{E}_x$ is defined as the destroyed exergy in the control volume. It can be found from volume integration of the entropy production rate multiplied by temperature:

$$\dot{E}_x = \Delta x \int_{-h}^{h} T\dot{P}_s \, dy \tag{4.28}$$

Substituting Eq. (4.22) into (4.28),

$$\dot{E}_x = \Delta x \frac{2}{3\mu}\left(\frac{\partial p}{\partial x}\right)^2 h^3 \tag{4.29}$$

Eq. (4.29) shows that, after the flow passes the distance, Δx, the destroyed exergy in the flow direction has the same value as the change of thermal energy, but with a positive sign. This result provides a useful energy validation method of the second law model.

4.2.3 Entropy distribution within the channel

Once the velocity is obtained, other quantities such as entropy generation can be found by substituting these quantities into Eq. (4.21). Under isothermal conditions and fully developed laminar flow, Eq. (4.10) becomes

$$\nabla \cdot (\rho s \mathbf{u}) = \dot{P}_s \tag{4.30}$$

Substituting Eqs. (4.19) and (4.22) into (4.30) yields

$$\frac{\partial s}{\partial x} = \frac{1}{T}\frac{2}{\rho}\left(-\frac{\partial p}{\partial x}\right)\frac{(y/h)^2}{1-(y/h)^2} \tag{4.31}$$

The specific entropy, s, can be obtained by integrating the right side of Eq. (4.31),

$$s = \frac{1}{T}\frac{2}{\rho}\left(-\frac{\partial p}{\partial x}\right)\frac{(y/h)^2}{1-(y/h)^2}x + s_0 \tag{4.32}$$

where

$$s_0 = \frac{1}{T}\frac{2}{\rho}\tau_w \tag{4.33}$$

and $\tau_w$is the viscous shear stress at the wall. This quantity is the product of wall shear rate, $\left(\frac{\partial u}{\partial y}\right)_{y=0}$, and the dynamic viscosity, μ:

$$\tau_w = -h\frac{\partial p}{\partial x} \tag{4.34}$$

As a result, Eq. (4.32) can be rearranged in dimensionless form:

$$\frac{s}{\frac{2h\tau_w}{T\rho}} = \frac{(1-y/h)^2}{1-(1-y/h)^2}\left(\frac{x}{h}\right) + 1 \tag{4.35}$$

Eq. (4.35) is plotted in Fig.4-3, showing the specific distributions for laminar channel flow.

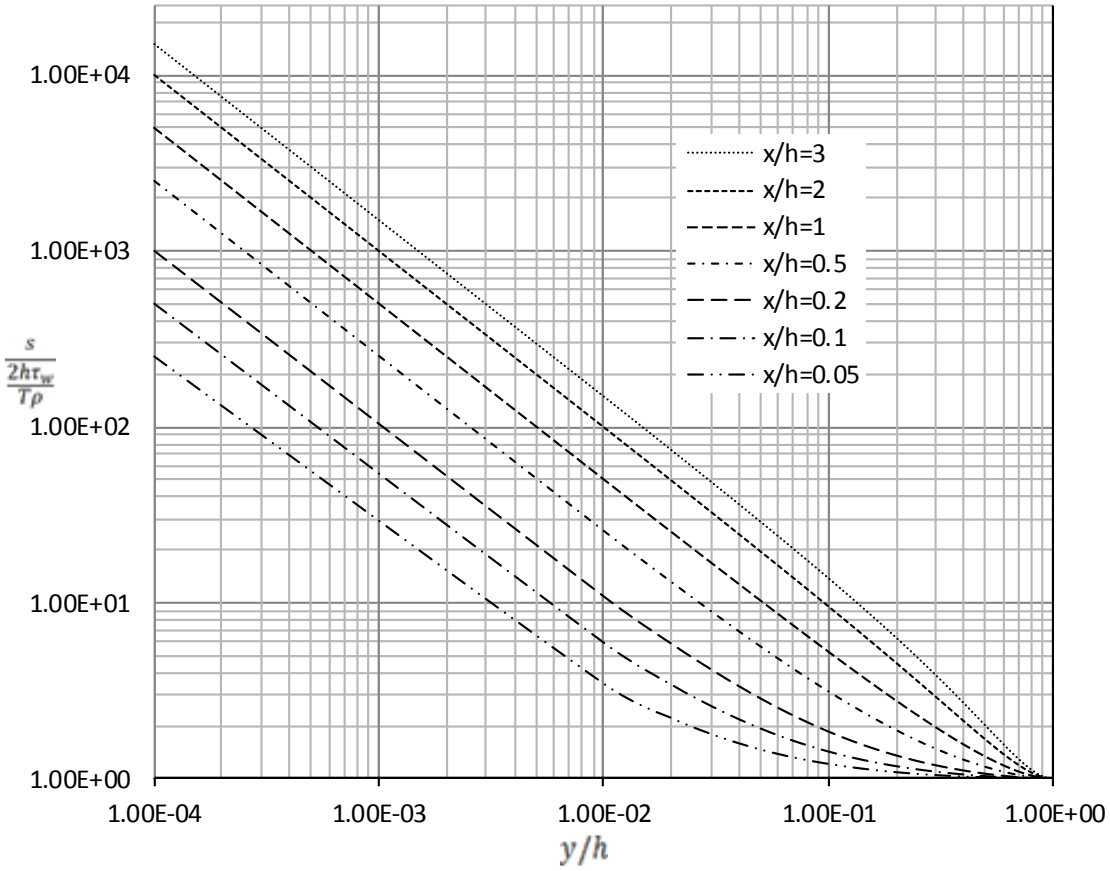

Figure 4-3: Entropy distribution

4.3. Entropy production rate in turbulent shear flow

4.3.1 Turbulent viscosity/dissipation model (TVD)

The velocity field is expressed by mean and fluctuating components as follows:

$$\mathbf{u} = \bar{\mathbf{u}} + \mathbf{u}' \tag{4.36}$$

where the $\bar{\mathbf{u}}$ and $\mathbf{u}'$ notations refer to mean and fluctuating components associated with the Reynolds averaging. Performing time averaging of Eq. (4.21),

$$\bar{\dot{P}}_S = \frac{\mu}{T}\left[\left(\nabla\bar{\mathbf{u}} + \nabla\overline{\mathbf{u}^{\mathbf{T}}}\right):\nabla\bar{\mathbf{u}}\right] + \frac{\mu}{T}\left[\left(\nabla\mathbf{u}' + \nabla\mathbf{u}'^{\mathbf{T}}\right):\nabla\bar{\mathbf{u}}\right] + \frac{\mu}{T}\overline{\left[\left(\nabla\mathbf{u}' + \nabla\mathbf{u}'^{\mathbf{T}}\right):\nabla\mathbf{u}'\right]} \quad (4.37)$$

Modeling of Eq. (4.37) represents a challenge to explicitly expressing the mean entropy production in terms of other mean flow variables alone. Two different approaches for expressing the mean entropy production will be considered below.

The first term on the right side of Eq. (4.37) is expressed as the mean flow entropy generation term:

$$\Phi_\mu = \bar{\boldsymbol{\tau}}:\nabla\bar{\mathbf{u}} \quad (4.38)$$

where $\bar{\boldsymbol{\tau}}$ is the Reynolds averaged shear stress expressed in terms of the mean velocity and $\bar{\boldsymbol{\tau}}$ is expressed as follows:

$$\bar{\boldsymbol{\tau}} = \mu\left(\nabla\bar{\mathbf{u}} + \nabla\overline{\mathbf{u}^{\mathbf{T}}}\right) \quad (4.39)$$

Simplified models, based on the eddy viscosity for the mean entropy generation, have been documented in past literature [51], [99] , [53]. The linear eddy viscosity model assumes a Boussinesq relationship between the turbulent stresses (second moments) and the mean strain rate tensor through an isotropic eddy viscosity. These simplified models have not been fully validated against experimental data regarding the turbulence correlations of entropy production that have been measured and reported in past literature.

Moore and Moore [51] developed the following correlations for mean entropy production, thermal diffusion, and viscous dissipation, respectively:

$$\boldsymbol{\tau_T} = \mu\left(\nabla\mathbf{u}' + \nabla\mathbf{u}'^{\mathbf{T}}\right) = \mu_T\left(\nabla\bar{\mathbf{u}} + \nabla\overline{\mathbf{u}^{\mathbf{T}}}\right) \quad (4.40)$$

where μ_T is the turbulent viscosity. In two-equation eddy viscosity models, such as the $k-\varepsilon$ model, μ_T is found by CFD as one of the solved turbulent quantities. The formulation uses the turbulent kinetic energy and energy dissipation as follows:

$$\mu_T = C_\mu\frac{k^2}{\varepsilon} \quad (4.41)$$

where $C_\mu = 0.09$ is a constant. The second term in Eq. (4.37) can be expressed as the eddy entropy term that results from the turbulent shear stress:

$$\Phi_T = \boldsymbol{\tau_T} : \nabla \bar{\mathbf{u}} \tag{4.42}$$

In turbulent shear flow, the energy budget of the total flow can be obtained by integrating the kinetic energy of the flow over a control volume [106]:

$$\frac{d}{dt}\int \frac{\mathbf{1}}{\mathbf{2}}\mathbf{u}\mathbf{u}\, dV = -\frac{1}{2}\nu \int (\nabla \mathbf{u} + \nabla \mathbf{u}^{\mathbf{T}})(\nabla \mathbf{u} + \nabla \mathbf{u}^{\mathbf{T}})dV = -\int \Delta dV \tag{4.43}$$

where Δ is the dissipation rate per unit mass. Decomposing Eq. (4.43) into mean and fluctuating components, the average dissipation rate can be rewritten as

$$\bar{\Delta} = \frac{1}{2}\nu\left(\nabla \bar{\mathbf{u}} + \nabla \overline{\mathbf{u}^{\mathbf{T}}}\right)\left(\nabla \bar{\mathbf{u}} + \nabla \overline{\mathbf{u}^{\mathbf{T}}}\right) + \frac{1}{2}\nu \overline{\left(\nabla \mathbf{u}' + \nabla \mathbf{u}'^{\mathbf{T}}\right)\left(\nabla \mathbf{u}' + \nabla \mathbf{u}'^{\mathbf{T}}\right)} \tag{4.44}$$

The quantity inside the average of the second term of Eq. (4.44) will be denoted as ε, where

$$\varepsilon = \frac{1}{2}\nu\left(\nabla \mathbf{u}' + \nabla \mathbf{u}'^{\mathbf{T}}\right)\left(\nabla \mathbf{u}' + \nabla \mathbf{u}'^{\mathbf{T}}\right) \tag{4.45}$$

The average value becomes

$$\bar{\varepsilon} = \frac{1}{2}\nu \overline{\left(\nabla \mathbf{u}' + \nabla \mathbf{u}'^{\mathbf{T}}\right)\left(\nabla \mathbf{u}' + \nabla \mathbf{u}'^{\mathbf{T}}\right)} \tag{4.46}$$

Subdividing into mean-flow and turbulent components and averaging, Eq. (4.43) becomes

$$\frac{d}{dt}\int \frac{\mathbf{1}}{\mathbf{2}}\bar{\mathbf{u}}\bar{\mathbf{u}}\, dV =$$

$$-\frac{1}{2}\nu \int \left[\left(\nabla \bar{\mathbf{u}} + \nabla \overline{\mathbf{u}^{\mathbf{T}}}\right)\left(\nabla \bar{\mathbf{u}} + \nabla \overline{\mathbf{u}^{\mathbf{T}}}\right) + \overline{\left(\nabla \mathbf{u}' + \nabla \mathbf{u}'^{\mathbf{T}}\right)\left(\nabla \mathbf{u}' + \nabla \mathbf{u}'^{\mathbf{T}}\right)}\right] dV \tag{4.47}$$

Eq. (4.47) shows how the total mean energy of the flow decays based on the mean flow and average turbulence dissipation components. The dissipation of the total energy due to the mean flow component is usually relatively small compared to the turbulence

contribution at high Reynolds numbers for many turbulent flows. Comparing Eq. (4.46) with (4.37), the third item on the right side of Eq. (4.37) can be written as

$$\Phi_D = \rho\bar{\varepsilon} \tag{4.48}$$

Substituting Eq. (4.38), (4.42), and (4.48) into Eq. (4.37) yields the entropy production rate

$$\bar{\dot{P}}_S = \frac{1}{T}\left(\Phi_\mu + \Phi_T + \Phi_D\right) \tag{4.49}$$

where Φ_D is the turbulent dissipation term. The value of the fluctuating velocity gradient $\nabla\mathbf{u}'$ increases rapidly with the Reynolds number, in contrast to the mean velocity gradient $\nabla\bar{\mathbf{u}}$.

4.3.2 Reynolds shear stress model (RSS)

The mean-flow momentum equation of turbulent flow can be written as

$$\rho\frac{D\bar{\mathbf{u}}}{Dt} = -\nabla\bar{p} + \nabla\cdot(\bar{\boldsymbol{\tau}} + \boldsymbol{\tau_R}) + \rho\mathbf{g} \tag{4.50}$$

where $\boldsymbol{\tau_R}$ is the Reynolds stress tensor.

$$\boldsymbol{\tau_R} = -\rho\overline{\mathbf{u}'\mathbf{u}'} \tag{4.51}$$

Substituting Eq. (4.16) into Eq. (4.8), based on the Gibbs equation, the entropy transport equation is written as

$$\frac{Ds}{Dt} = \frac{1}{T}\frac{De}{Dt} + \frac{p}{T\rho}\nabla\cdot\mathbf{u} \tag{4.52}$$

Taking averages of both sides of Eq. (4.52), the mean entropy time derivative becomes

$$\frac{D\bar{s}}{Dt} = \frac{1}{T}\frac{D\bar{e}}{Dt} + \frac{\bar{p}}{T\rho}\nabla\cdot\bar{\mathbf{u}} \tag{4.53}$$

Using Eq. (4.53), the entropy production rate for turbulent flow can be written as

$$\bar{\dot{P}}_S = \frac{1}{T}(\bar{\boldsymbol{\tau}}:\nabla\bar{\mathbf{u}} + \boldsymbol{\tau_R}:\nabla\bar{\mathbf{u}}) \tag{4.54}$$

Alternatively, define

$$\Phi_{\boldsymbol{R}} = \boldsymbol{\tau_R}:\nabla\overline{\mathbf{u}} \tag{4.55}$$

As a result, the model of entropy production can be expressed as follows:

$$\bar{\dot{P}}_s = \frac{1}{T}\left(\Phi_\mu + \Phi_{\boldsymbol{R}}\right) \tag{4.56}$$

In Eq. (4.56), $\Phi_{\boldsymbol{R}}$ represents the Reynolds shear dissipation. The fluctuating part of the turbulent flow interacts with the mean flow with a force of $-\nabla(\overline{\mathbf{u}'\mathbf{u}'})$ per unit mass.

4.4. Results and discussion

The DNS data [107] are obtained for a fully developed two-dimensional turbulent flow between two parallel walls with the Newtonian fluid having constant properties. The flow field is homogeneous both in the stream wise and span wise directions and the statistics are dependent only on the distance from the wall. The data in solutions are presented in dimensionless form. The flow is driven by the imposed pressure gradient according to the friction velocity, and the flow condition is defined with the channel height.

Table 4-1 shows six cases of turbulent flow between two parallel plates at different Reynolds numbers based on the friction velocity and the bulk mean velocity [107]. In Table 4-1, ν is kinematic viscosity, $u_{\boldsymbol{\tau}}$ is friction velocity, U_m is bulk mean velocity, and h is the channel half width.

Table 4-1: Six cases of turbulent flow between parallel plates

Case	$Re_\tau = hu_{\boldsymbol{\tau}}/\nu$	$Re_m = 2hU_{\boldsymbol{m}}/\nu$
1	109.4	3,220.4
2	150.5	4,586.2
3	211.0	6,666.0
4	297.9	10,039.1
5	395.8	13,924.9

6	642.5	24,272. 2

The numerical solutions of turbulence quantities are plotted from Figs. 4-4 to 4-7. Figure 4-4 illustrates the normalized mean velocity distribution across the half channel. It is observed that the velocity gradient increases with the increase in Reynolds number. Compared with the curve for laminar channel flow showed in Fig. 4-2, the velocity profiles for the turbulent flows are flat in the center of the channel compared to the laminar flow. .

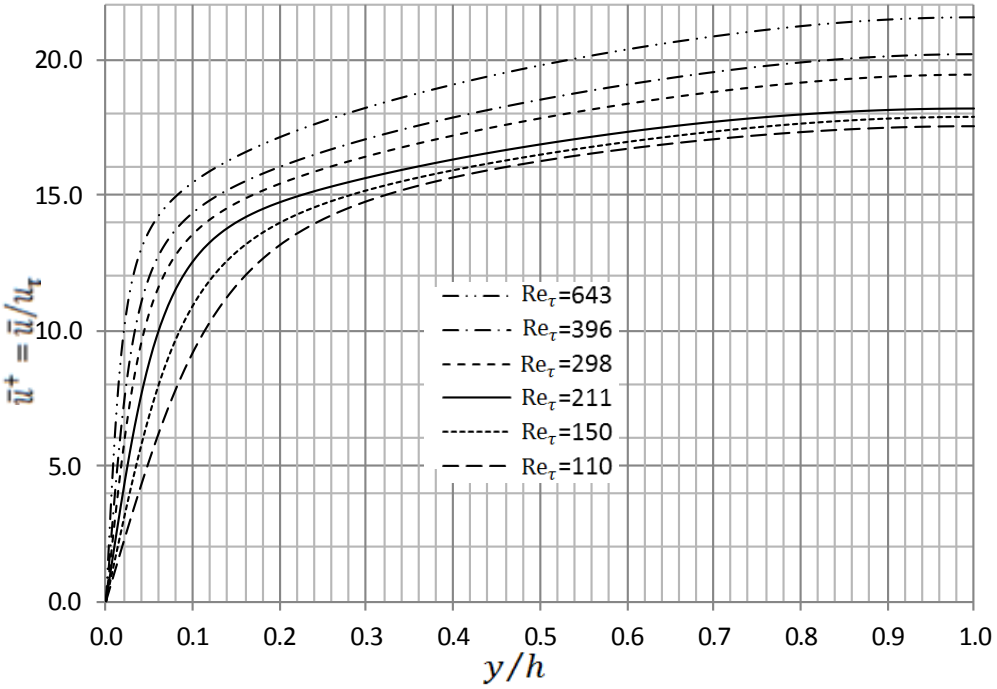

Figure 4-4: Mean velocities across the half channel height

Figure 4-5 shows the Reynolds shear stresses across the half channel. For different Reynolds number, the curves present consistency, meaning that the larger the Reynolds number, the closer to the wall the maximum value. It also shows that the Reynolds shear stresses increases with increase in Reynolds number.

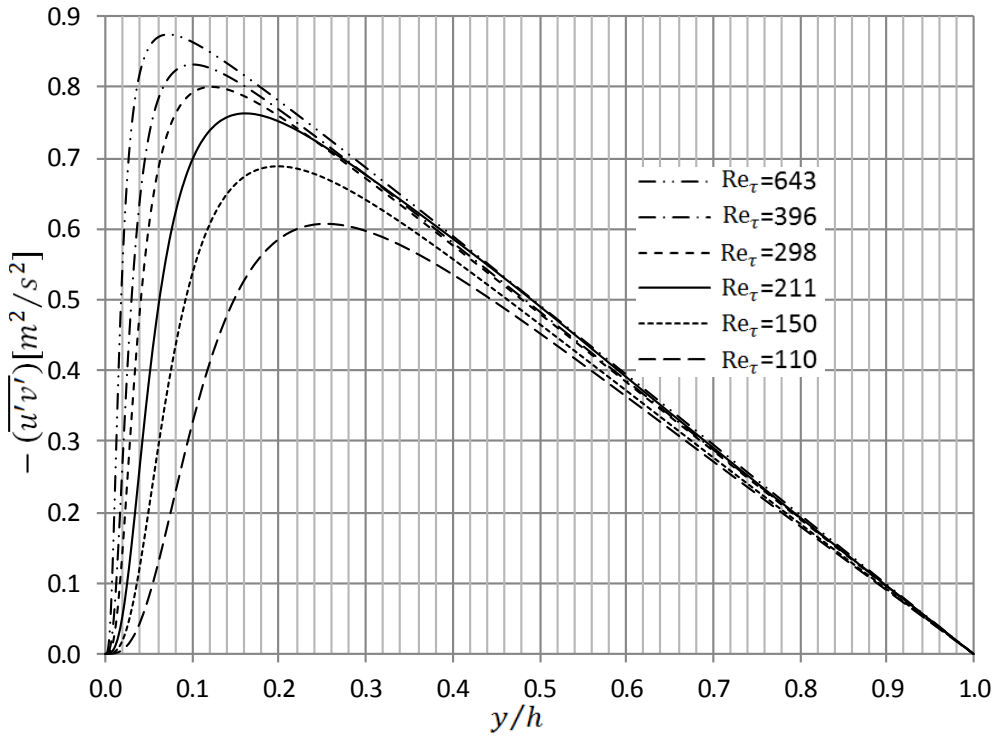

Figure 4-5: Reynolds shear stresses across the half channel height

Figure 4-6 shows the kinetic energy production across the half channel. The variations of the values are steeper near the wall for large Reynolds numbers than small ones. Also with the increase in Reynolds number, the maximum value increases. The kinetic energy production is the key parameter for configuring eddy viscosity for k-ε turbulent model when solving RANS.

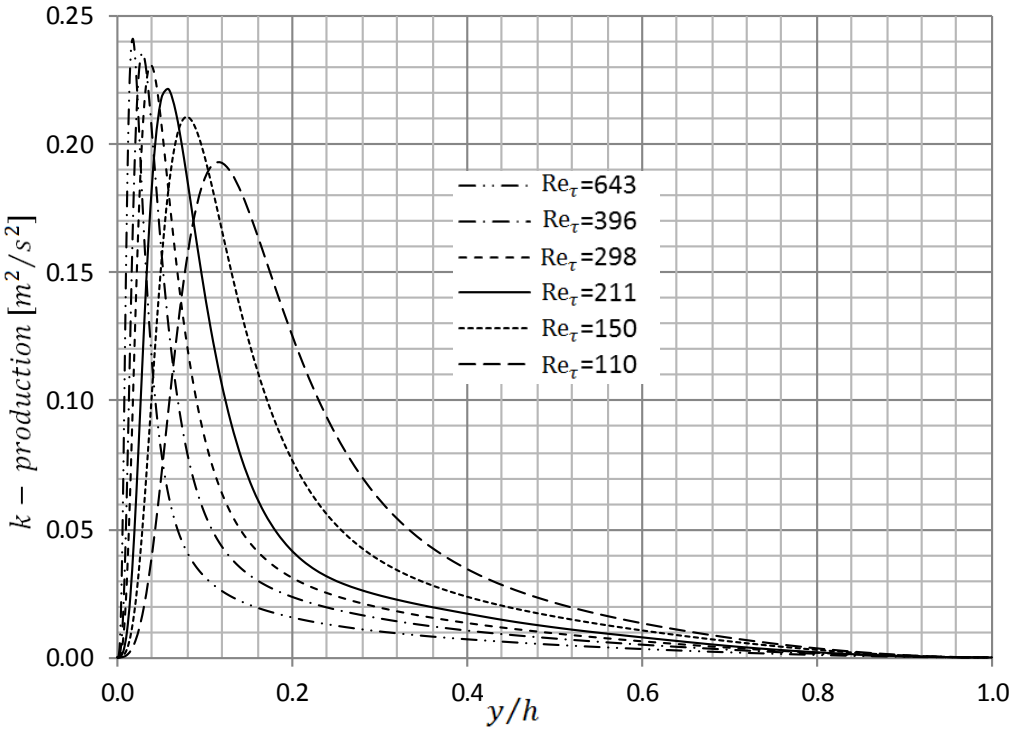

Figure 4-6: Kinetic energy production across the half channel height Re_τ

Figure 4-7 shows the kinetic energy dissipation rate across the half channel. Since it can act only to reduce the kinetic energy of the flow, it causes a negative rate of change of kinetic energy. This is a dissipated exergy associated with eddies in turbulent flow which is resulted from the fluctuating viscous stresses in resisting deformation of the fluid material. In RANS, the kinetic energy dissipation along with the kinetic energy forms eddy viscosity.

From above figures for DNS solutions of turbulent channel flow, two different numerical models of entropy production for turbulent flow are constructed.

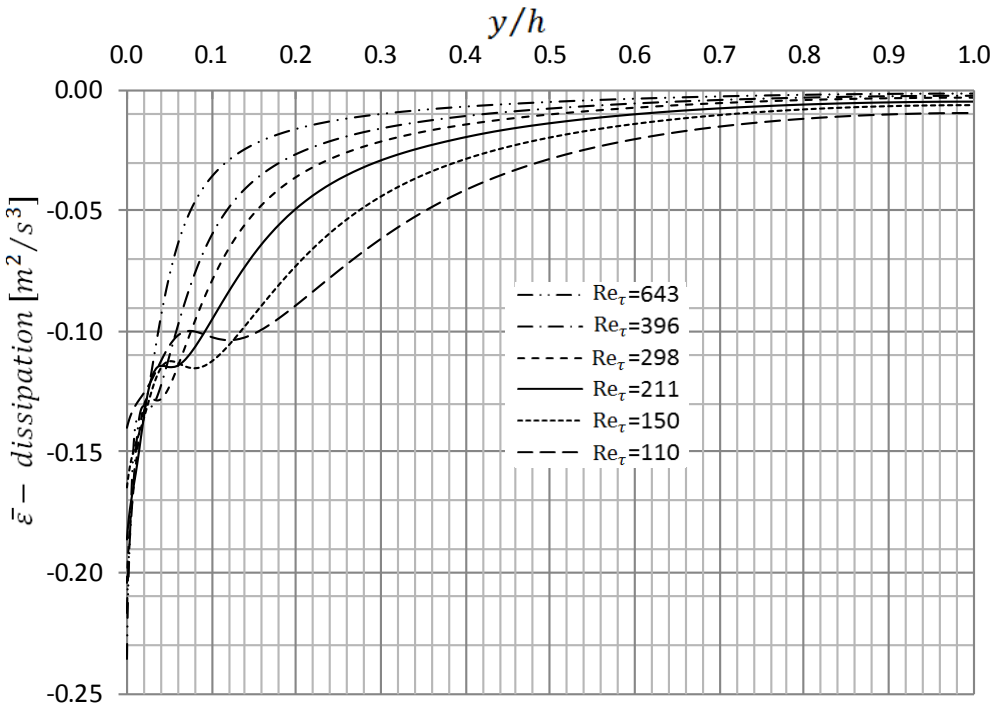

Figure 4-7: Kinetic energy dissipation across the half channel height

Further attention is focused on the accuracy of the models in predicting the energy dissipation. Similar to the laminar cases discussed above, the destroyed exergy is calculated by integrating the entropy production across the section while the energy balance method is used to verify the loss of kinetic energy in the flow passing the section against the exergy destruction.

Fig. 4-8 shows the viscous dissipation of the mean velocity field. This formulation is similar to the situation in laminar flow, which is considered the main loss in viscous sheared flow, either in laminar or turbulent flow. In such cases, the flow is driven by pressure gradient opposite the flow direction, and the none-slip boundary condition is the source of friction force that forms the velocity gradient. The friction force has the opposite direction of the flow and does useless work consuming the kinetic energy.

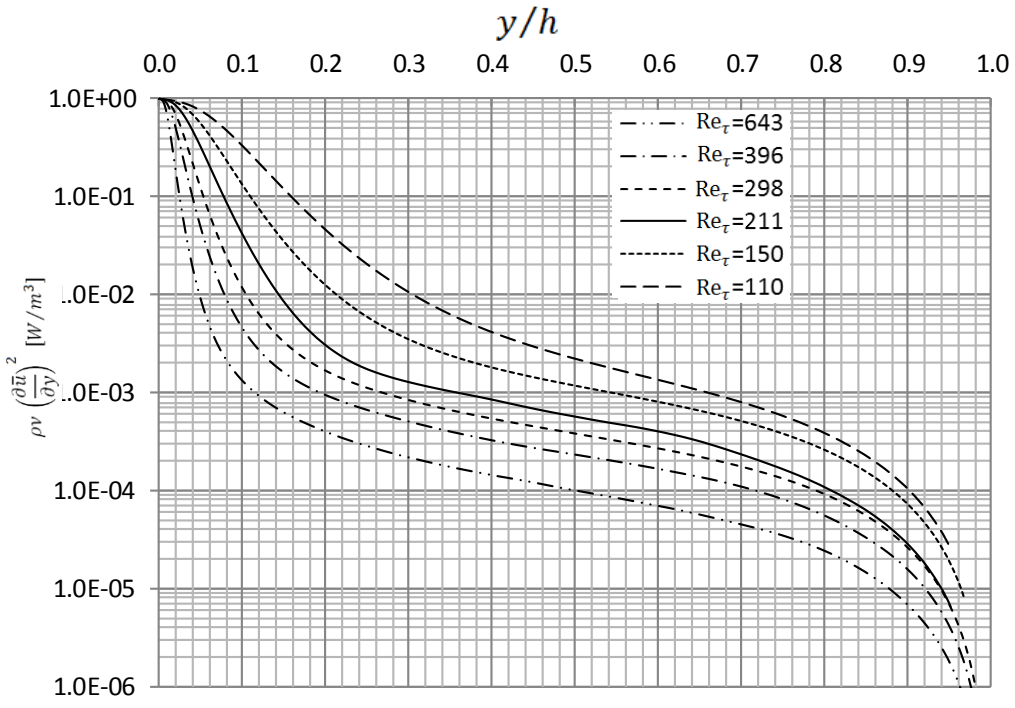

Figure 4-8: Irreversibility due to mean viscous stress across the half channel height

Fig.4-9 illustrates the irreversibility due to the eddy viscous stresses, $\nu_T\left(\frac{\partial\bar{u}}{\partial y}\right)$, across the half channel height. The eddy viscosity, ν_T, can be found by Eq. (4.41), based on the results of the turbulent kinetic energy and energy dissipation in Figs. (4-6) and (4-7). Fig. 4-10 illustrates the dissipation due to the Reynolds shear stress $-\rho\overline{u'v'}$.

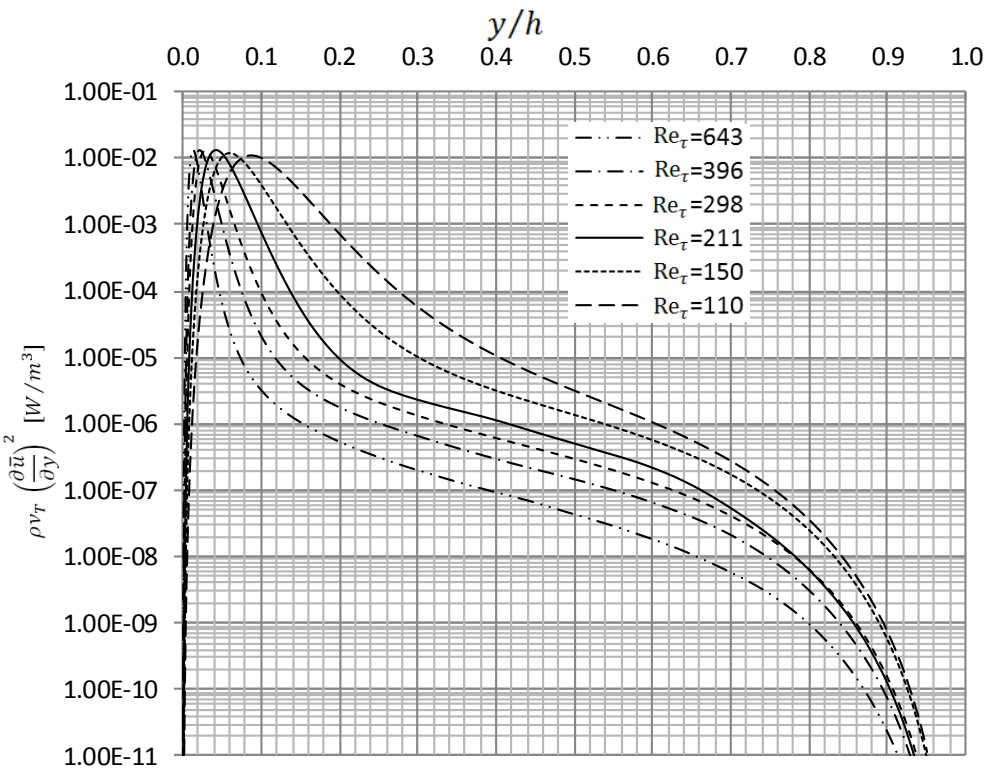

Figure 4-9: Irreversibility due to turbulent viscous stresses across the half channel height

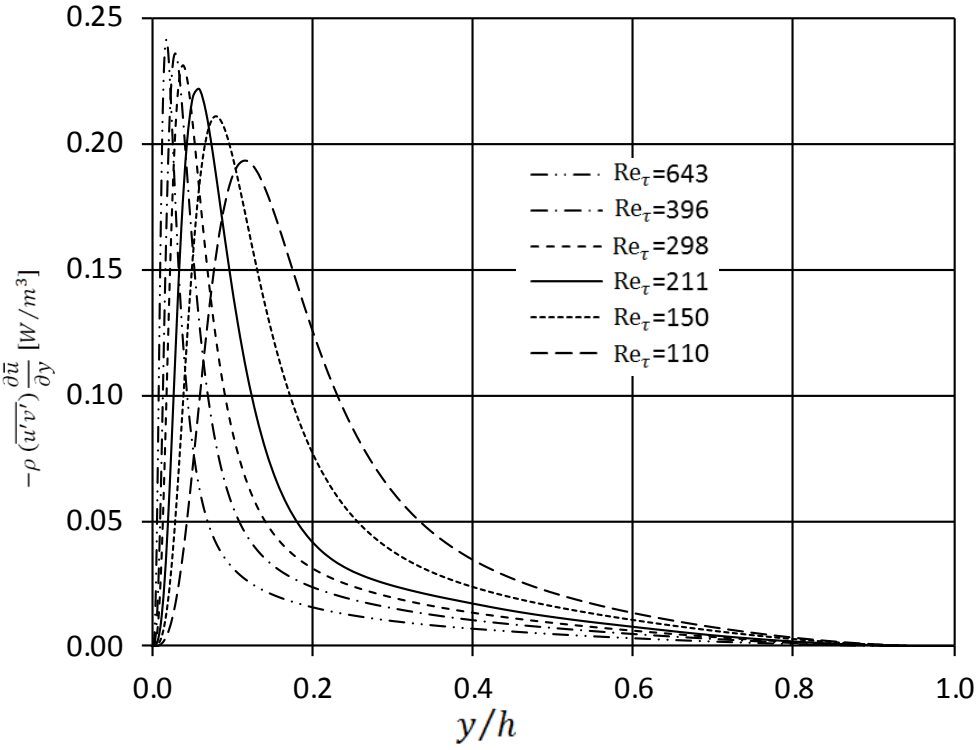

Figure 4-10: Irreversibility due to Reynolds shear stresses across the half channel height

The two models of entropy production rate for turbulent flow are based on the results of Figs. 4-7 to 4-10. The results are illustrated in Fig. 4-11, in which the curves represent the distributions of entropy production across the half-width of the channel at different Reynolds numbers.

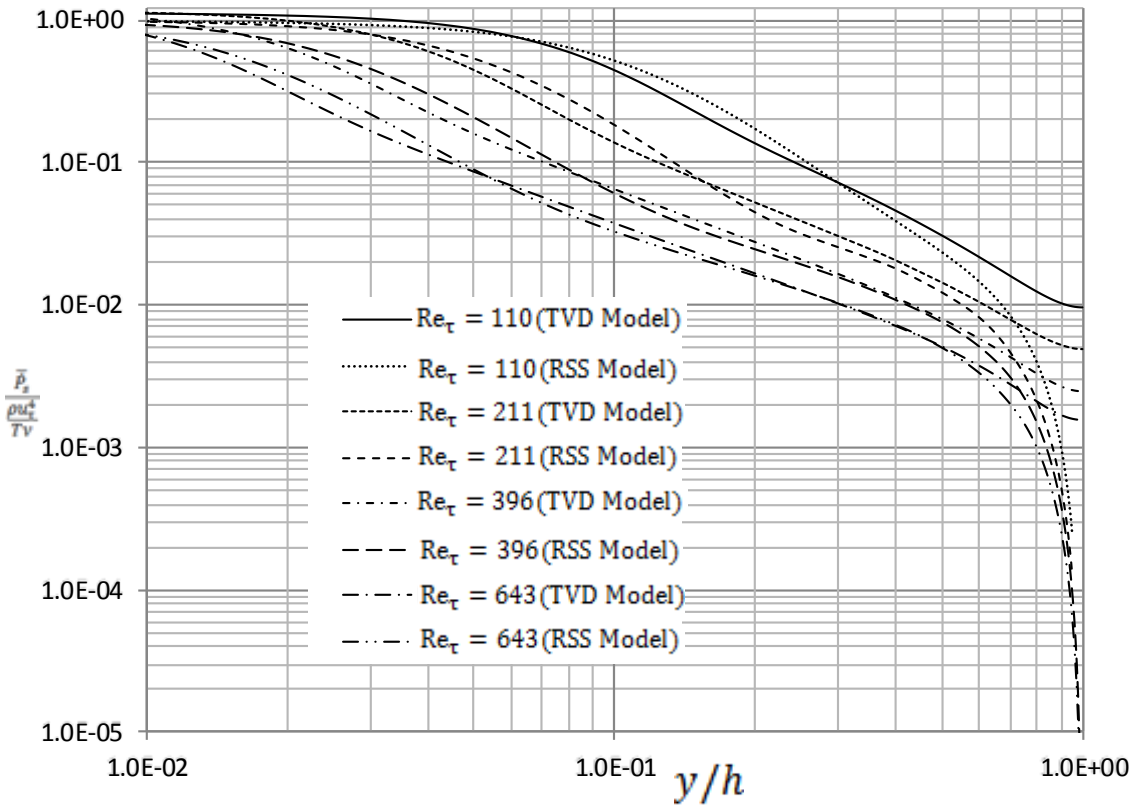

Figure 4-11: Entropy production rate across the half channel height (TVD = turbulent viscosity/dissipation model; RSS = Reynolds shear stress model)

The validations of the models are performed based on an energy balance method, similar to the case of laminar flow. The exergy destruction per unit length can be obtained by integration of entropy production rate across the half-width of the channel.

$$\dot{E}_x = \int_0^h T\dot{P}_s dy \tag{4.57}$$

The kinetic energy loss of the flow passing the section can be determined as follows:

$$\dot{Q} = \frac{\dot{m}}{\rho}\left(-\frac{\partial p}{\partial x}\right) \tag{4.58}$$

where $\dot{m}$ is the mass flow rate

$$\dot{m} = \int_0^h \rho\bar{u} dy \tag{4.59}$$

and $\frac{\partial p}{\partial x}$ is the pressure gradient in the flow direction.

$$\tau_w = -h\frac{\partial p}{\partial x}, \text{ and } \tau_w = \mu\left(\frac{\partial \bar{u}}{\partial y}\right)_{y=0} \tag{4.60}$$

The exergy destruction and thermal energy are calculated using Eqs. 4.57 and 4.58. The comparisons and resulting errors are summarized in Table 4-2. Results indicate that both entropy models predict the irreversible losses in terms of energy balances with good accuracy.

Table 4-2: Comparison of models

$Re_\tau = hu_\tau/\nu$		110	150	210	298	396	643
Heat transfer $[W]$	$\dot{Q} = \frac{\dot{m}}{\rho}\left(-\frac{\partial p}{\partial x}\right)$	0.134	0.101	0.075	0.057	0.044	0.029
TVD Model $[W]$	$\dot{E}_x = \int_0^h \left(\Phi_\mu + \Phi_T + \Phi_D\right)dy$	0.130	0.099	0.072	0.056	0.044	0.029
	Error $= \frac{\dot{Q} - E_x}{\dot{Q}} \times 100\%$	3.420	2.551	4.645	1.339	1.052	2.192
RSS Model $[W]$	$\dot{E}_x = \int_0^h \left(\Phi_\mu + \Phi_{\boldsymbol{R}}\right)dy$	0.129	0.098	0.071	0.055	0.044	0.030
	Error $= \frac{\dot{Q} - E_x}{\dot{Q}} \times 100\%$	4.106	3.169	5.197	2.104	1.812	2.872

For the channel flow problem, the entropy transport equation of turbulent flow becomes

$$\bar{u}\frac{\partial \bar{s}}{\partial x} = \bar{P}_s \tag{4.61}$$

Using the predicted results of entropy production and solving for the mean specific entropy gives

$$\bar{s} = \int \frac{\overline{\dot{P}_s}}{\bar{u}} dx \tag{4.62}$$

The results of the mean specific entropy $\bar{s}$ are plotted in Fig. 4-12.

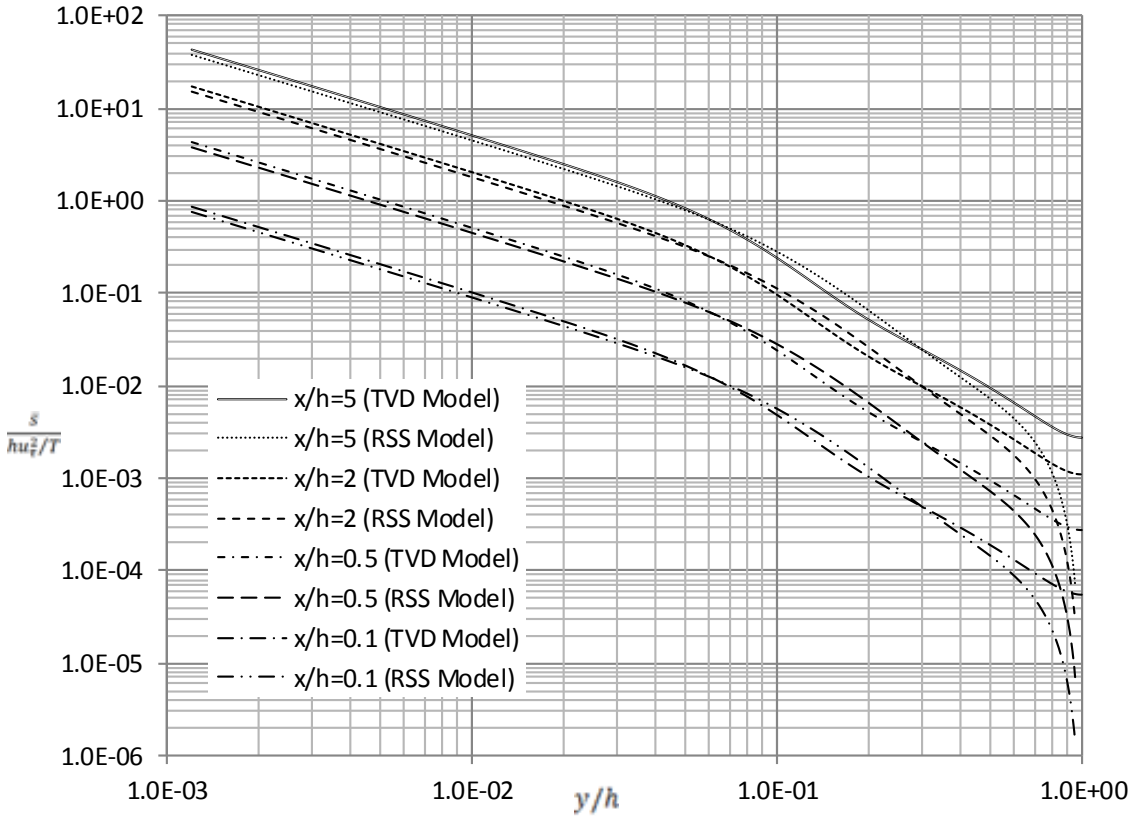

$(a)\ Re_\tau = 110$

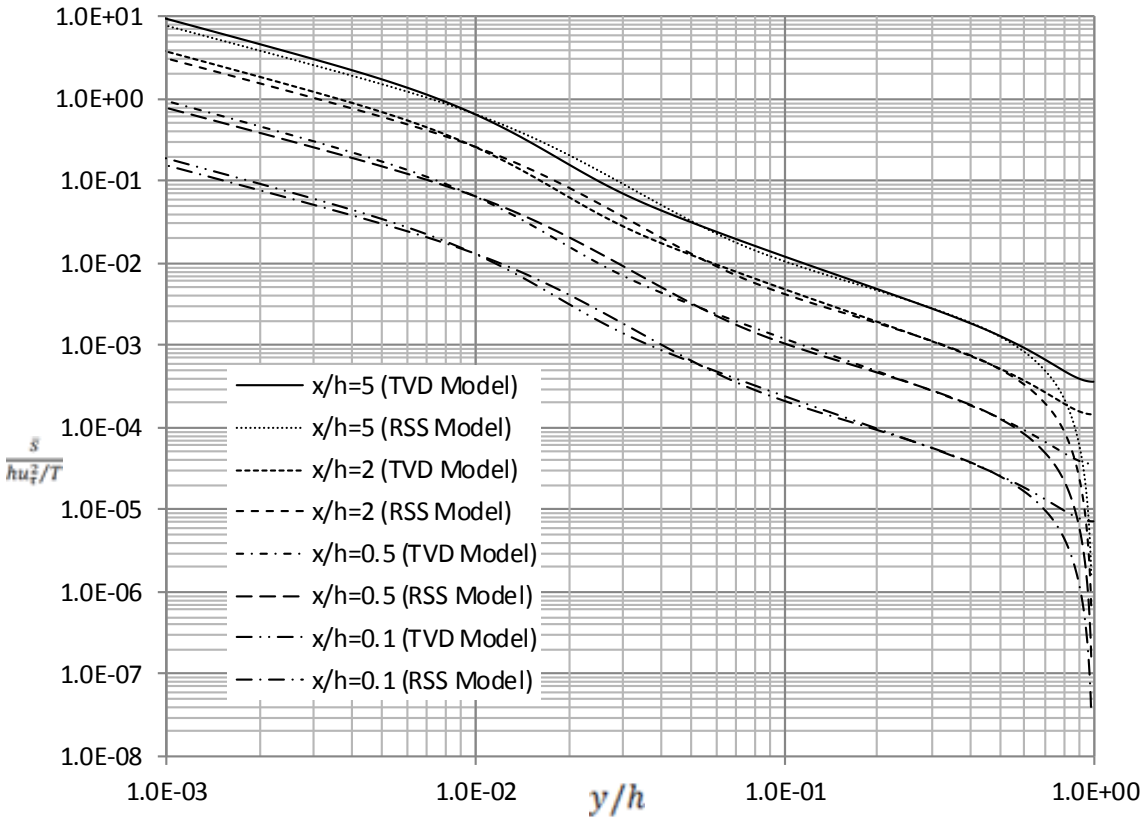

$(b)\ Re_\tau = 643$

Figure 4-12: Mean specific entropy across the half channel height (TVD = turbulent viscosity/dissipation model; RSS = Reynolds shear stress model)

The TVD model (turbulent viscosity/dissipation model) in Eq. (4.49) predicts that entropy production arises from dissipation due to the mean flow motion and turbulence dissipation. Fig. 4-8 illustrates the logarithmic representation of the viscous dissipation, Φ_μ. The distribution of dissipation rate is similar to the laminar flow case.

Near the vicinity of the wall, the gradient of mean velocity has a maximum value that is dominant by contributing about 90% of the total entropy production. However, it decreases rapidly near the wall because the gradient of the mean velocity decreases significantly. As a result, the mean dissipation rate gradually declines to zero near the

center line. Compared with the case of laminar flow, this change in mean dissipation rate near the wall area is more significant.

The turbulent viscous dissipation, Φ_T, in Eq. (4.49) is plotted in Fig. 4-9. This term contributes less to the total. From the wall to a distance of about 10% away from the wall, the dissipation rate has a sudden increase up to 0.02. Naterer and Adeyinka [78] neglected this term. The third term in Eq. (4.49) is the kinetic energy dissipation, Φ_D. The variable $\bar{\varepsilon}$ differs from the dissipation of turbulent kinetic energy in the standard $k-\varepsilon$ model [108]. This kinetic energy dissipation becomes more dominant near the wall and progressively declines. This trend can be observed in Fig. 4-7.

The alternative model of entropy production in Eq. (4.36), the RSS model (Reynolds shear stress model), was derived from the RANS equations. The first dissipation term is Φ_μ, and the second term, $\Phi_{\boldsymbol{R}}$, represents the Reynolds shear dissipation resulting from the velocity fluctuation. It can be interpreted as the work done by the force $-\nabla(\overline{\mathbf{u}'\mathbf{u}'})$ in the streamwise direction and dissipated to thermal energy. The curves of the dissipation rate at various Reynolds numbers are shown in Fig. 4-10. The dissipation rate increases to a maximum value near the wall. Beyond the maximum, the curves suddenly decline then gradually decrease. They approach zero at the center line because of the zero mean velocity gradient.

The integral values of the entropy production rate are obtained by the integration of the values shown in Fig. 4-11. The validation of the models was performed based on an energy balance. Table 4-2 summarizes the integral values for the two models. The comparisons are made between the destroyed exergy and the dissipated thermal energy. It shows that the TVD model predicts the local loss with higher precision than the RSS

model. In Fig. 4-11, the curves from the wall to the distance of about 90% from the wall nearly overlap, and the difference occurs near the center line, where the gradient of mean velocity tends toward zero. The curves of the RSS model sharply drop to approximately zero while the curves of the TVD model have a slower decline. For this reason, the entropy generation near the center line is not captured as accurately with the RSS model, leading to an underestimated total loss across the section.

The mean specific entropy is obtained by integration of Eq. (4.62). The difference between the two models can be observed in Fig. 4-12. The curves of the RSS model are consistent with the TVD model beyond the center area, but they show a sharp decrease when approaching the center line, where the gradient of mean velocity tends toward zero.

4.5 Summary

The new formulations of entropy production for turbulent flows were developed in this chapter. An energy balance method was used to validate and verify the models. The specific entropy was solved based on analytical and numerical methods. A comparison between two different models of entropy production for turbulent flow was presented. Finally, the errors for different models were presented for an accuracy comparison. The results indicate that the entropy model for laminar flow exactly predicted the local loss through validation by the energy balance method. Two different models of entropy production rate for turbulent flow were derived from different perspectives. These models address the viscous layer and results outside of the layer. Both models slightly underestimated the irreversibility of the wall-bounded turbulent entropy production that can be observed in Table 4-2. However, overall they provide accurate predictions of the flow irreversibility, especially for center line losses in TVD

model. This chapter presented the fundamental method for study on entropy generation for single phase flow and the similar method will be used in two phase flow.

Chapter 5

Two-phase Eulerian averaged formulation of entropy production in cavitation flow

This chapter presents the formulation of entropy production for two-phase flow, including cavitating flow. This model is derived from the Gibbs and RANS equations. An inter-phase slip algorithm mixture model is applied to control over-coupling of phases. The Rayleigh-Plesset equation is used to model the rate of mass generation of vapor at the interface. The standard k-ε turbulence equations are used to predict turbulence in the cavitation flow. The CFD predictions include the analysis of the force and cavitation characteristics of a hydrofoil NACA 4412 section and the velocity distributions behind a Propeller 5168 via CFD results and water tunnel experimental data. The results prove that the concerning entropy production of two-phase cavitating flow around a hydrofoil can be correlated to the loss of kinetic energy.

5.1 Problem formulation and governing equations

The model is expressed in terms of four field equations: the mixture continuity, momentum, vapor continuity, and algebraic equations. Each algebraic equation addresses the slip velocity of the vapor phase relative to the fluid phase. The governing equations for continuity and momentum of the mixture are:

$$\frac{\partial}{\partial t}(\rho_m) + \nabla \cdot (\rho_m \mathbf{u}_m) = 0 \tag{5.1}$$

$$\rho_m \frac{\partial \mathbf{u}_m}{\partial t} + \nabla \cdot (\rho_m \mathbf{u}_m \mathbf{u}_m) = -\nabla p_m + \nabla \cdot (\boldsymbol{\tau}_m + \boldsymbol{\tau}_{Tm}) + \nabla \cdot \boldsymbol{\tau}_{Dm} + \rho_m \mathbf{g} \tag{5.2}$$

where ρ_m is the mixture density and $\mathbf{u}_m$ is the mixture velocity. They are defined by

$$\rho_m \equiv \alpha_v \rho_v + (1 - \alpha_v)\rho_l \tag{5.3}$$

$$\mathbf{u}_m \equiv \frac{\alpha_v \rho_v \mathbf{u}_v + (1-\alpha_v)\rho_l \mathbf{u}_l}{\rho_m} \tag{5.4}$$

where α_v refers to the volume fraction of the vapor phase. The density of vapor, ρ_v, and liquid, ρ_l, are assumed constant.

The mechanical (kinetic) energy equation can be obtained by taking the dot product of the momentum equation and velocity, yielding

$$\rho_m \frac{D}{Dt}\left(\frac{1}{2}\mathbf{u_m^2}\right) = -\mathbf{u}_m \cdot \nabla p_m + \nabla \cdot (\boldsymbol{\tau}_m \cdot \mathbf{u}_m) - \boldsymbol{\tau}_m : \nabla \mathbf{u}_m + \nabla \cdot (\boldsymbol{\tau}_{Tm} \cdot \mathbf{u}_m) -$$

$$\boldsymbol{\tau}_{Tm} : \nabla \mathbf{u}_m + \nabla \cdot (\boldsymbol{\tau}_{Dm} \cdot \mathbf{u}_m) - \boldsymbol{\tau}_{Dm} : \nabla \mathbf{u}_m + \mathbf{u}_m \cdot \rho_m \mathbf{g} + \mathbf{u}_m \cdot \mathbf{M}_m \quad (5.5)$$

where $\mathbf{M}_m$ is the mixture momentum source term due to the surface tension effect. The total energy equation is given by

$$\rho_m \frac{D}{Dt}\left(e_m + \frac{1}{2}\mathbf{u_m^2}\right) = -\nabla \cdot \mathbf{q} - \nabla \cdot (p_m \mathbf{u}_m) + \nabla \cdot (\boldsymbol{\tau}_m \cdot \mathbf{u}_m) + \nabla \cdot (\boldsymbol{\tau}_{Tm} \cdot \mathbf{u}_m) +$$

$$\nabla \cdot (\boldsymbol{\tau}_{Dm} \cdot \mathbf{u}_m) + \mathbf{u}_m \cdot \rho_m \mathbf{g} + \dot{q} + E_m \quad (5.6)$$

where $\boldsymbol{e}_m$, $\dot{q}$, and $\boldsymbol{q}$ represent the internal energy, body heating, and heat flux, respectively. The mass fraction of the vapor phase is defined as

$$c_v = \frac{\alpha_v \rho_v}{\rho_m} \quad (5.7)$$

In Eq. (5.2), the diffusion stress, $\boldsymbol{\tau}_{Dm}$, can be expressed as a function of $\mathbf{u}_{lv}$ [96]:

$$\boldsymbol{\tau}_{Dm} = -\rho_m c_v (1 - c_v) |\mathbf{u}_{lv} \mathbf{u}_{lv}^T| \quad (5.8)$$

where the slip velocity is

$$|\mathbf{u}_{lv}| \mathbf{u}_{lv} = \frac{4}{3} \frac{d_v}{\alpha_v \rho_l C_D} \left\{ \alpha_v (\rho_v - \rho_m) \left[\mathbf{g} - \nabla \cdot (\mathbf{u}_m \mathbf{u}_m) - \frac{\partial \mathbf{u}_m}{\partial t} \right] \right\} \quad (5.9)$$

where d_v is the diameter of the bubble and C_D is the drag coefficient. The drag coefficient depends on the bubble Reynolds number, Re_v, which is defined as follows:

$$\mathrm{Re}_v = \frac{d_v \rho_l |\mathbf{u}_{lv}|}{\mu_l} \quad (5.10)$$

A general expression for the drag coefficient is given as follows:

$$C_D = \begin{cases} \frac{24}{\mathrm{Re}_v}(1 + 0.15\mathrm{Re}_v^{0.687}) & Re_v < 1000 \\ 0.44 & Re_v \geq 1000 \end{cases} \quad (5.11)$$

The correlations in Eq. (5.11) are used for spheres since it is assumed in this research that bubbles are spheres in order to apply Rayleigh-Plesset equation for phase change. Then the continuity equation for the vapor phase can be expressed in terms of $\mathbf{u}_{lv}$ as follows:

$$\frac{\partial}{\partial t}(\alpha_v \rho_v) + \nabla \cdot (\alpha_v \rho_v \mathbf{u}_m) = \Gamma_v - \nabla \cdot [\alpha_v \rho_v \mathbf{u}_{lv}(1 - c_v)] \quad (5.12)$$

The generalized stress includes the influence of both viscous shear stress and turbulent stress, which can be expressed as follows [109]:

$$\boldsymbol{\tau}_{Gm} = \boldsymbol{\tau}_m + \boldsymbol{\tau}_{Tm} \quad (5.13)$$

$$\boldsymbol{\tau}_{Gm} = (\mu_m + \mu_{Tm})\left[(\nabla \mathbf{u}_m + \nabla \mathbf{u}_m^T) - \frac{2}{3}(\nabla \cdot \mathbf{u}_m)\boldsymbol{I}\right] - \frac{2}{3}\rho_m k_m \boldsymbol{I} \quad (5.14)$$

where $\boldsymbol{I}$ is a unit tensor and $k_m$is the turbulent kinetic energy density for the mixture phase. The dynamic viscosity for the mixture μ_m is defined as

$$\mu_m = \alpha_v \mu_v + (1 - \alpha_v)\mu_l \quad (5.15)$$

The coefficient of the turbulent eddy viscosity for the mixture can be written in the following form like a single-phase flow:

$$\mu_{Tm} = \frac{C_{\mu m}\rho_m k_m^2}{\varepsilon_m} \quad (5.16)$$

Transport equations for the standard k-ε model for k (turbulent kinetic energy) and ε (dissipation rate of turbulent kinetic energy) are written as follows: [101]

$$\frac{\partial}{\partial t}(\rho_m k_m) + \nabla \cdot \left[(\rho_m k_m \mathbf{u}_m) - \left[\mu_m + \frac{\mu_{Tm}}{\sigma_{km}}\right]\nabla k_m\right] = P_k + P_b - \rho_m \varepsilon_m - Y_M + S_k \quad (5.17)$$

For dissipation ε,

$$\frac{\partial}{\partial t}(\rho_m \varepsilon_m) + \nabla \cdot \left[(\rho_m \varepsilon_m \mathbf{u}_m) - \left[\mu_m + \frac{\mu_{Tm}}{\sigma_{\varepsilon m}}\right] \nabla \varepsilon_m\right] = C_{1\varepsilon} \frac{\varepsilon_m}{k_m}(P_k + C_{3\varepsilon} P_b) -$$

$$C_{2\varepsilon} \rho_m \frac{\varepsilon_m^2}{k_m} + S_\varepsilon \tag{5.18}$$

For production of k,

$$P_k = -\rho_m \overline{\mathbf{u}_m' \mathbf{u}_m'} \nabla \cdot \mathbf{u}_m \tag{5.19}$$

$$P_k = \mu_{Tm} S^2 \tag{5.20}$$

where S is the modulus of the mean rate-of-strain tensor, defined as

$$S \equiv \sqrt{2 S_{ij} S_{ij}} \tag{5.21}$$

The effect of buoyancy is defined as

$$P_b = \beta \frac{\mu_{Tm}}{\mathrm{Pr}_{Tm}} \mathbf{g} \cdot \nabla T \tag{5.22}$$

where Pr_{Tm} is the turbulent Prandtl number for energy and g_i is the component of the gravitational vector in the i-th direction. For the standard and realizable models, the default value of Pr_{Tm} is 0.85. The coefficient of thermal expansion, β, is defined as

$$\beta = -\frac{1}{\rho_m}\left(\frac{\partial \rho_m}{\partial T}\right)_p \tag{5.23}$$

The model constants have the following default values:

$$C_{\mu m} = 0.09, C_{1\varepsilon} = 1.44, C_{2\varepsilon} = 1.92, \sigma_{km} = 1.0, \sigma_{\varepsilon m} = 1.3 \tag{5.24}$$

Cavitation is a process involving two-phase flow with a fluid phase and vapor bubbles. To describe turbulence in a cavitating flow, the standard k-ε turbulence equations can be used. The formulation will use the turbulent viscosity in terms of k and ε in the mixture momentum equation. The onset of flow cavitation is characterized by the cavitation number, defined as [103]:

$$C_a = \frac{p - p_v}{1/2 \rho_l u_l^2} \tag{5.25}$$

Thus, the total inter-phase mass transfer rate per unit volume can be derived from the Rayleigh-Plesset equation [103] as follows:

$$\Gamma_v = \frac{3\alpha_v \rho_v}{d_v}\sqrt{\frac{2}{3}\frac{p_v - p}{\rho_l}} \tag{5.26}$$

In Eq. (5.26) d_v is the diameter of bubble, where sphere geometry of bubble is assumed in Rayleigh-Plesset's derivation which governs the dynamics of a spherical bubble in a liquid.

5.2 Formulations of entropy production rate for two-phase flow

The second law can be written in terms of a Clausius–Duhem inequality [93] by using e as the internal energy, p as pressure, V as volume, T as the temperature, and s as the entropy. In the most general form, Eq. (4.52) can be written as

$$\frac{Ds}{Dt} = \frac{1}{T}\frac{De_m}{Dt} + \frac{p_m}{T\rho_m}\nabla \cdot \mathbf{u}_m \tag{5.27}$$

Combining Eqs. (5.5) and (5.6) and noting that

$$\nabla \cdot (p_m \mathbf{u}_m) = \mathbf{u}_m \cdot \nabla p_m + p_m \nabla \cdot \mathbf{u}_m \tag{5.28}$$

the internal energy equation e_m is

$$\rho_m \frac{De_m}{Dt} = -\nabla \cdot \mathbf{q} - p_m \nabla \cdot \mathbf{u}_m + (\boldsymbol{\tau}_m + \boldsymbol{\tau}_{Tm}) : \nabla \mathbf{u}_m + \boldsymbol{\tau}_{Dm} : \nabla \mathbf{u}_m + \dot{q} + E_m - \mathbf{u}_m \cdot \mathbf{M}_m \tag{5.29}$$

The second law can be written as a Clausius–Duhem inequality [93] as follows:

$$\frac{Ds}{Dt} + \nabla \cdot \left(\frac{\mathbf{q}}{T}\right) - \frac{\dot{q}}{T} \equiv \dot{P}_s \geq 0 \tag{5.30}$$

Combining Eqs. (5.27), (5.29), and (5.30), the entropy production rate for the mixture model of two-phase flow yields:

$$\dot{P}_s = \frac{1}{T}[-\nabla \cdot \mathbf{q} - p_m \nabla \cdot \mathbf{u}_m + (\boldsymbol{\tau}_m + \boldsymbol{\tau}_{Tm}) : \nabla \mathbf{u}_m + \boldsymbol{\tau}_{Dm} : \nabla \mathbf{u}_m + \dot{q} + E_m - \mathbf{u}_m \cdot \mathbf{M}_m] + \frac{p_m \rho_m}{T} \frac{D}{Dt}\left(\frac{1}{\rho_m}\right) + \nabla \cdot \left(\frac{\mathbf{q}}{T}\right) - \frac{\dot{q}}{T} \quad (5.31)$$

In Eq. (5.31),

$$\nabla \cdot \left(\frac{\mathbf{q}}{T}\right) = \frac{T\nabla \cdot \mathbf{q} - \mathbf{q} \cdot \nabla T}{T^2} \quad (5.32)$$

From Fourier's law,

$$\mathbf{q} = -K \cdot \nabla T \quad (5.33)$$

$$\frac{D}{Dt}\left(\frac{1}{\rho_m}\right) = \frac{1}{\rho_m} \nabla \cdot \mathrm{u_m} \quad (5.34)$$

Eq. (5.31) becomes:

$$\dot{\mathrm{P}}_\mathrm{s} = \frac{1}{T}[(\boldsymbol{\tau}_m + \boldsymbol{\tau}_{Tm}) : \nabla \mathbf{u}_m + \boldsymbol{\tau}_{Dm} : \nabla \mathbf{u}_m + E_m - \mathbf{u}_m \cdot \mathbf{M}_m] + \frac{K_m \nabla T \cdot \nabla T}{T^2} \quad (5.35)$$

Eq. (5.35) can be defined as follows:

$$\dot{P}_s = \frac{1}{T}\left[\Phi_m^{\mu} + \Phi_m^{T} + \Phi_m^{D} + \Phi_m^{\sigma}\right] + \frac{K_m \nabla T \cdot \nabla T}{T^2} \quad (5.36)$$

Four different effects are defined as follows:

$\Phi_m^{\mu} = \boldsymbol{\tau}_m : \nabla \mathbf{u}_m$ mixture viscous dissipation (5.37)

$\Phi_m^{T} = \boldsymbol{\tau}_{Tm} : \nabla \mathbf{u}_m$ mixture turbulent work effect (5.38)

$\Phi_m^{D} = \boldsymbol{\tau}_{Dm} : \nabla \mathbf{u}_m$ diffusion stress effect (5.39)

$\Phi_m^{\sigma} = E_m - \mathbf{u}_m \cdot \mathbf{M}_m$ energy source effect and surface tension effect from interfaces (5.40)

where Φ_m^{D} is the diffusion stress effect and can be expressed as a function of $\boldsymbol{u}_{lv}$, and Φ_m^{σ} is the energy source effect and surface tension effect based on the interacting continua having two different items to be defined.

$$\mathbf{M}_m = 2H_{pc}\sigma \nabla \alpha_p + \mathbf{M}_m^{H} \quad (5.41)$$

In Eq. 5.41, H_{pc} and σ are the average mean curvature of interfaces and the surface tension. $\mathbf{M}_m^H$ accounts for the effect of changes in the mean curvature,

$$E_m = T\left(\frac{\partial\sigma}{\partial T}\right)\frac{D_i a_i}{Dt} + 2H_{pc}\sigma\frac{\partial\alpha_l}{\partial t} + E_m^H \tag{5.42}$$

where T, a_i, α_l, and E_m^H are mean interface temperature, interfacial area concentration, void fraction of liquid phase, and mixture energy gain due to changes in the mean curvature, respectively.

The interfacial energy source E_m complicates the formulation significantly. With very few exceptions, this term can be neglected relative to the large-energy exchanges that involve latent heat of phase change.

The interfacial momentum transfer condition $\mathbf{M}_m$ is preserved in the averaged formulation to obtain the drag force balance for the mixture model. Substituting Eqs. (5.41) and (5.42), Eq. (5.40) becomes

$$\Phi_m^\sigma = T\left(\frac{\partial\sigma}{\partial T}\right)\frac{D_i a_i}{Dt} + 2H_{pc}\sigma\frac{\partial\alpha_l}{\partial t} + E_m^H - 2H_{pc}\sigma\left(\mathbf{u}_m\cdot\nabla\alpha_p\right) - \mathbf{u}_m\cdot\mathbf{M}_m^H \tag{5.43}$$

Note that

$$\alpha_l = 1 - \alpha_p \tag{5.44}$$

which yields

$$\Phi_m^\sigma = T\left(\frac{\partial\sigma}{\partial T}\right)\frac{D_i a_i}{Dt} - 2H_{pc}\sigma\left(\frac{\partial\alpha_p}{\partial t} + \mathbf{u}_m\cdot\nabla\alpha_p\right) + E_m^H - \mathbf{u}_m\cdot\mathbf{M}_m^H \tag{5.45}$$

In addition, note that

$$E_m^H - \mathbf{u}_m\cdot\mathbf{M}_m^H = 0 \tag{5.46}$$

$$\frac{\partial\alpha_p}{\partial t} + \mathbf{u}_m\cdot\nabla\alpha_p = \Gamma_p - \nabla\cdot\left(\alpha_p\mathbf{u}_{Mp}\right) \tag{5.47}$$

Eq. (5.47) becomes

$$\Phi_m^\sigma = T\left(\frac{\partial\sigma}{\partial T}\right)\frac{D_i a_i}{Dt} + 2H_{pc}\sigma\left[\nabla\cdot\left(\alpha_p\mathbf{u}_{Mp}\right) - \Gamma_p\right] \tag{5.48}$$

and substituting Eq. (3.53) into (5.48) results in

$$\Phi_m^{\sigma} = T\left(\frac{\partial \sigma}{\partial T}\right)\frac{D_i a_i}{Dt} + 2H_{pc}\sigma\left\{\nabla\cdot\left[\alpha_p(1-c_p)\mathbf{u}_{Cp}\right] - \Gamma_p\right\} \tag{5.49}$$

For cavitation flow, the Rayleigh-Plesset equation can be used to model Γ_p. Substituting Eq. (5.26) and the following expression into (5.49) renders

$$\mathbf{u}_{Cp} = \mathbf{u}_{Cp0} + \frac{D_{Mp}}{\alpha_p}\nabla\alpha_p \tag{5.50}$$

Eq. (5.49) becomes

$$\Phi_m^{\sigma} = T\left(\frac{d\sigma}{dT}\right)\frac{D_i a_i}{Dt} + 2H_{pc}\sigma\left\{\nabla\cdot\left[\alpha_p(1-c_p)\left(\mathbf{u}_{Cp0} + \frac{D_{Mp}}{\alpha_p}\nabla\alpha_p\right)\right] - \frac{3\alpha_v\rho_v}{d_v}\sqrt{\frac{2}{3}\frac{p_v-p}{\rho_l}}\right\} \tag{5.51}$$

For the $k-\varepsilon$ model, the diffusion coefficient D_{Mp} is given by

$$D_{Mp} = \frac{\mu_m}{\rho_m}\left(1 + 0.85\,\frac{\mathrm{u}_{Cp}^2}{2k/3}\right)^{-\frac{1}{2}} \tag{5.52}$$

where $\mathbf{u}_{Cp0}$ can be modeled in different forms depending on the cases. The general form is given as follows:

$$|\mathbf{u}_{Cp0}|\mathbf{u}_{Cp0} = \frac{4}{3}\frac{d_p}{\alpha_v\rho_C C_D}\left\{\alpha_v(\rho_p-\rho_m)\left[\mathbf{g} - \nabla\cdot(\mathbf{u}_m\mathbf{u}_m) - \frac{\partial \mathbf{u}_m}{\partial t}\right]\right\} \tag{5.53}$$

After further approximations eliminating $(\mathbf{u}_m\cdot\nabla)\mathbf{u}_m$, instead of the pressure gradient, equation (5.53) becomes

$$|\mathbf{u}_{Cp0}|\mathbf{u}_{Cp0} = \frac{4}{3}\frac{d_p}{\rho_C C_D}\frac{\nabla p}{\rho_m}(\rho_p-\rho_m) \tag{5.54}$$

In equation (5.51), the transport equation for the interfacial area concentration is

$$\frac{D_i a_i}{Dt} = \frac{\partial a_i}{\partial t} + \mathbf{u}_i\cdot\nabla a_i = \Phi_L \tag{5.55}$$

where $\mathbf{u}_i$ is the velocity of the interface and Φ_L is the source term expressed by various parameters. The average interface velocity, $\mathbf{u}_i$, can be given approximately by

$$\mathbf{u}_i = \mathbf{u}_p - \frac{\Gamma_p}{\rho_p a_i^2} \nabla \alpha_v \approx \mathbf{u}_p \tag{5.56}$$

where $\mathbf{u}_p$ is the velocity of dispersed phase. In bubbly two-phase flow, it is the bubble velocity. In Eq. (5.56), it is assumed that the volume fraction gradient of vapour phase can be neglected [93].

The constitutive equation for H_{pc} is given as follows:

$$H_{pc} = \frac{a_i}{3C^i \alpha_p} \tag{5.57}$$

where the factor C^i is 1 for fairly uniform spherical droplets or bubbles. The most well-known empirical correlation of the interfacial area concentration in bubble columns would be Akita–Yoshida's correlation [110] given by

$$a_i = \frac{1}{3D_H} \left(\frac{gD_H^2 \rho_c}{\sigma}\right)^{0.5} \left(\frac{gD_H^3}{\nu_c^2}\right)^{0.1} \alpha_p^{1.13} \tag{5.58}$$

Kocamustafaogullari et al. [111] developed the following theoretical model for interfacial area concentration based on the average pressure fluctuations generated by the turbulent liquid fluctuations acting across a bubble diameter and the competing surface tension force:

$$a_i = \frac{8.49}{D_H^{0.44}} \left(\frac{\sigma}{\rho_c}\right)^{-0.33} \alpha_p^{0.78} \varepsilon_m^{0.22} \tag{5.59}$$

Another modified correlation from the same author can be expressed from the following equation:

$$a_i = \frac{3.02 g^{0.174}}{D_H^{0.335} \nu_c^{0.239}} \left(\frac{\sigma}{\rho_c - \rho_p}\right)^{-0.174} \alpha_p \varepsilon_m^{0.0769} \tag{5.60}$$

where a_i, D_H, g , σ, ν_c , and ε are the interfacial area concentration, the equivalent hydraulic diameter, the gravitational acceleration, the surface tension, the kinematic viscosity of liquid, and the energy dissipation rate per unit mass, respectively.

5.3 Numerical formulation and validation of fluid flow equations

Obtaining DNS solution of the Navier–Stokes equations for turbulent flow is difficult. Because the flow involves significantly different mixing-length scales, the solutions need a fine resolution of mesh that makes the computations very time consuming. Any easy way to solve turbulent flow using a laminar model associated with a coarse mesh usually results in a time-unsteady solution. Hence, an Eulerian averaged model such as the Reynolds-averaged Navier–Stokes equations (RANS) is used in practical CFD applications when modeling turbulent flows.

For two-phase flow (including cavitation), the partial differential equations presented in this chapter have no general analytical solution, but they can be solved numerically. This technology involves the spatial domain discrete into finite control volumes, and the integration of governing equations into each control volume. Hence the other relevant quantities, like mass, momentum and energy can be preserved in a discrete sense for each control volume. And then the discretized equations are solved iteratively for each control volume. The approximate solutions to each variable can be obtained at central points of the control volume throughout the domain.

To predict the process of evaporation and entropy generation, it is important to model the evolution of the vapour and transport phenomena on a microscopic scale. The interfacial structures that characterize evaporation of liquid are complicated, and normally it is not possible to solve the exact conservation equations on a microscopic scale. Instead, macroscopic models of the transport phenomena are used. These can be derived by averaging the microscopic equations over a finite averaging volume that contains both liquid and vapour. This volume is smaller than the overall system and large

compared to the characteristic size of interfacial structures. This volume-averaged method can be used to handle continuum equations for two-phase flow. This section presents CFD cavitation results of a NACA 4412. Based on these numerical solutions, the two-phase flow entropy production formulation will be investigated and discussed.

5.3.1 Method of CFD (computational fluid dynamics)

As one of two -equation models, k-ε model is robust and has been widely used in numerous fields including industrial applications and scientific research, which solves kinetic energy k and turbulent dissipation ε. Even though it was reported that the model performs poorly for flows with separation which stems from lack of capability to ascertain adverse pressure gradients [112] [113], it is easy to implement in CFD simulations. This model is applied in this research for the CFD simulations of hydrofoil and propeller.

Another challenge in CFD is to properly treat the thin layer near the wall, where viscous effects are dominant because of the non-slip boundary condition. Since the k-ε model is for high Re flows and Re is low close to the airfoil surface a wall function is used to model the near-wall velocity profile.

A typical NACA hydrofoil geometrical construction is illustrated in Fig. 5-1. The leading edge and mid-chord cavitation on a hydrofoil have particular importance for turbine or propeller cavitation studies because they represent two-dimensional section characteristics of blade cavitation. Fluid flow past a 2-D NACA 4412 hydrofoil that has a maximum thickness of 12% and a camber ratio of 4% located 40% back from the airfoil leading edge is initially adopted as a benchmark case for validation purposes. The same

hydrofoil geometry was used for experimental cavitation studies in Ref. [114], carried out in a high speed water tunnel. It includes tests of a 2-D 3" chord and 10" span section of the NACA 4412 hydrofoil, with measurements during cavitation-free operation, hydrodynamic forces and moments as functions of the angle of attack, and the velocity field, as well as observations under cavitating conditions with the inception and growth of cavitation bubbles at different angles of attack as functions of the cavitation number, C_a. Validation was performed by comparing existing data from the NACA database with results obtained from the two-dimensional simulations.

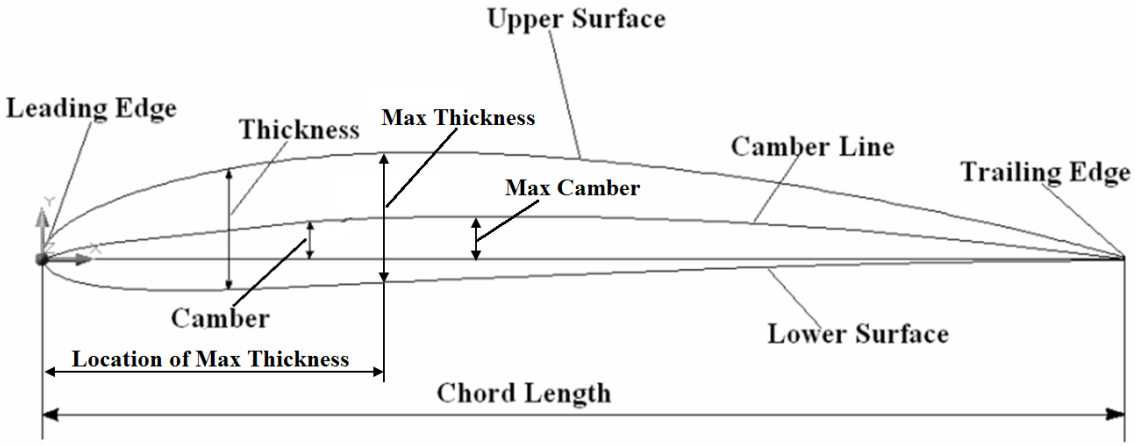

Figure 5-1: NACA hydrofoil geometrical construction

5.3.2 Geometrical modeling and grid generation

A structured grid consisting of 307,688 quadrilateral cells (among others developed afterwards for grid convergence studies) was generated in a computational domain. The domain extended to $-5C \leq x \leq 6C$ horizontally and $-2.5C \leq y \leq 2.5C$ vertically, where *C* represents the chord length, as shown in Fig. 5-2. A simulation of a modified NACA66 foil section was carried out using FLUENT 6.1 with the same domain size [85] and the results had a good agreement with experiment investigations [115]. To

eliminate boundary effects in the top, bottom, and outlet regions, the boundaries were located several span lengths away from the hydrofoil.

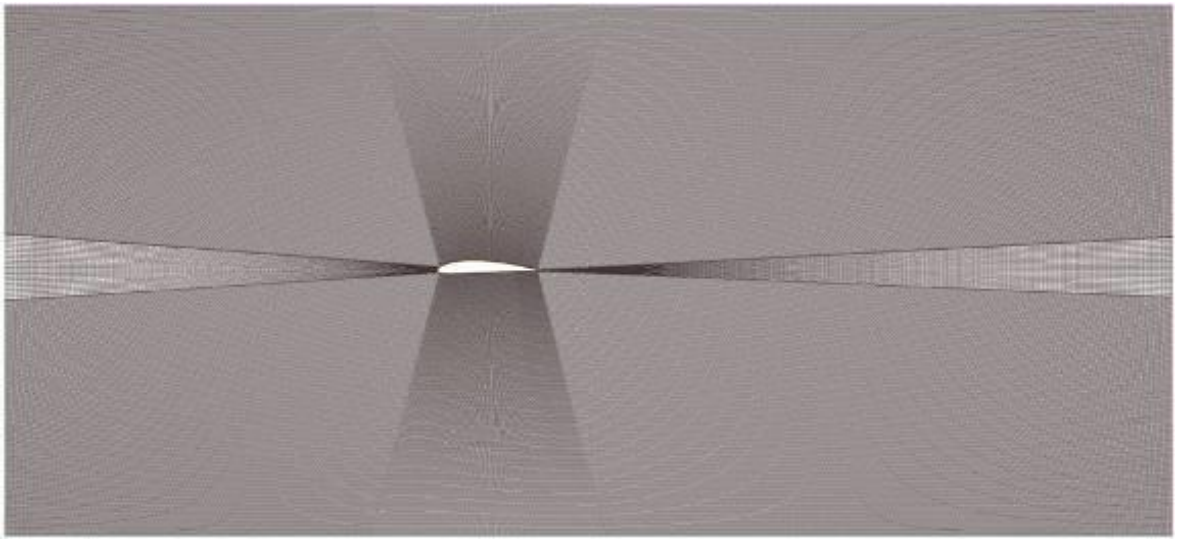

Figure 5-2: Computational domain and hexahedral mesh of NACA 4412 hydrofoil

5.3.3 Boundary conditions

For this case, the inlet boundary condition on the left side facing the leading edge was set to a uniform flow of normal velocity and a medium turbulence intensity of 5%. The estimation of the value of turbulence intensity is based on the upstream history of the flow in the water tunnel. The experiment measurement of this hydrofoil was taken using a loop water supply. The flow could be considered as fully developed therefore the turbulence intensity might be little higher than normal by a few percent. An eddy viscosity ratio, 5 was assumed, which is the ratio between the turbulent viscosity and the dynamic viscosity. By doing so is to estimate the influence of the turbulent viscosity over molecular viscosity at inlet. To compare the simulation results with experimental data, the velocity magnitudes were configured to 3.36, 6.59, 8.55, and 10.58 m/s to fit the Reynolds numbers of 287,000, 563,000, 730,000, and 903,000, respectively. A static

pressure outlet boundary condition was prescribed on the right side, facing the trailing edge (see Figure 5-1). Symmetry boundary conditions were set on the orthogonal section planes of the hydrofoil, under which a 2-D flow around the hydrofoil was simulated. The normal velocities were set to zero, indicating no flow across that boundary. A free boundary slip condition was applied along both the upper side and lower edges of the computational domain, where the shear stress at the boundary was zero ($\tau = 0$), and the velocity of the fluid near the wall was not retarded by wall friction effects. A no-slip boundary condition was prescribed on the hydrofoil surface. The fluid immediately next to the wall assumed the velocity of the wall was zero.

The scalable wall functions [116], in combination with the standard k-ε turbulence closure are employed. The average value of $y^+$was evaluated on the solid surfaces of the hydrofoil which is about 24. $y^+$is the dimensionless distance from the wall defined as $y^+ = \Delta y u_\tau / \nu$, where, $u_\tau = \sqrt{\frac{\tau_w}{\rho}}$ is the friction velocity, Δy is the normal distance from the wall, and τ_w is the wall shear stress. The logarithmic relation for the near wall velocity is given by $u^+ = \frac{U_t}{u_\tau} = \frac{1}{\kappa}\ln(y^+) + C$, where, κ is the Von Karman constant and C is a log-layer constant depending on wall roughness. The velocity U_t tangent to the wall at a distance of Δy from the wall is determined.

5.4 Grid independence study

The simulation of the NACA 4412 hydrofoil was examined in a grid refinement study to confirm grid independence of the predicted results. The number of elements in this baseline grid was 307,688. For the grid dependence study, another grid was generated with the same mesh strategy, but by systematically decreasing the element size

on the edges, resulting in roughly three times the number of elements. The number of cells in the grids was 956,008. Table 5-1 shows slight differences between the two mesh configurations, with errors of 0.7%, 0.2%, and 0.3% for measurements of forces in the X and Y directions and torques about the Z axis, respectively.

Table 5-1: Comparison between two mesh configurations

	Coarse Mesh	Fine Mesh	Error
Nodes	618,192	1,439,280	
Elements	307,688	956,008	
Force (X) [N]	-0.0324465	-0.0322098	0.7%
Force (Y) [N]	-1.85574	-1.85979	0.2%
Torque (Z) [N m]	0.0503247	0.0504576	0.3%
Convergence criteria	1E-6	1E-6	
Master computer on mesh partition	1.600E+03 s	3.861E+03s	
Slave computer on mesh partition	1.474E+03 s	3.866E+03 s	
Total wall clock time	3.566E+03 s	7.282E+03 s	
Computer configuration	AMD Dual Core 2.40 GHz, 3.0 GB of RAM, Win XP		

5.5 Results of CFD validation

5.5.1 Forces on NACA 4412 hydrofoil

A simulation was performed to compare against past measured data during cavitation-free operation. Hydrodynamic forces and moments were found as functions of

the angle of attack and Reynolds number. The results are compared with existing data of the hydrofoil from water tunnel tests. The test data and the numerical results of section lift coefficient, profile drag coefficient, and center of pressure in percent of the hydrofoil chord are shown in Figs. 5-3 to 5-5. Four tests were conducted over a Reynolds number range from 287,000 to 903,000.

Because the excessive magnitude of the forces developed, the test data were not taken up to the maximum lift for all Reynolds numbers with the measurements. The data gathered only for the two lower Reynolds numbers has been obtained. Data obtained with the numerical simulation were complete over all Reynolds number range and allow predictions of cavitation events to be taken at all operating conditions of interest.

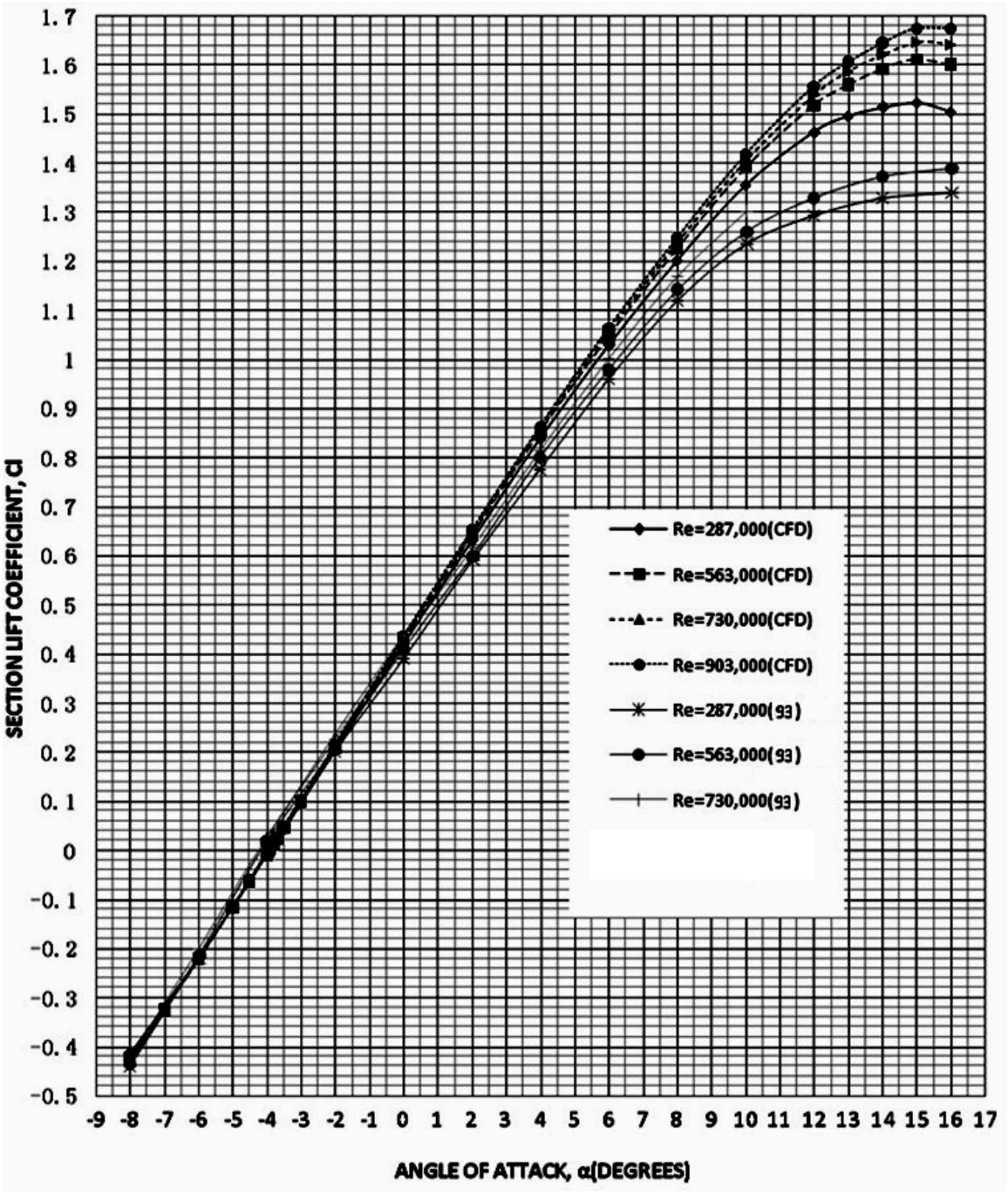

Figure 5-3: Predicted and measured data of section lift coefficients

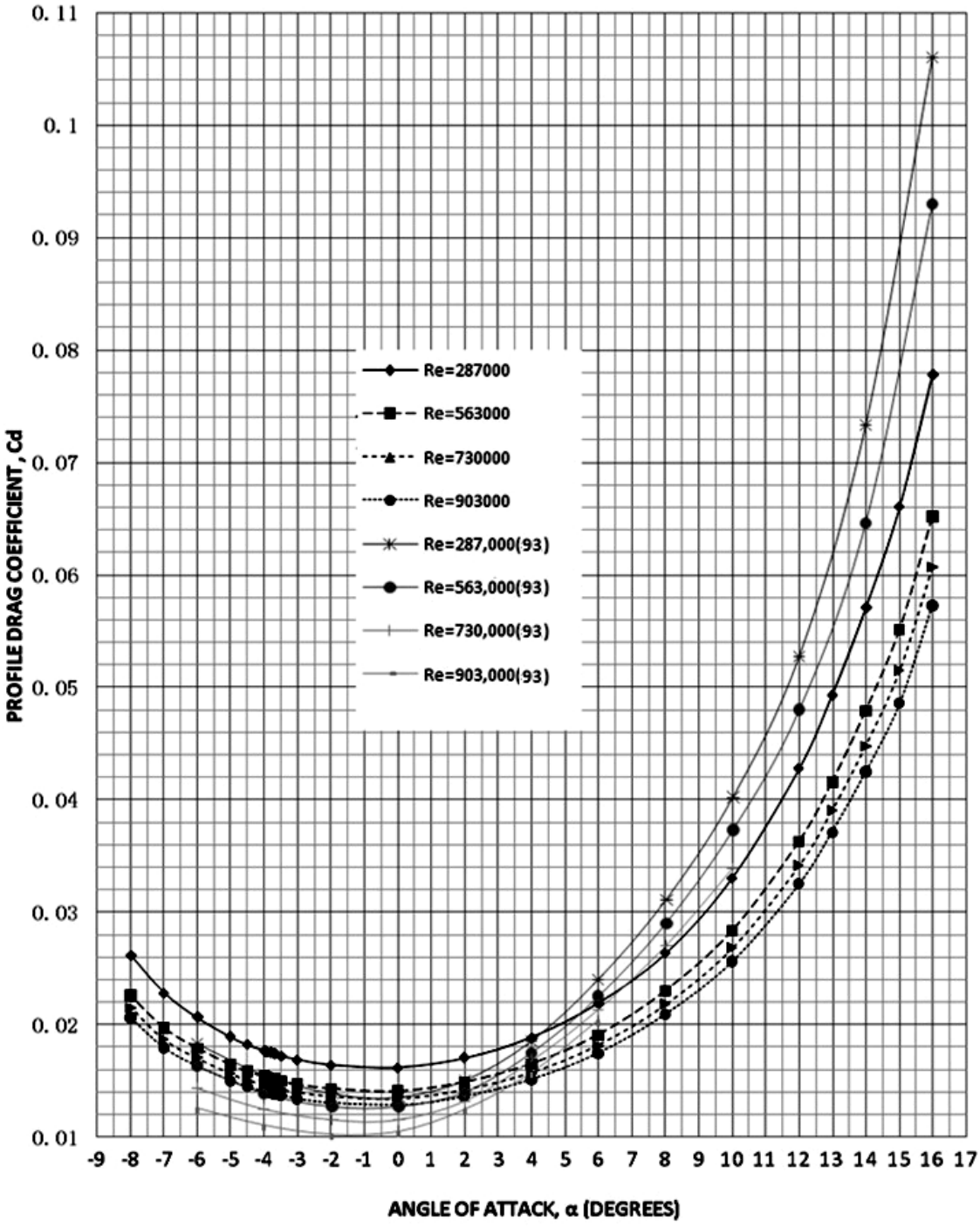

Figure 5-4: Predicted and measured data of profile drag coefficients

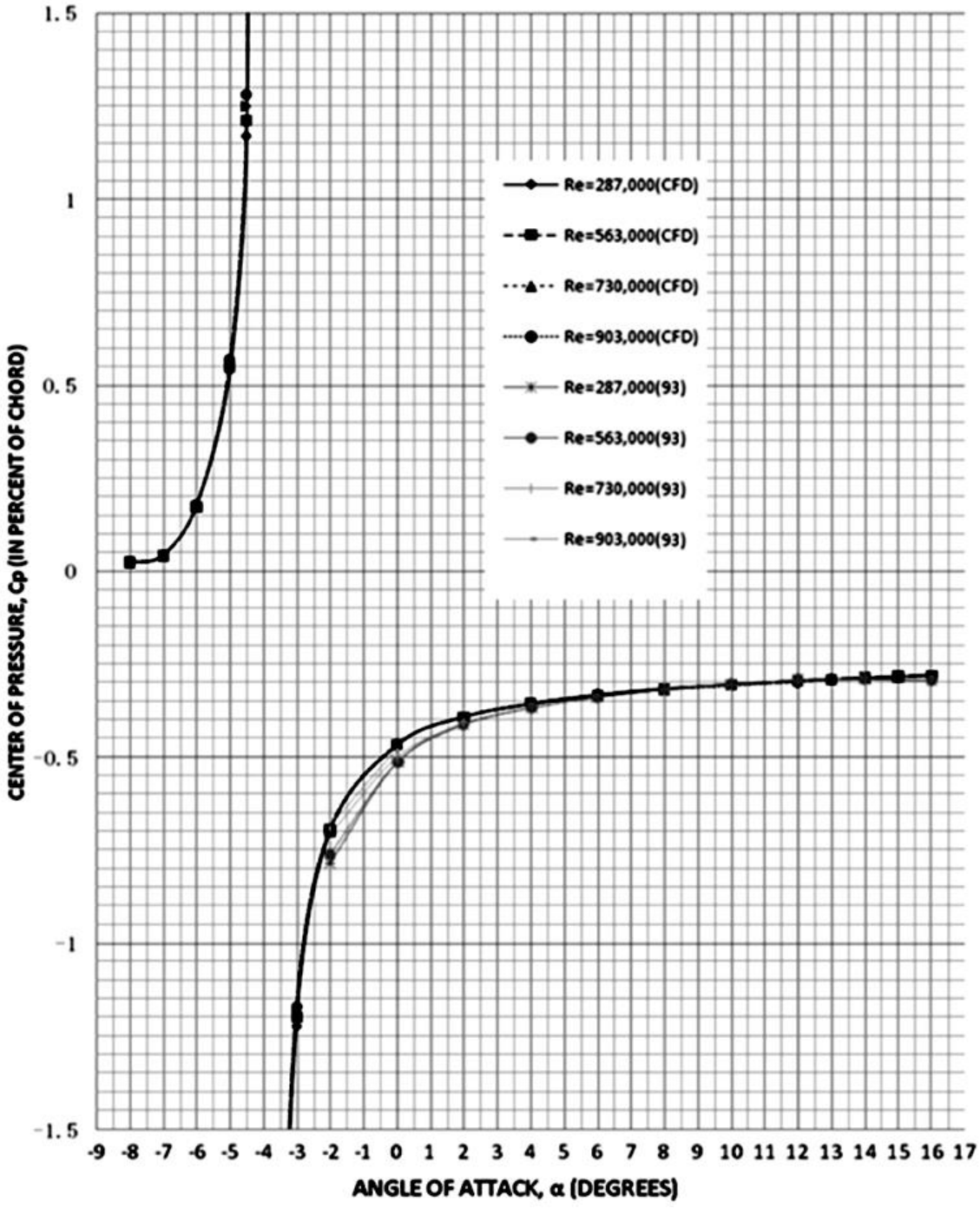

Figure 5-5: Predicted and measured data of center of pressure

We can see from Figs. 5-3 to 5-5 that both numerical results and test results show

certain consistent change in performance. The slope of the lift curve becomes steeper and the maximum lift coefficient turn out to be larger with the increase in Reynolds number. The values of lift coefficients in Figs. 5-3 have good agreements with the experimental data for small angles of attack $(-8° \leq \alpha_0 \leq +8°)$. The maximum lift coefficients obtained from the water tunnel test for Reynolds number 287,000 and 563,000 are about 1.36 and 1.39 at 16° of angle of attack, whereas the numerical results of the same items show about 1.52 and 1.61 at 15° of angle of attack, respectively. The computational and experimental results for the profile drag coefficient as function of angles of attack are illustrated in Fig. 5-4. The curves show consistent variation with Reynolds numbers. The minimum drag force occurs at 0° of angle of attack which agrees with the experimental data, but the values are a little bit larger than those obtained by experiment measurement. This good agreement with the results of the two dimensional model is expected due to the quasi two-dimensional character of the water tunnel test installation.

The measured hydrodynamic forces and moments approximate but differ from the characteristics of a hydrofoil section with infinite aspect ratio. The occurrence of the finite span of induced effect reduces the lift force and increases the drag force [114]. It should be recognized that the infinite aspect ratio only exists in an ideal test circumstance and this real two-dimensional experiments are extremely difficult to achieve, particularly at higher angles of attack. Therefore, the experimental data are only available for validation. CFD predictions of this quantity are of interest because it can create the real two-dimensional numerical simulations by applying the symmetric boundary conditions, which eliminate the influence of the induced effect and truly represent the basic behavior of the foils profiles shape independent of aspect ratio or other geometrical arrangement.

The main differences of performance between infinite aspect ratio of hydrofoil and those obtained by tests of a finite span hydrofoil occur in the region of large angles of attack. The effect is significant for large angles of attack. Fig. 5-5 shows measurements of center of pressure and pitching moment coefficients in percent of the hydrofoil chord as functions of the angle of attack at different Reynolds number. The same contents for the numerical results are also illustrated. The numerical results show good agreement with the measurements for the angles of attack between -2° and 16°. The curves overlap each other, which mean the C_p values are only the functions of angles of attack independent of Reynolds number.

The values of center of pressure with angles of attack between -8° and -2° were not given in the measurements, because there is an enormous value of C_p around the area of zero lift coefficients. A hydrofoil does not generate lift when the lift coefficient is close to zero. At this position a conventionally cambered hydrofoil produces a nose-down pitching moment, which results in an infinite distance of the pressure center behind the hydrofoil [114]. This tendency is also illustrated in numerical simulations. The figure shows how the C_p changes with angle of attack for the typical cambered NACA 4412 hydrofoil. Note that the C_p location moves off the hydrofoil and tends to infinity as C_l approaches zero, and that the direction of movement of the center of pressure has a reversion on the zero lift point.

Fixing the moment reference point is a simple and preferable approach, since the pitching moment shows little or no dependence on the angle of attack. The point is called hydrodynamic center. On the cambered hydrofoil NACA 4412 the hydrodynamic center is not in a fixed location and lies a little behind the quarter-chord point. At the

bottom of Fig. 5-5, the pitching moment coefficients referred to the hydrodynamic center are illustrated for the experimental and numerical results respectively. The pitching moment about the point in the hydro foil is essentially independent of angle of attack for a wide range. In these two figures, the moment coefficients is nearly constant up to about 5°, and within 15% of a constant value up to about 8°. Furthermore all runs show nearly the same magnitude for pitching moment coefficient, $C_{m_{a,c}}$.

In short, the predicted flow patterns show good agreement with the experimental data. The predicted data were obtained directly by solving the RANS equations with no corrections. In the water tunnel tests, a quasi-infinite span was assumed to simulate infinite aspect ratio characteristics.

5.5.2 Cavitation on NACA 4412 hydrofoil

Observations of the inception and growth of cavitation were carried out in the water tunnel by means of photographs. They were recorded at different angles of attack, as functions of the cavitation parameter C_a. The measurements include the onset of cavitation on one or both faces of the NACA 4412 hydrofoil, at attack angles ranging from -4° to +12°. Figure 5-6 shows a diagram with inception of cavitation on the upper and lower surfaces of the hydrofoil, for different cavitation parameters, against the angle of attack. The computational results show close agreement with the water tunnel measurements.

The photos taken of the measurements and images of contours of vapour volume fraction of 1% from CFX-Post are shown together side by side in Figure 5-7. Each group is arranged to show the development of cavitation as the pressure and cavitation

parameter, C_a, are reduced. Both water tunnel measurements and computational results show cavitation begins earlier for larger angles of attack, meaning at higher pressures or lower velocities, and hence higher critical values of C_a. Figure 5-7 shows cavitation inception and development for $\alpha_0 = +12°$ .The left column shows photos on the upper surface for the measurements. The right column shows the section views for contours of vapor volume fraction of 1% from the computational results. The first row shows the beginning of cavitation near the leading edge of the upper side, and the typical leading edge sheet cavitation soon after inception at $C_a = 1.17$. For $\alpha_0 = +12°$, no cavitation is obtained on the lower surface, even though C_a is reduced to 0.3, while cavitation is well established on the upper surface at $C_a = 2.94$ and $\alpha_0 = +12°$. At higher angles of attack, cavitation occurs only on one surface of the hydrofoil. There is a sufficient dynamic pressure increase on the surface pitched into the flow stream to suppress cavitation completely.

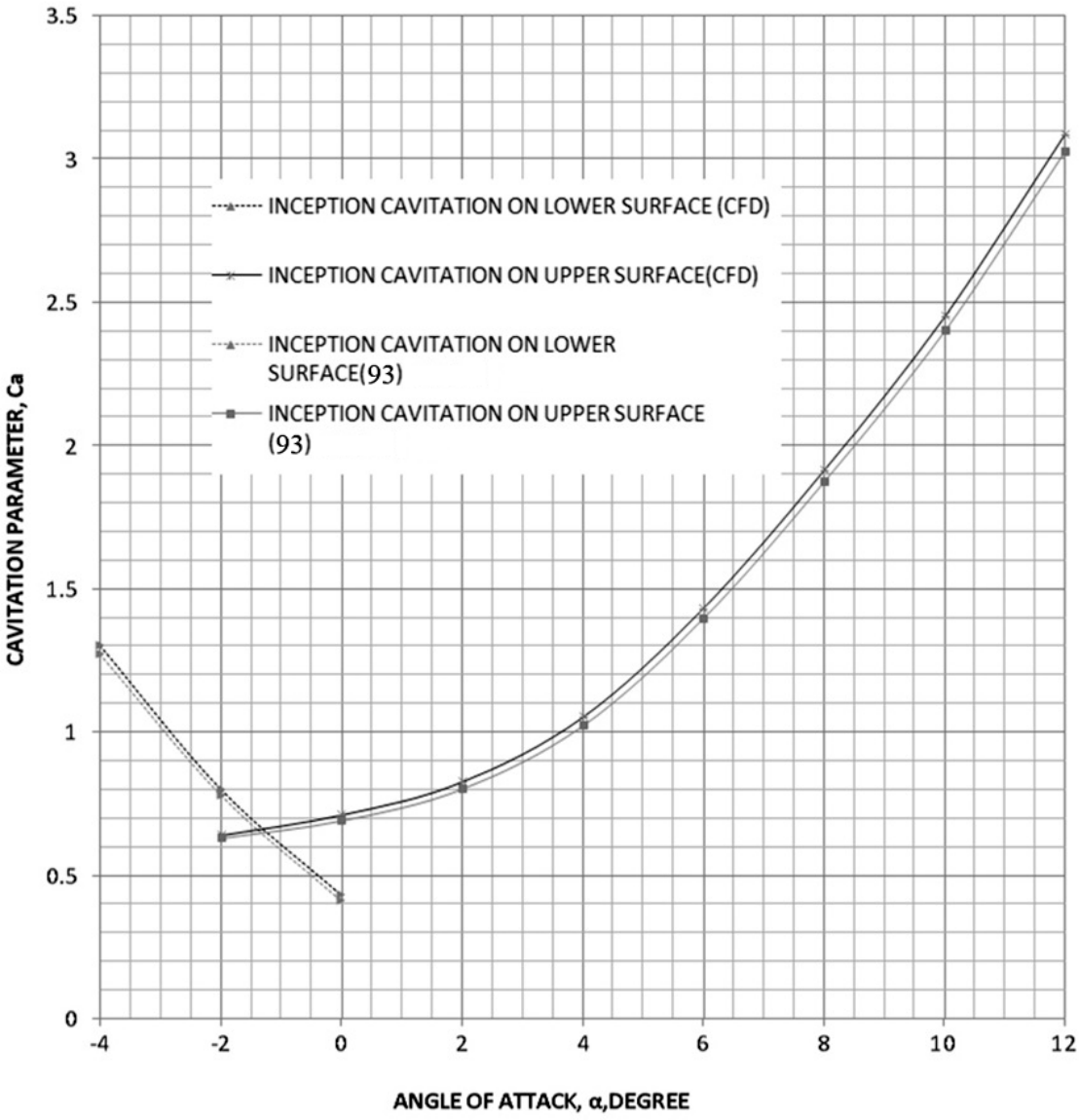

Figure 5-6: Inception of cavitation on NACA 4412 hydrofoil in a water tunnel and predicted results

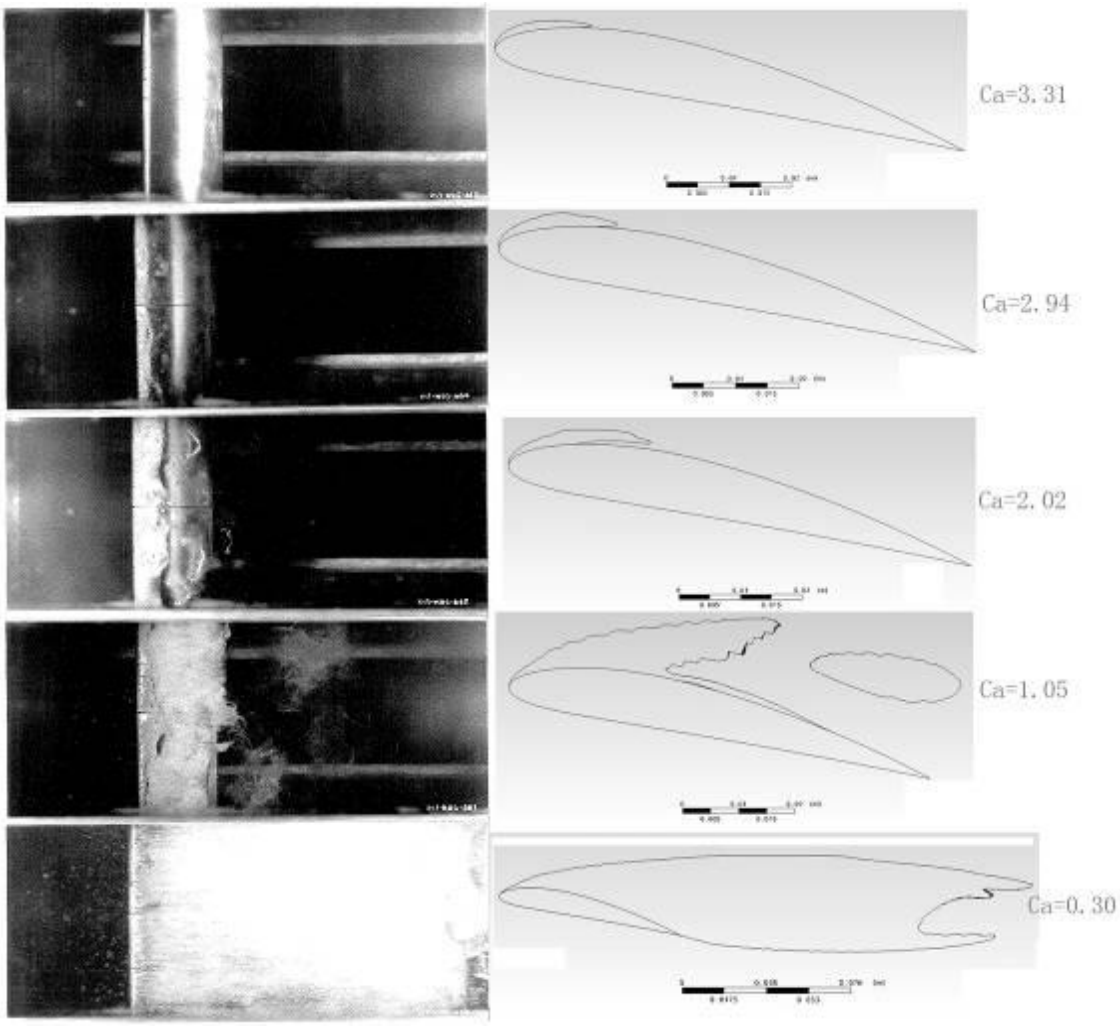

Figure 5-7: Cavitation on NACA 4412 hydrofoil; Upper surface at $\alpha_0 = +12^{\circ}$
Left side: top view of Robert et al. [114], Right side: side view of CFD results

5.6 Entropy production with NACA 4412 hydrofoil

Local entropy production due to the NACA 4412 hydrofoil is examined at four Re numbers and five angles of attack. First, the mixture viscous dissipation, mixture turbulent work, diffusion stress , and interface energy source and surface tension effects that contribute to the entropy production rate as defined by Eq. (5.36) are investigated separately for the case of Re = 903,000 at an attack angle of 8 degrees. Second, local

production rate variation is investigated normal to the hydrofoil at a Re number of 93,000 and along the surface of the hydrofoil at Re = 287 000, 560 000, 730 000 and 930 000, and at α_0 = 0, 4, 12, and -4 degrees. Results are presented along lines normal to the upper surface of the NACA 4412 hydrofoil at eight points as defined in Figs. 5-8 – 5-12.

In these figures y is defined normal to the foil surface. The local boundary thickness, δ is defined as a distance across a boundary layer and has essentially reached 99% of the free stream velocity, U_∞.

The slopes of the lines are determined using the derivative of the NACA 4412 curve so that the lines are strictly perpendicular to the NACA curve. In Figs. 5-8 – 5-12, y is the coordinate in the normal direction normalized by δ, the local boundary thickness of the NACA4412 profile at the given points 1-8. Figure 5-8 predicts that entropy production that arises from dissipation due to the mixture mean flow motion $\mathbf{u}_m$. The logarithmic representation of the mean viscous dissipation Φ_m^μ is illustrated. This dissipation is comparable to the viscous dissipation of the mean velocity field in a single-phase turbulent flow case. For such single-phase viscous flow, both laminar and turbulent, the viscous dissipation is a function of velocity gradient because the dynamic viscosities are constant at a certain temperature.

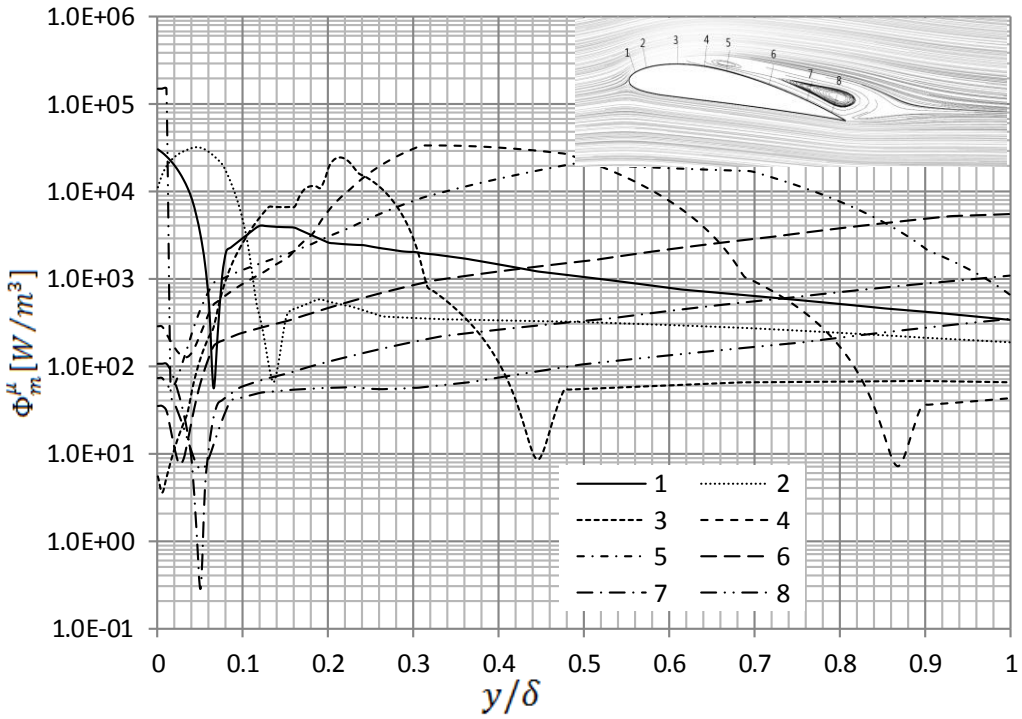

Figure 5-8: Mean viscous dissipation on lines 1-8 (Re = 903,000 at $\alpha_0 = +8^{\circ}$)

For a two-phase flow, the value of the mixture dynamic viscosity μ_m is determined by the void volume of the vapor and the dynamic viscosities of the two substances - liquid and vapor. In the same way, the mean velocity is determined not only by the individual velocities of the two-phase substances but also by the void volume of the vapor. Near the vicinity of the wall, the gradient of mean velocity has a maximum value. However, the mixture dynamic viscosity varies from location to location. In the liquid dominant area where less cavitation occurs, the mean mixture dissipation is dominated by the mixture velocity gradient. The curve of the mean viscous dissipation Φ_m^{μ} along line 1 shows the value near the surface has a maximum value followed by a drastic decrease. In this area, the cavitation occurs, causing the void fraction to grow. The mixture dynamic viscosity in this region has a relatively small effect on the shear stress.

Out of this region, the cavitation gradually eases; hence, the liquid phase dominates the region again. Meanwhile, the gradient of mixture velocity does not change significantly, so the mixture dynamic viscosity greatly increases, causing an increase in mean viscous dissipation. Afterwards, the irreversibility gradually increases because the velocity gradient of the mixture progressively decreases with the flow field away from the boundary.

Figure 5-9 shows the irreversibility due to the Reynolds shear stress $-\rho\overline{\mathbf{u}'_m\mathbf{u}'_m}$ resulting from the mixture velocity fluctuation. The logarithmic representation of the turbulent dissipation Φ_m^T is illustrated. This irreversibility can also be interpreted as the work done by the force $-\nabla(\overline{\mathbf{u}'_m\mathbf{u}'_m})$ in the streamwise direction and dissipated to thermal energy. It is comparable to the turbulent dissipation in a single-phase turbulent flow case. The dissipation rate decreases to a minimum value near the surface. Beyond the minimum, the curves gradually increase.

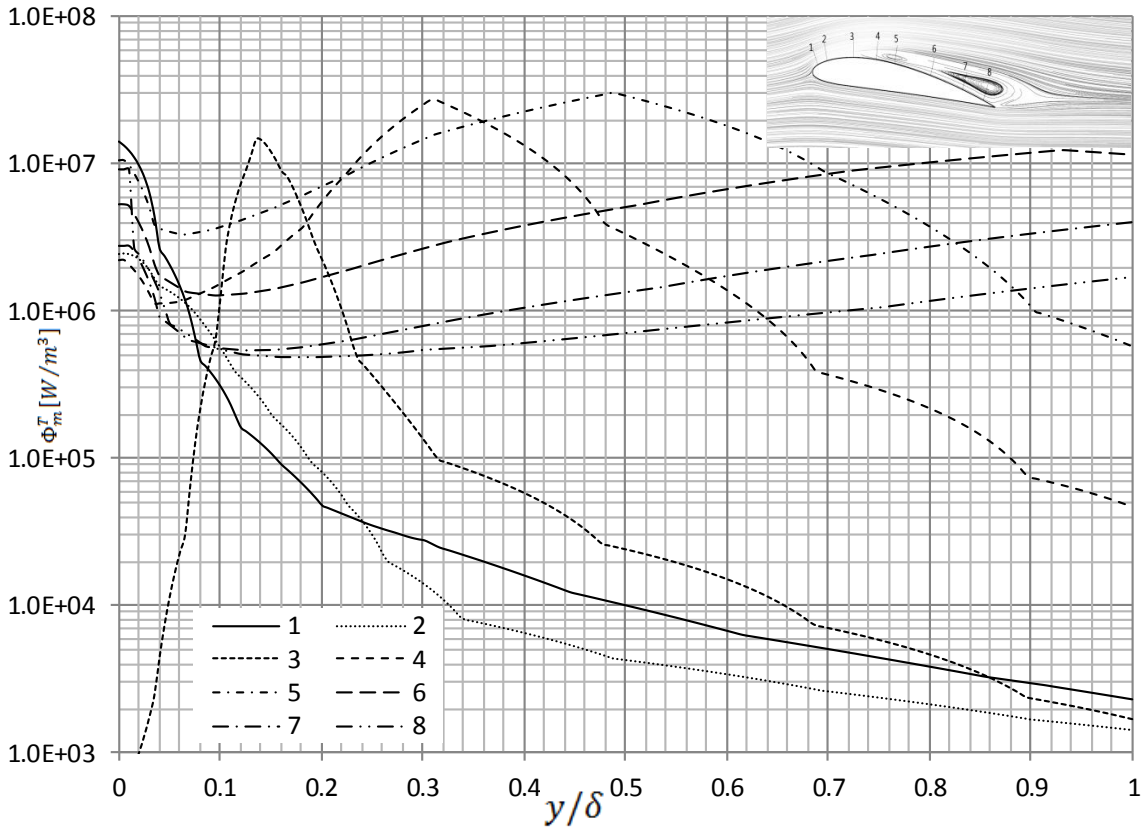

Figure 5-9: Turbulence dissipation on lines 1-8 (Re = 903,000 at $\alpha_0 = +8^{\circ}$)

Figure 5-10 shows the irreversibility due to the slip velocity between liquid and vapor phases. The diffusion velocity of each phase is the relative velocity with respect to the mass center of the mixture. This irreversibility exists in the two-phase flow, but the mechanism of the physics is unclear. Figure 5-10 shows the irregular changes of the irreversibility along these lines.

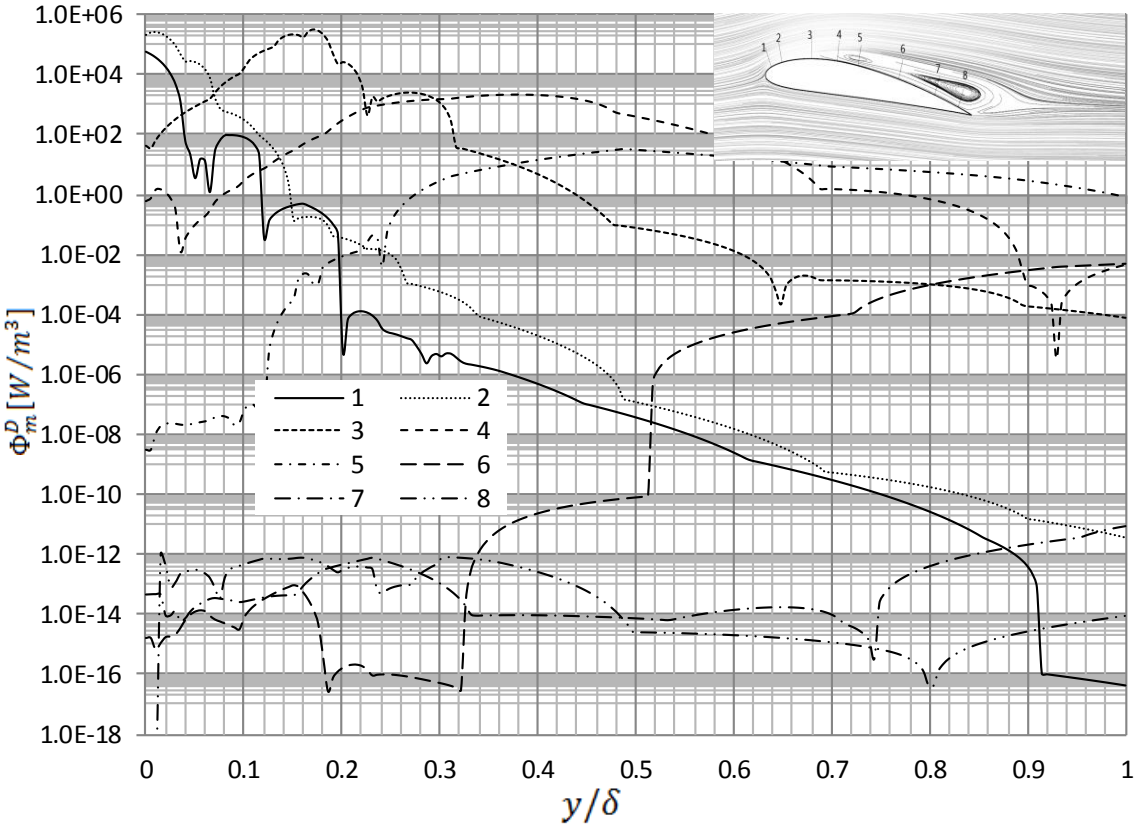

Figure 5-10: Diffusion dissipation on lines 1-8 (Re = 903,000 at $\alpha_0 = +8^{\circ}$)

In CFD, to simplify the solutions of the transport process, the homogeneous multiphase flow model can have a common flow field shared by all fluids, as well as other relevant fields such as temperature and turbulence. In this case, the flow field is homogeneous, assuming the transported quantities (with the exception of volume fraction) are the same for all phases. Hence, for a given transport process, the diffusion irreversibility does not exist because the velocities of liquid and vapor phase are identical. The homogeneous model neglects the diffusion term, causing underestimation of the energy dissipation due to the difference of velocities between the two phases.

Figure 5-11 shows the irreversibility due to the effects of the energy source and the momentum sources from interfaces. In cavitation flow, the large-energy exchanges

involve the latent heat of phase change. This process converts the kinetic energy into internal energy to compensate for the latent heat.

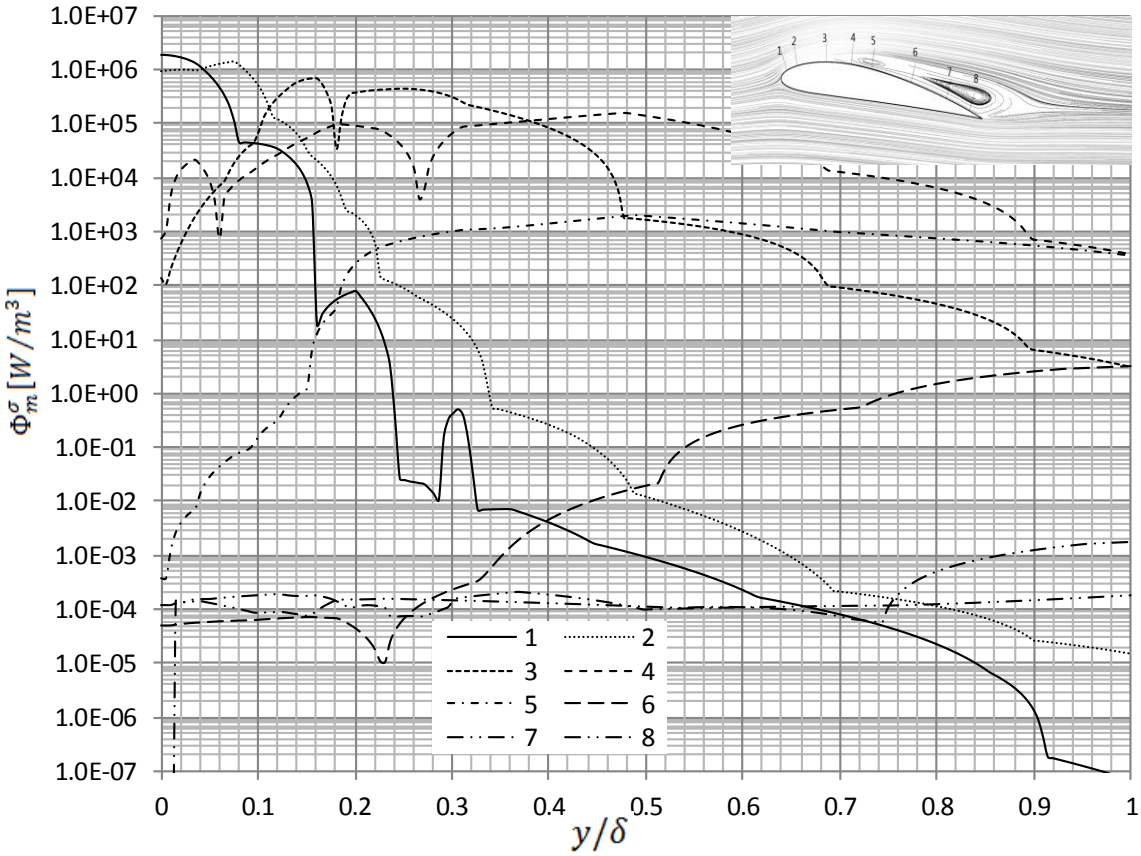

Figure 5-11: Cavitation dissipation on lines 1-8 (Re = 903,000 at $\alpha_0 = +8^\circ$)

The energy dissipation due to the cavitation near the wall has significant effect when the cavitation occurs. On the front upper surface, the energy dissipation rates have relatively high values, and then drop off quickly away from the wall. This variation is evident along line 1. Although this irreversibility occurs only in the regions where the cavitation occurs, the local energy loss has a higher level than the mean viscous dissipation.

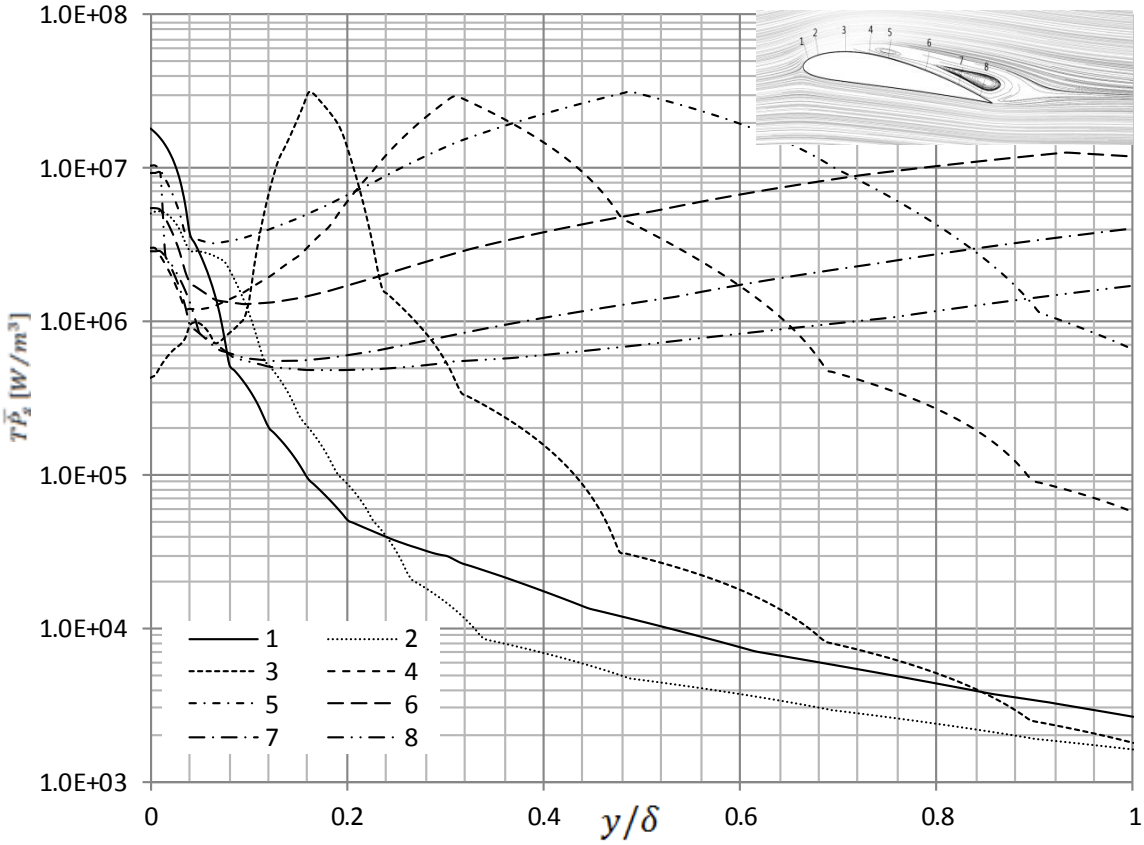

Figure 5-12: Entropy production on lines 1-8 (Re = 903,000 at $\alpha_0 = +8^{\circ}$)

The total entropy production is obtained by adding all elements from Fig. 5-8 to 5-11. The variations of the values depend on many factors. Verification and validation of the entropy model can be made based on the energy balance method. Fig. 5-12 shows the total entropy production along the eight lines in different locations on the upper surface. Figure 5-13 shows entropy production for different Reynolds numbers. In Fig. 5-13, the horizontal coordinate x is normalized by the chord length, C_L of the NACA4412 profile. It is observed that for larger Reynolds numbers, there is a higher energy loss. In addition, the fluctuation occurs at the region where the flow separates.

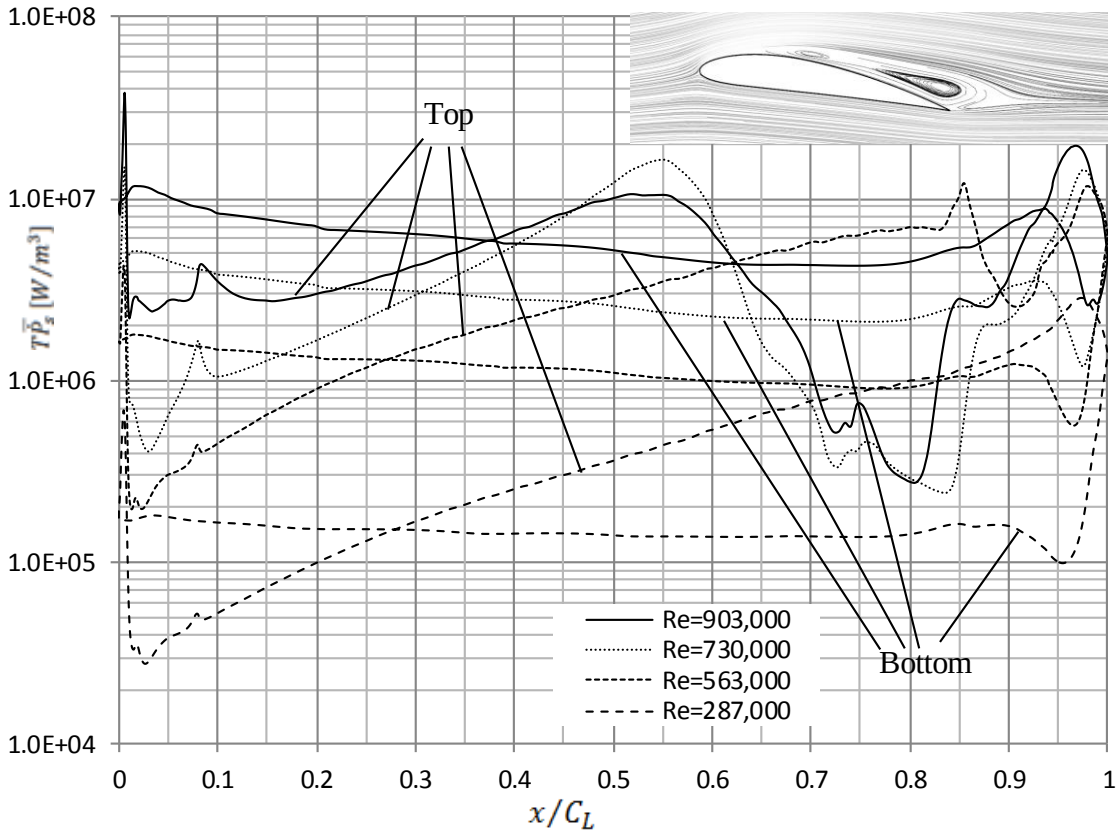

Figure 5-13: Entropy production on NACA 4412 hydrofoil ($\alpha_0 = +8^{\circ}$)

Figure 5-14 shows total entropy production along the lines at $\alpha_0 = 0^{\circ}$ angle of attack. The cavitation at this position is very weak, and the flow has no observed separation. The only energy loss in this situation occurs due to the mean and turbulent viscous components. The irreversibility on the wall has a maximum value, and then gradually drops as it moves away from the wall.

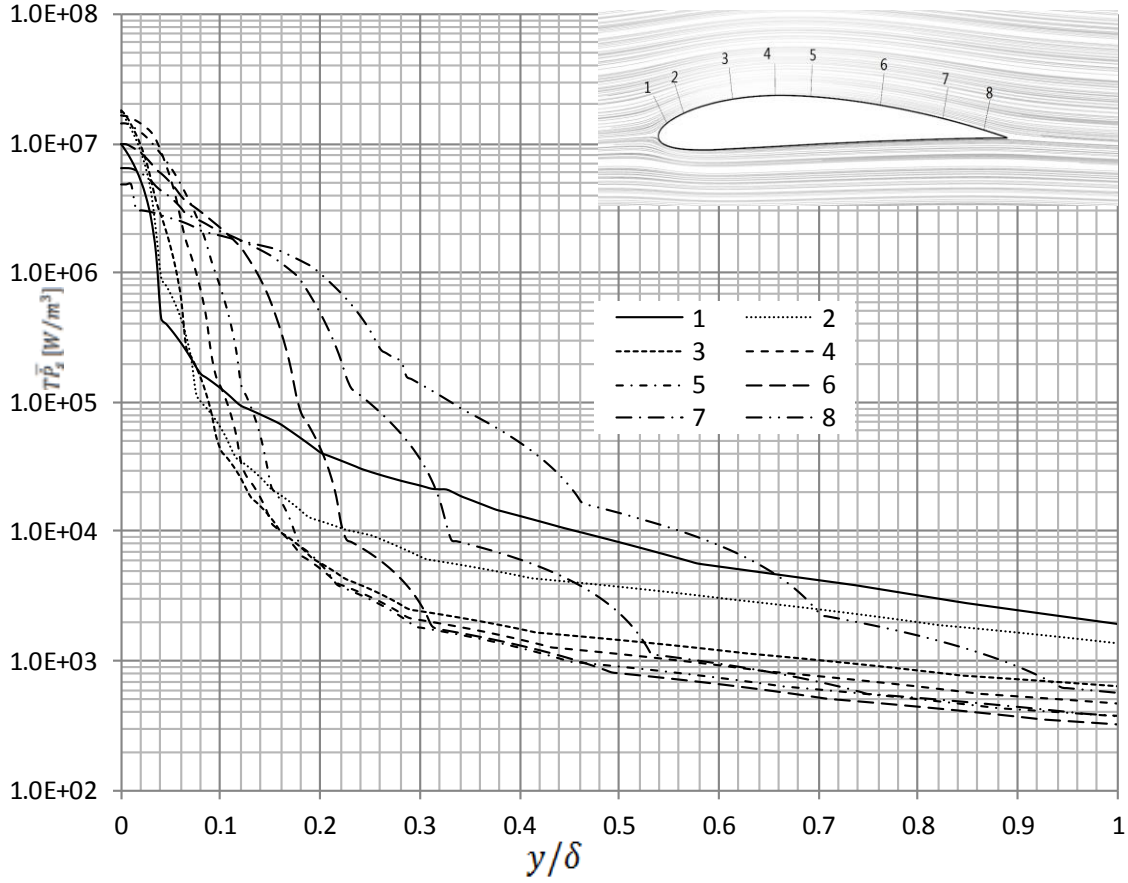

Figure 5-14: Entropy production on lines 1-8 (Re = 903,000, at $\alpha_0 = 0^\circ$)

Figure 5-15 shows entropy production on the surface for different Reynolds numbers. It is observed that the energy dissipation increases with the Reynolds number.

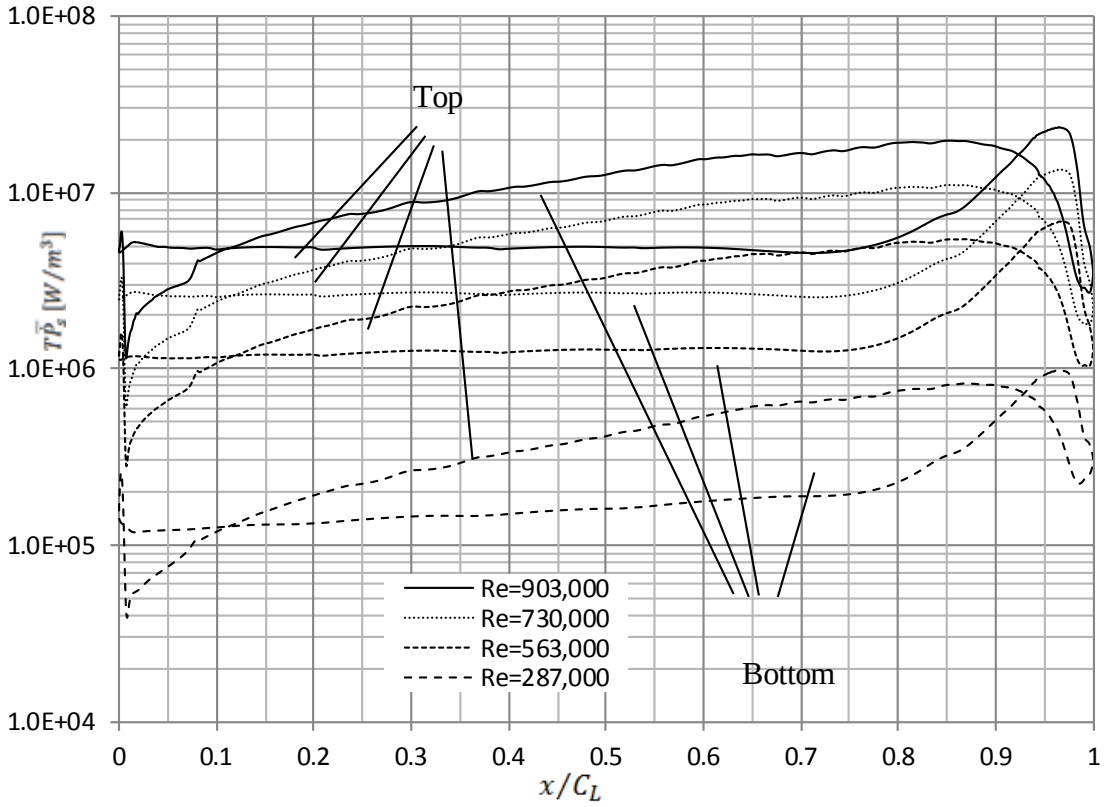

Figure 5-15: Entropy production on NACA 4412 hydrofoil (at $\alpha_0 = 0^\circ$)

Figure 5-16 shows total entropy production along the lines at $\alpha_0 = 4^\circ$ angle of attack. The cavitation at this position is increasingly established. The energy loss at this position gradually increases because of the mean and turbulent viscous components and cavitation. The irreversibility along the lines on the wall has a maximum value, then gradually drops as it moves away from the wall.

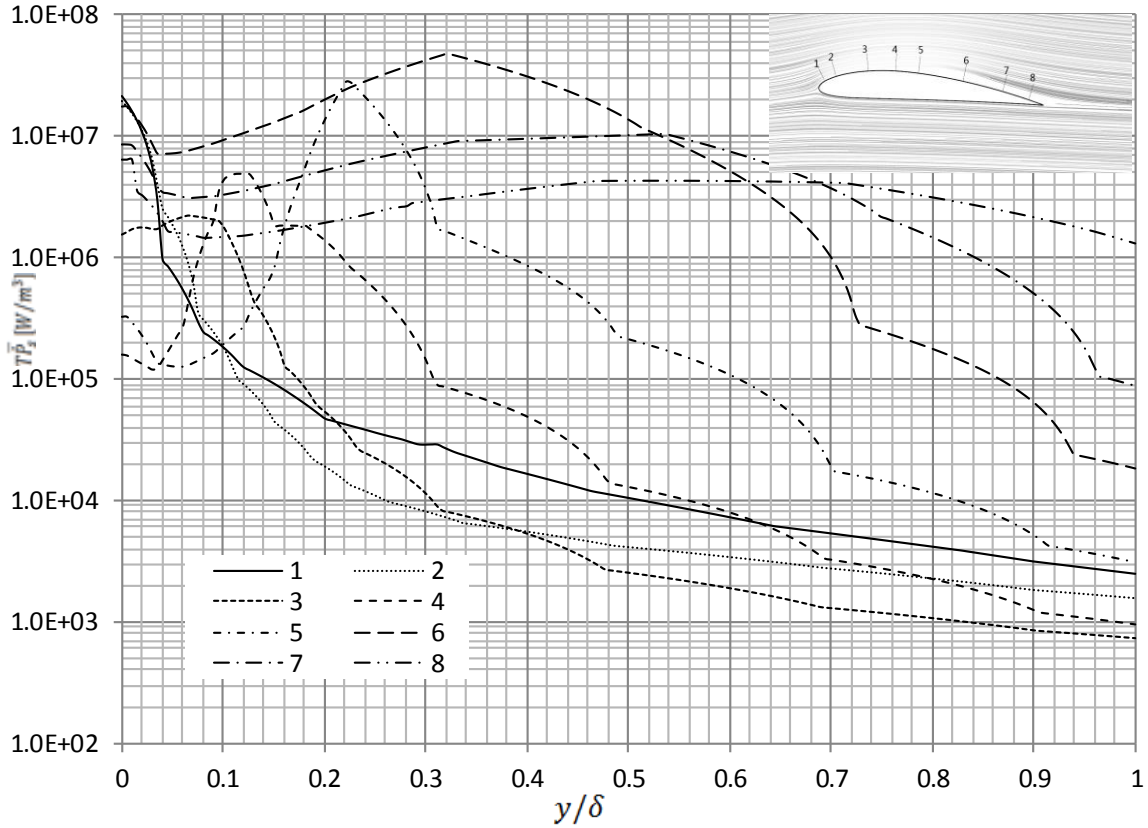

Figure 5-16: Entropy production on lines 1-8 (Re = 903,000, $\alpha_0 = +4^{\circ}$)

Figure 5-17 shows entropy production for different Reynolds numbers. It is observed that the entropy production on the upper surface drops as the Reynolds number is 903,000. Because the void portion of the region increases the mixture dynamic viscosity, the loss in the viscous shear stress has smaller values. The void portion results from the cavitation from the high local velocity across the surface.

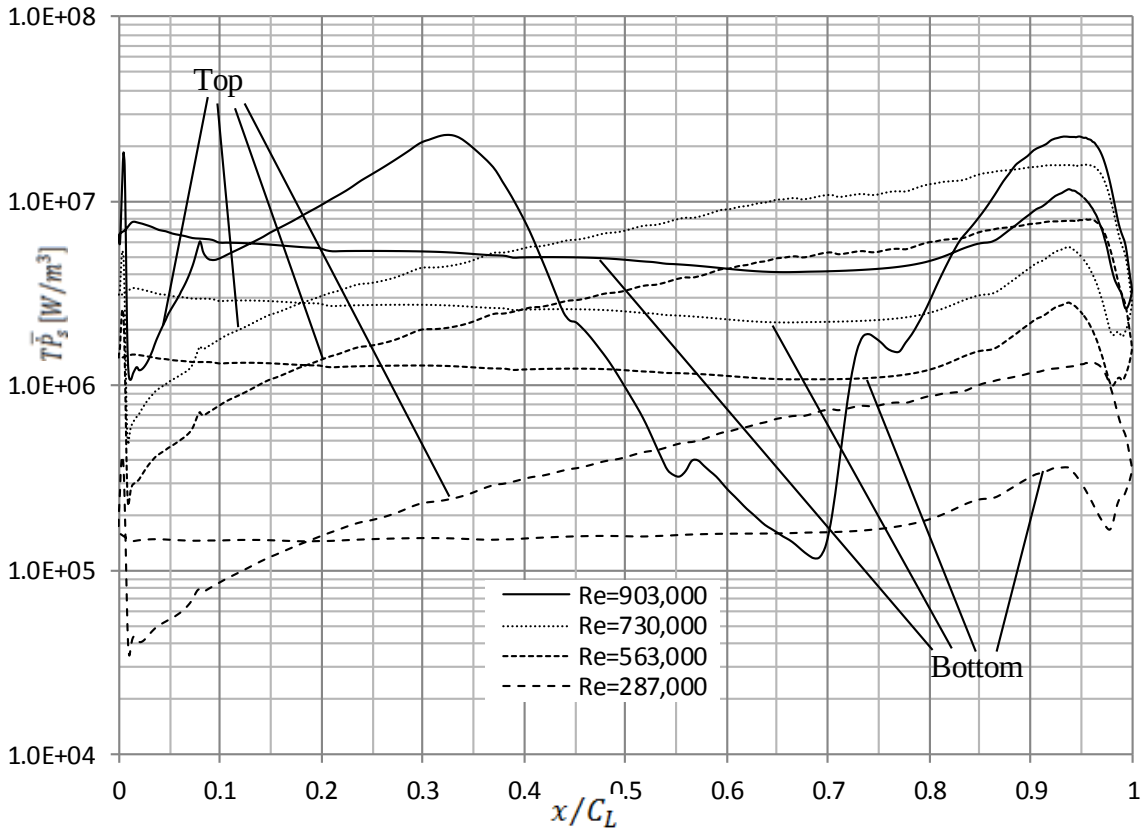

Figure 5-17: Entropy production on NACA 4412 hydrofoil (at $\alpha_0 = +4^{\circ}$)

Figure 5-18 shows the irreversibility on lines 1–8. It is observed that on lines 1 and 2, cavitation does not occur. The energy dissipation largely occurs from the viscous shear stress and turbulent kinetic energy dissipation. The tendency of the two curves illustrates the similarities to the single-phase turbulent flow, discussed in Chapter 4. Downstream, the flow on the top of the surface gradually separates, and the cavitation is increasingly established. The energy loss along lines 3–8 shows the effect of cavitation. The curves drop near the wall, and then gradually increase from the effects of energy and momentum sources from the interfaces.

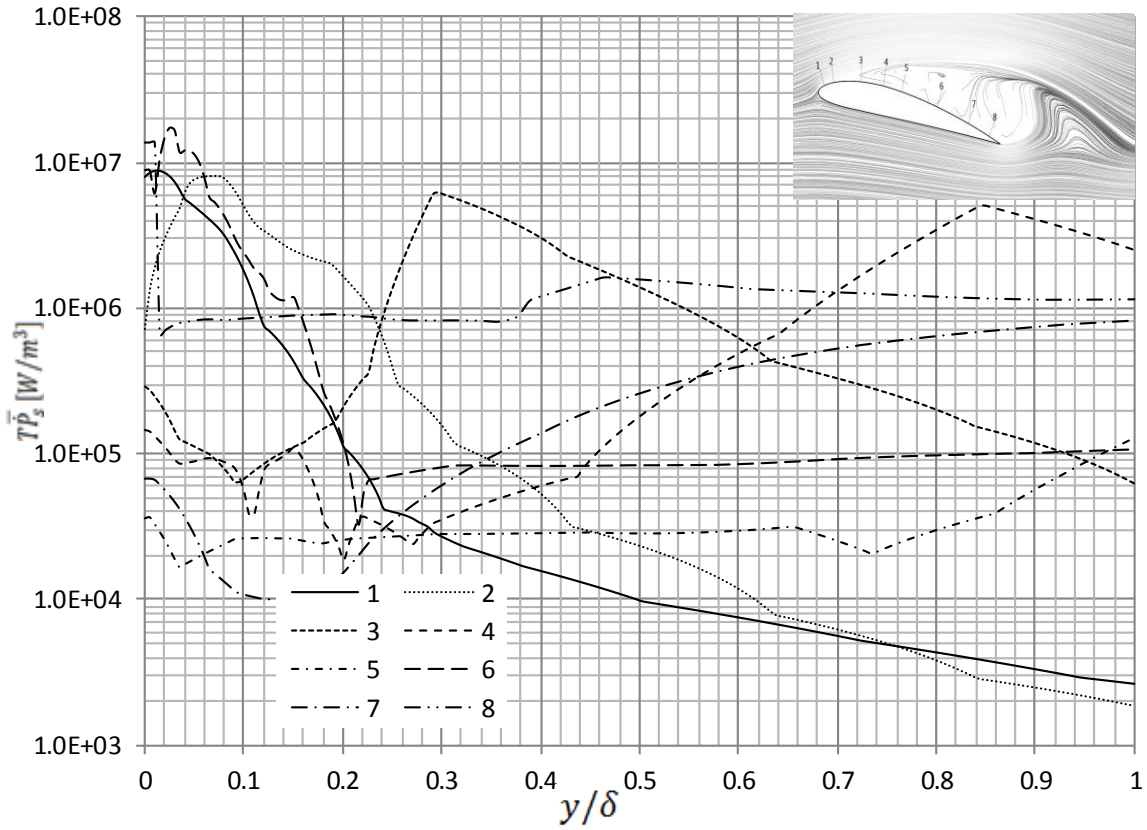

Figure 5-18: Entropy production on lines 1-8 (Re = 903,000, $\alpha_0 = +12^\circ$)

Figure 5-19 shows entropy production on the surface at $\alpha_0 = +12^\circ$ angle of attack for different Reynolds numbers. The entropy production on the upper surface of the profile at a Reynolds number of 903,000 has a fluctuation because the void portion of the region makes the irreversibility uncertain. The void portion results from the cavitation due to the high local velocity passing around the surface.

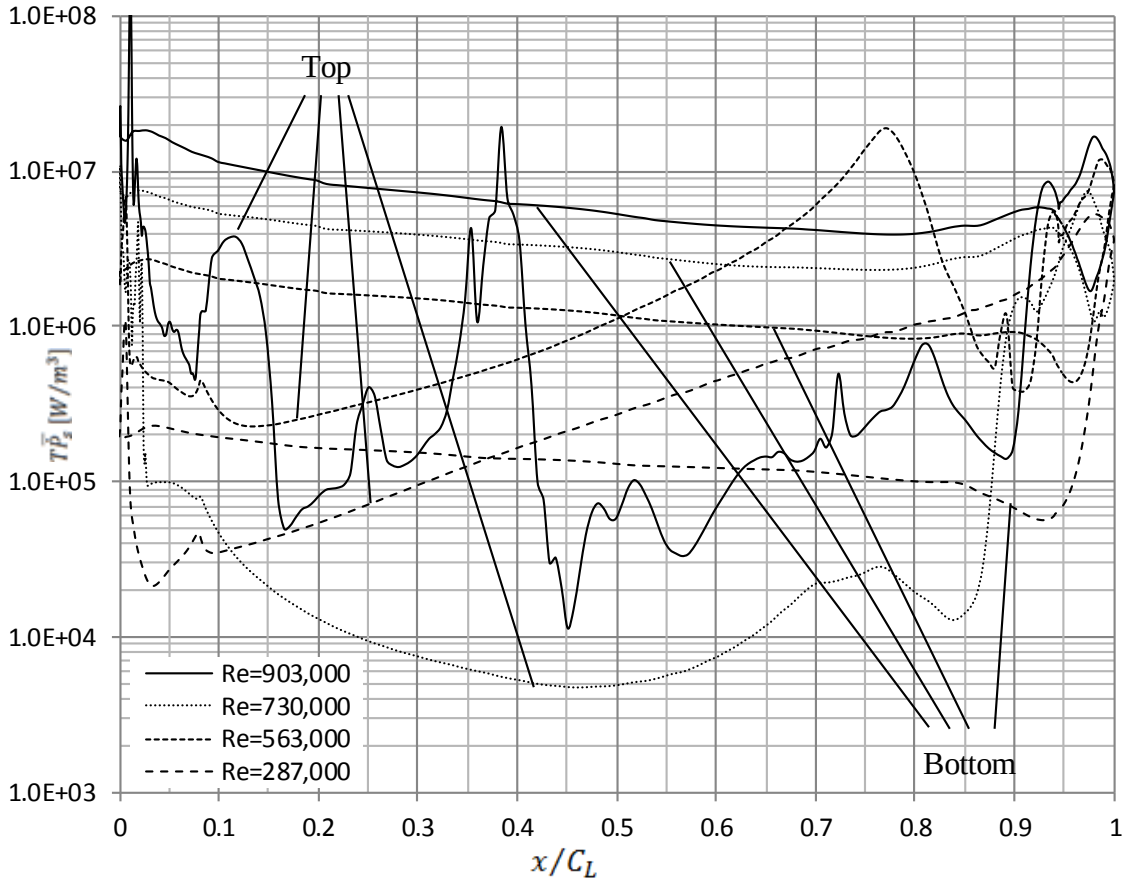

Figure 5-19: Entropy production on NACA 4412 hydrofoil (at $\alpha_0 = +12^{\circ}$)

Figure 5-20 shows the total entropy production along the lines at $\alpha_0 = -4^{\circ}$ angle of attack. The cavitation at this position of the surface is very weak, and the flow has no observed separation. The only energy loss in this situation occurs due to the mean and turbulent viscous components. The irreversibility on the wall has a maximum value, and then gradually drops as it moves away from the wall.

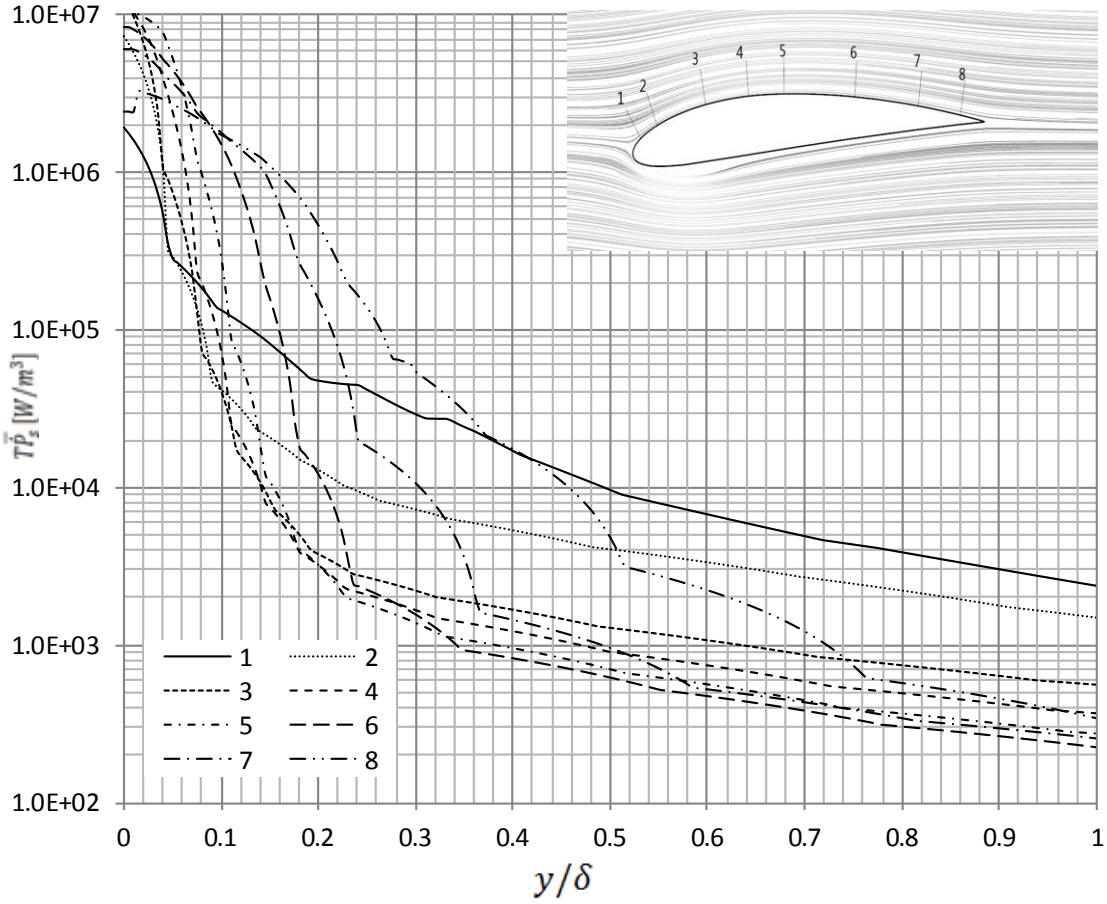

Figure 5-20: Entropy production on line1-8 (Re=903,000 at $\alpha_0 = -4^{\circ}$)

Figure 5-21 shows the entropy production for different Reynolds numbers. It is observed that the entropy production on the bottom surface rises for all Reynolds numbers because the void portion in the region makes the mixture dynamic viscosity fluctuate; hence, the irreversibility fluctuates. The void occurs from the cavitation because of the high local velocity passing around the surface.

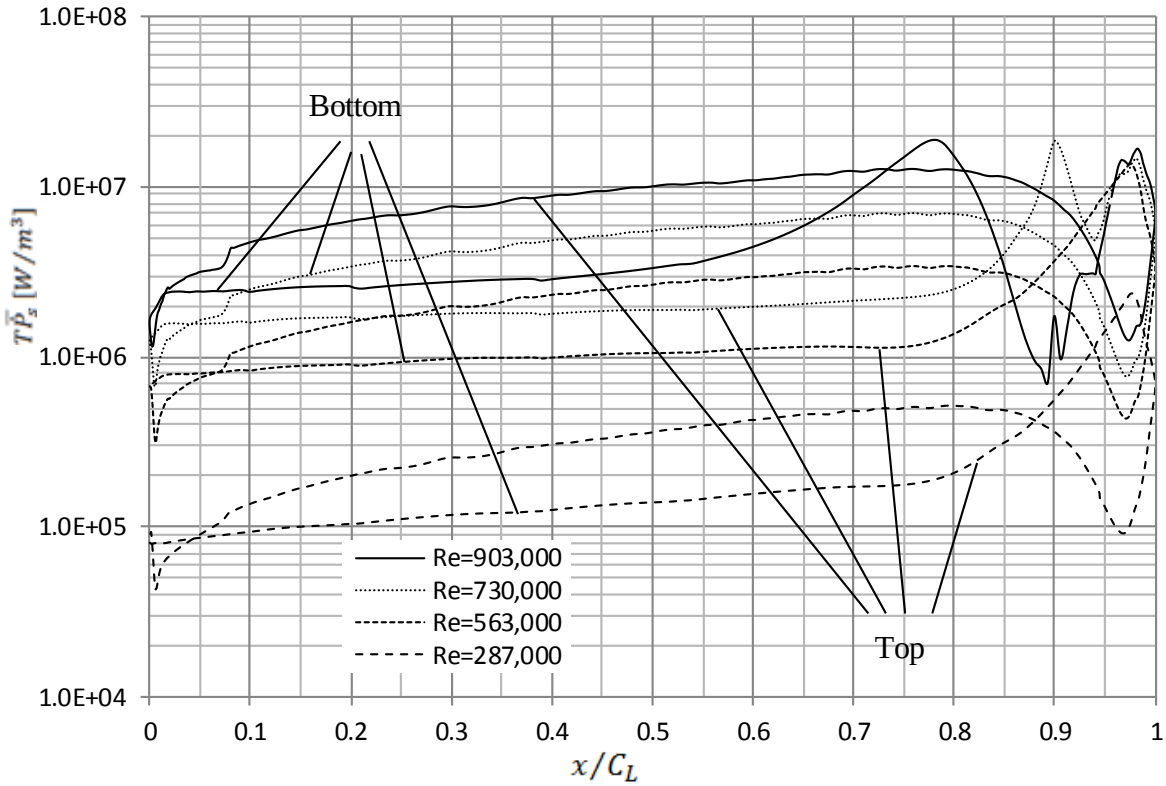

Figure 5-21: Entropy production on NACA 4412 hydrofoil (at $\alpha_0 = -4^{\circ}$)

The figures plotted in this section cover all CFD case studies for NACA 4412 hydrofoil with different Reynolds number at different angles of attack. The results are compared with experimental data carried out in water tunnel. These figures also reveal the microcosmical physical processes of two-phase flow undergoing mass transfer. The physical processes might be observed from lab testing but it is a challenge to carry out quantitative research. As mentioned previously, in this research entropy production is formulated with four respects, and comprehensive descriptions of each item are given separately in these figures. Results of simulation with a typical angle of attack ($\alpha_0 = +8^{\circ}$) and Reynolds number (Re = 903,000) are plotted from Figs. 5-8 to 5-11. The mean viscous dissipation Φ_m^{μ} is proportional to the product of the gradient of mean velocity and

mixture dynamic viscosity. When cavitation occurs, water vapor occupies a larger proportion of the volume fraction resulting in a smaller mixture dynamic viscosity as compared to the dynamic viscosity of liquid water. The turbulent dissipation Φ_m^T is caused by Reynolds shear stress $-\rho\overline{\mathbf{u}_m'\mathbf{u}_m'}$. Similar to single phase turbulent flow, the two-phase turbulence is resulted from the mixture velocity fluctuation. A new item, diffusion dissipation Φ_m^D is introduced as one of the four items which contribute entropy production. One can image that there is friction force existing between two phases as they have slip velocity. This diffusion is illustrated in Fig. 5-10. Entropy production due to cavitation is the key topic in this study. This irreversibility is shown in Fig. 5-11. The effects of the energy source and the momentum sources from interfaces cause energy exchanges and phase change. This process converts the kinetic energy into internal energy to compensate for the latent heat. Fig. 5-12 shows summary of above four effects which form the total entropy production.

Entropy production around NACA 4412 hydrofoil at the same angle of attack for different Reynolds numbers is plotted in Fig. 5-13. We can notice that for cavitating flow entropy production rise with increase in Reynolds number. This phenomenon can be explained that higher Reynolds number causes larger velocity gradient, higher Reynolds shear stress, and more intense phase change on the upper surface. All of the factors intensify this physical process.

From Figs 5-14 to 5-21, entropy production in the top boundaries as well as around the hydrofoil is illustrated. Instead of showing four items separately like Figs. 5-8 to 5-11, these figures summarize these items to show the total entropy production. It is observed that with the same Reynolds number 903,000, entropy production either along

the eight lines or around the foil highly depends on the angle of attack. At $\alpha_0 = 0^{\circ}$, the foil has smallest frontal area allowing flow to pass the profile with streamlined surrounding even under circumstances of the high Reynolds number. Entropy production mainly stems from mean viscous dissipation while other three items are not dominant. At $\alpha_0 = +12^{\circ}$, flow passes maximum frontal area of the profile, which causes intensive turbulence near the foil surface.

5.7 Validation and summary

The results in Fig.5-19 are consistent with Fig.5-7 as both represent the circumstances of the hydrofoil at the same angle of attack, $\alpha_0 = +12^{\circ}$. At Re=903,000 cavitation has intense occurrence at this position when cavitation number C_a drops down to about 0.3. Fig.5-7 gives a good agreement of cavitation extent of occurrence on the top area of the hydrofoils, while Fig.5-19 shows entropy production rate around the hydrofoils. On the top surface, a flow undergoes separation and phase change hence causing drastic changes in entropy production.

The integral values of the entropy production rate were obtained by volume integration of the four physical effects. Validation of the entropy production model for two-phase cavitation flow was performed based on an energy balance. Table 5-2 lists the comparisons made between the destroyed exergy and dissipated thermal energy. The definitions of these parameters are given as follows.

$$\dot{Q} = \left(\oiint_{A_{in}} \frac{\dot{m} p_{in}}{\rho_m} dA - \oiint_{A_{out}} \frac{\dot{m} p_{out}}{\rho_m} dA\right) + \left(\oiint_{A_{in}} \frac{1}{2} \mathbf{u}_m^3 \rho_m \, dA - \oiint_{A_{out}} \frac{1}{2} \mathbf{u}_m^3 \rho_m dA\right) \tag{5.61}$$

$$\dot{E}_x = \iiint_V \left(\Phi_m^{\mu} + \Phi_m^{T} + \Phi_m^{D} + \Phi_m^{\sigma}\right) dV \tag{5.62}$$

$$E = \frac{\dot{Q} - \dot{E}_x}{\dot{Q}} \times 100\% \quad (5.63)$$

Table 5-2: Predicted error of entropy production models

Angle of attack	Re Reynolds number	$\dot{Q}$ heat transfer [W]	$\dot{E}_x$ Entropy Model [W]	Error [100%]
$\alpha_0 = -4^\circ$	903,000	0.738	0.718	2.65
	730,000	0.229	0.228	0.53
	563,000	0.096	0.094	2.00
	287,000	0.015	0.014	1.98
$\alpha_0 = 0^\circ$	903,000	0.335	0.330	1.50
	730,000	0.185	0.182	1.40
	563,000	0.089	0.087	1.87
	287,000	0.014	0.013	2.82
$\alpha_0 = +4^\circ$	903,000	0.721	0.704	2.35
	730,000	0.230	0.220	4.31
	563,000	0.111	0.106	3.62
	287,000	0.017	0.016	4.63
$\alpha_0 = +8^\circ$	903,000	2.412	2.318	3.91
	730,000	0.914	0.874	4.32
	563,000	0.165	0.164	0.92
	287,000	0.024	0.023	1.50
$\alpha_0 = +12^\circ$	903,000	3.872	3.790	2.11
	730,000	1.417	1.309	7.61
	563,000	0.288	0.249	5.66
	287,000	0.040	0.038	5.11

This new formulation of entropy production for two-phase cavitation flow predicts a local loss with high precision. An energy balance method was used to validate and verify the models. The errors for different cases were presented to compare accuracy.

Chapter 6

Entropy model verification with 3-D propeller

6.1 Introduction

This chapter is concerned with a computational study of cavitating flow around a marine propeller, solving with the RANS equations applied to a cavitation model. A DTMB propeller model P5168 was selected to verify the entropy production model for 3-D cavitation flow. P5168 is a five-bladed, controllable-pitch propeller with a design advance ratio of 1.27. The propeller is left-handed with a radius of 15.86 inches. Because of its well-documented data, P5168 has become an international benchmark used extensively for CFD validation. Open-water measurements were made by Chesnakas and Jessup [117] over a wide range of advance ratios. Detailed velocity field LDV measurements were presented in Ref. [117]. Computational conditions were set to the corresponding experimental conditions. The k- ε model was used for turbulence closure in the simulations (see Eqs.5.17 and 5.18). Computational results will be analyzed and validated against the experimental data. The pressure distribution on the blade and hub surface, as well as velocity and turbulence quantities in the propeller wake, will be used to analyze and verify the flow field.

For the present study, the mixture fluid methods presented in Chapter 4 are adopted for mass transfer between phases and extended for interphase slip velocity (see Eq. (5.9)). For the validation of CFD, simulations of open-water performance and flow field analysis for a cavitating propeller have been conducted.

6.2 Geometrical modeling and grid generation

For the P5168 propeller, a 3-D blade profile was simulated from several 3-D cylindrical blade sections represented by a series of hydrofoils. Fifteen hydrofoils were twisted into different angles on separate cylinders. These hydrofoils were stacked in the span wise direction and blended together from hub to tip to form the 3-D curvature surface. After adding other geometrical features like the hub, the P5168 propeller's 3-D geometry was created (see Fig.6-1).

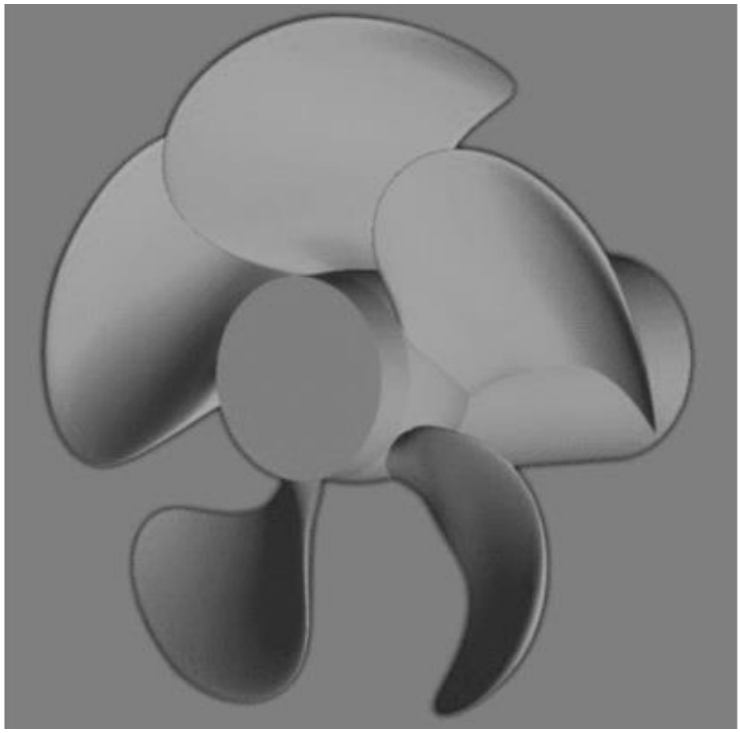

Figure 6-1: Geometrical construction of propeller 5168

The P5168 geometry is defined in a tabular form in Ref. [117]. FORTRAN codes were produced to obtain up to 159 data files of the coordinates of points at each section. Every section has 2020 points which were joined together to form a very smooth curve on a cylindrical surface. These 159 curves were connected defining the blade surface.

The simulated geometry uses an infinite shaft of constant radius, whereas the experimental blade included a cylindrical fairwater that extended 96.8 mm downstream of the hub. The geometry in Ref. [117] has a small increase in hub radius near the propeller. This feature was not included in the CFD model.

For the P5168 propeller, the simulations resembled open-channel tests in which the physical domain was subdivided into simpler shapes and formed into a large cylinder surrounding the propeller. The overall domain extends a distance of 1.9D upstream, 5.4D downstream, and 2.8D outward in the radial direction. The similar domain size was adopted for study of hexa-structured and hybrid-unstructured meshing with the same propeller using CFX [118]. Blade surfaces and a hub were centered at the Y axis on the coordinate system and aligned with uniform inflow (see Fig.6-2).

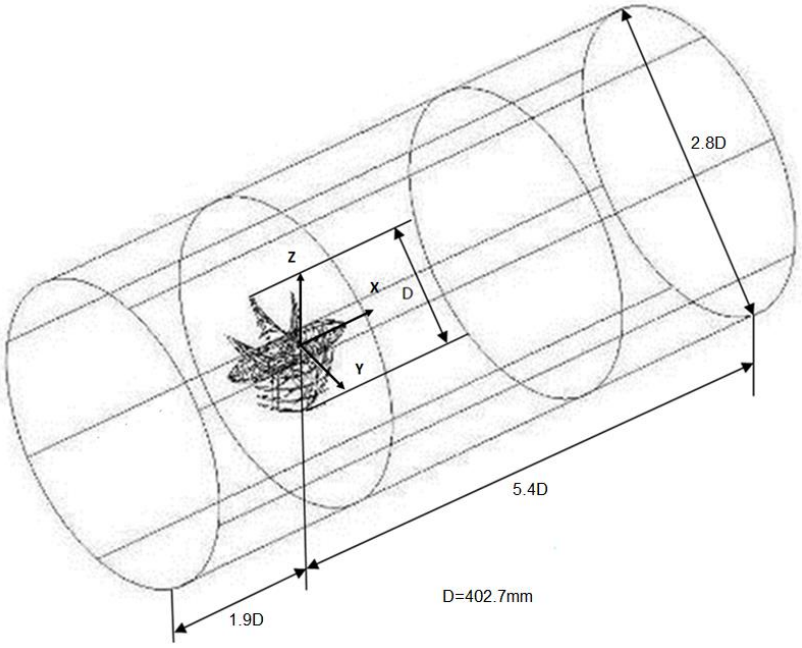

Figure 6-2: Testing and CFD domain of propeller P5168

The grid type has an important role in accuracy and computational time of the numerical solution. One of the most difficult tasks in CFD is mesh generation, especially for 3D analysis. The choice of whether to use a structured or an unstructured mesh is very problem specific. Unstructured grid generation for complex geometry is usually much faster than structured grid generation. However, if the geometry is only slightly modified from a previously existing geometry with a structured grid, then structured grid generation can occur very fast. Also it takes less CPU time to achieve a converged solution if a structured grid is used rather than an unstructured grid [119]. In this study, grid generation was accomplished by CFX built-in grid generation software ICEM CFD [120]. A rotational periodic grid interface was used to map the complete propeller geometry and connect the symmetry planes or surfaces. This type of grid interface is adequate for the simulations because symmetric results in many identical regions of the flow field repeat themselves with rotational periodicity. The computational domain was reduced to one fifth of the geometry. Using four symmetry planes and two curvature surfaces, the computational domain was sub-divided into five axial symmetrical sub-domains (see Fig. 6-3).

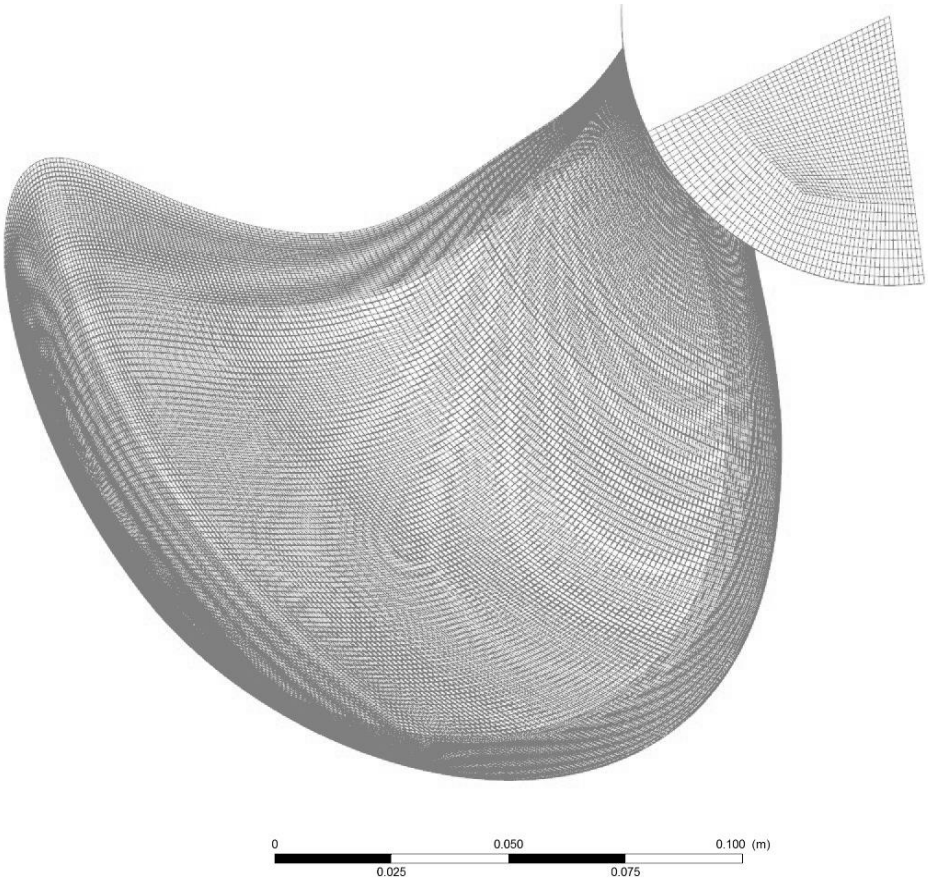

Figure 6-3: Axial symmetrical sub-domains for periodic boundary conditions

For propeller P5168, it is assumed that the inflow is uniform in the circumferential direction and is steady. This assumption allows the computational domain to be reduced to a single blade passage through the use of rotationally periodic boundary conditions.

6.3 Boundary conditions

The inlet boundary condition is set to the uniform free stream value, with a normal velocity range from 2 to11 m/s and a medium turbulence intensity of 5%. The pressure was extrapolated from inside the domain to the boundary. A zero gradient boundary condition was set at the outlet, with a relative static pressure of 51,957 Pa,

considering the flow direction normal to the boundary. As discussed above, the computational domain was reduced to one fifth of the geometry (see Fig. 6-4). The periodic boundary condition was then implemented. This approach was adopted to reduce computational time. The no-slip rotating wall boundary condition is prescribed on the surfaces of the blade and hub. This option allows the wall to rotate with a specified angular velocity, and the fluid immediately next to the wall assumes the velocity of the wall. Similarly, the free-slip boundary condition is set on the domain cylinder.

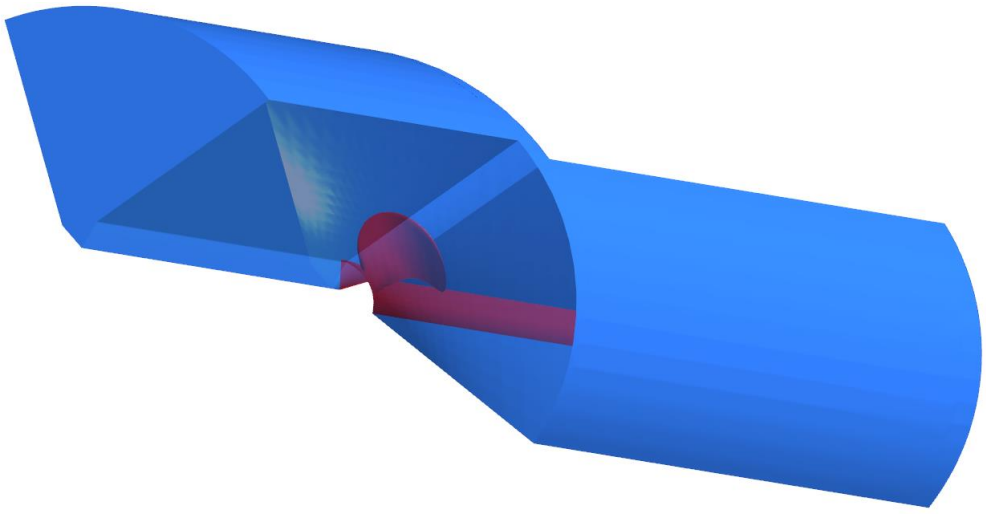

Figure 6-4: Design of the computational domain

There is a difference between flows around a rotating propeller in open water versus water flow past a propeller. For a steady-state analysis, the Multiple Rotating Reference Frame (MRF) approach can be used to simulate the first flow case. This method assumes that the flow is steady and the interaction between stationary and rotating frame is weak. In the second case, the blade and hub surfaces can be treated as moving walls and simply set wall angular velocities without any rotating reference frame.

CFD validations were conducted for four advance ratios: $J = \frac{U_\infty}{nD}$ equal to 0.98, 1.10 1.27, and 1.52, where U_∞ is the inflow speed and n is the number of revolutions in rpm, following the experimental conditions. The definition of advance ratio J is the ratio between the distance the propeller moves forward through the fluid during one revolution and the diameter of the propeller. In this case, the propeller does not move along its axial direction, and the water is flowing in the opposite direction. Thus, the incoming flow velocity is measured instead of the propeller forward velocity. Although the J = 1.10 case is the most interesting one in terms of the tip vortex flow, all the cases were considered in the present study, which is focused on the general open water propeller performance prediction. Table 6-1 presents the computational conditions.

Table 6-1: Computational conditions

$J = \frac{U_\infty}{nD}$	D [m]	n [rpm]	U_∞ [m/s]
0.98	0.4	1200	7.89
1.10	0.4	1450	10.70
1.27	0.4	1300	11.08
1.52	0.4	1150	11.73

6.4 Grid independence study

Figure 6-5 presents the curves of mixture velocity $\mathbf{u}_m$ on a hydrofoil section obtained on three different meshes using a two-phase mixture $k-\varepsilon$ model. Grid independence was assessed for a single advance ratio J =1.1. Over the three mess cases considered the influence on the prediction of $\mathbf{u}_m$ was not significant, less than 1.5%. Initial computations were conducted on the 5 million element mesh. After obtaining a

converged solution, the mesh was refined to 18 million to increase the resolution largely in the tip vortex region. The refined mesh provided less than 1% improvement in terms of $\mathbf{u}_m$, suggesting that the initial mesh resolution is much more important than the later mesh refinement. The mesh was further refined to 25 million elements with little change in local flow quantities. However the computing time in using this high definition mesh is much longer; hence, it increases the computation cost. The 18 million element mesh was used in this study.

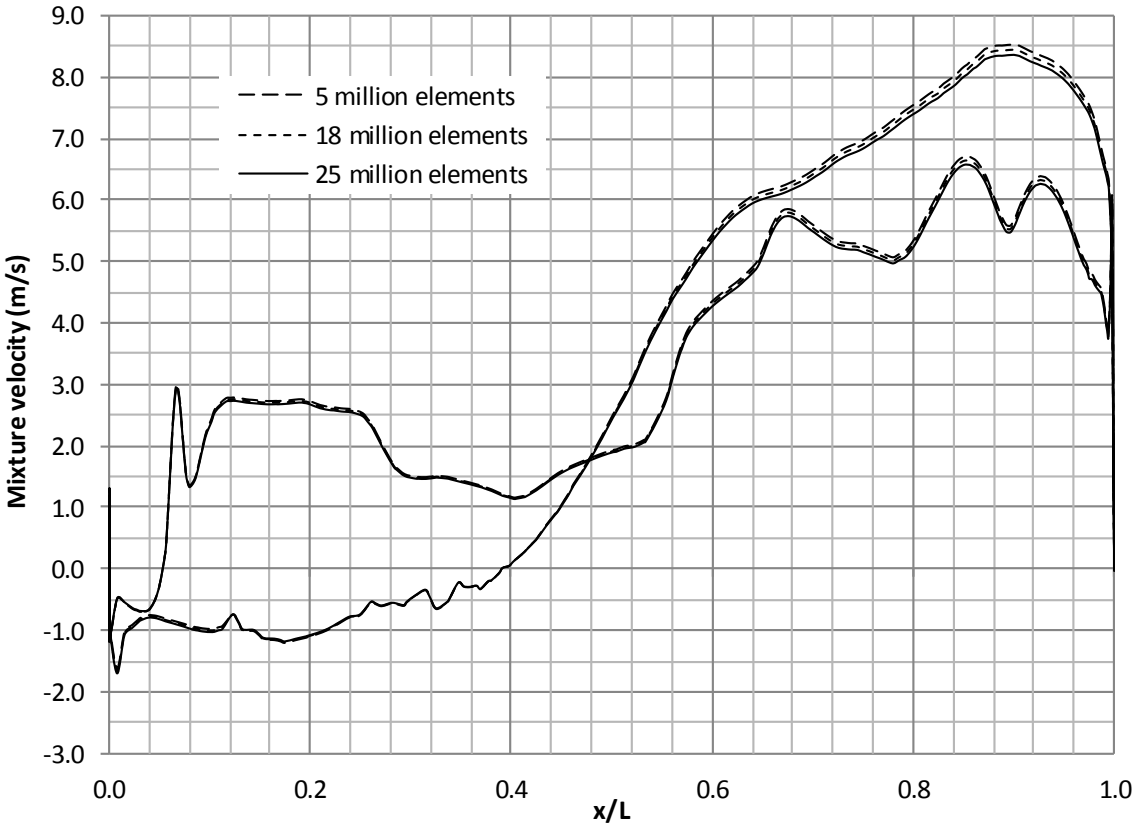

Figure 6-5: Mixture velocity on the cross-section of the blade

6.5 Velocity field of propeller P5168

The numerical solutions of cavitation flow mixture velocities at x/R = 0.2386 with different J's are plotted in Figs. 6-6 to 6-9. These figures show the projections of the

mixture velocity $\mathbf{u}_m$ on the plane. The definition of $\mathbf{u}_m$ can be found in Eq. (4.2). These velocity fields are selected for CFD validations against measured data. The velocity vector $\mathbf{u}_m$ is decomposed into three components: the axial velocity U_x, the tangential velocity U_t , and the radial velocity U_r. These velocity components are normalized by U_∞, the uniform velocity at inlet.

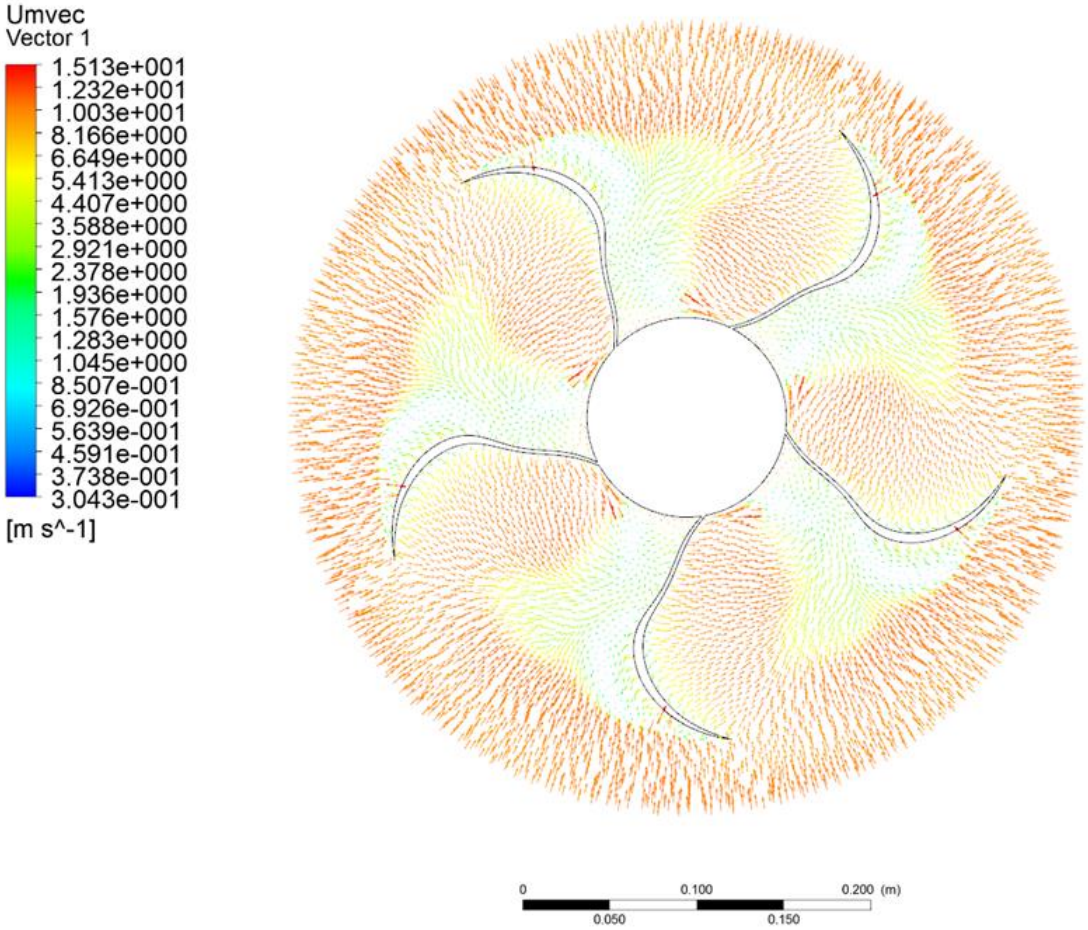

Figure 6-6: Velocity contours and vectors (J = 0.98 at x/R = 0.2386)

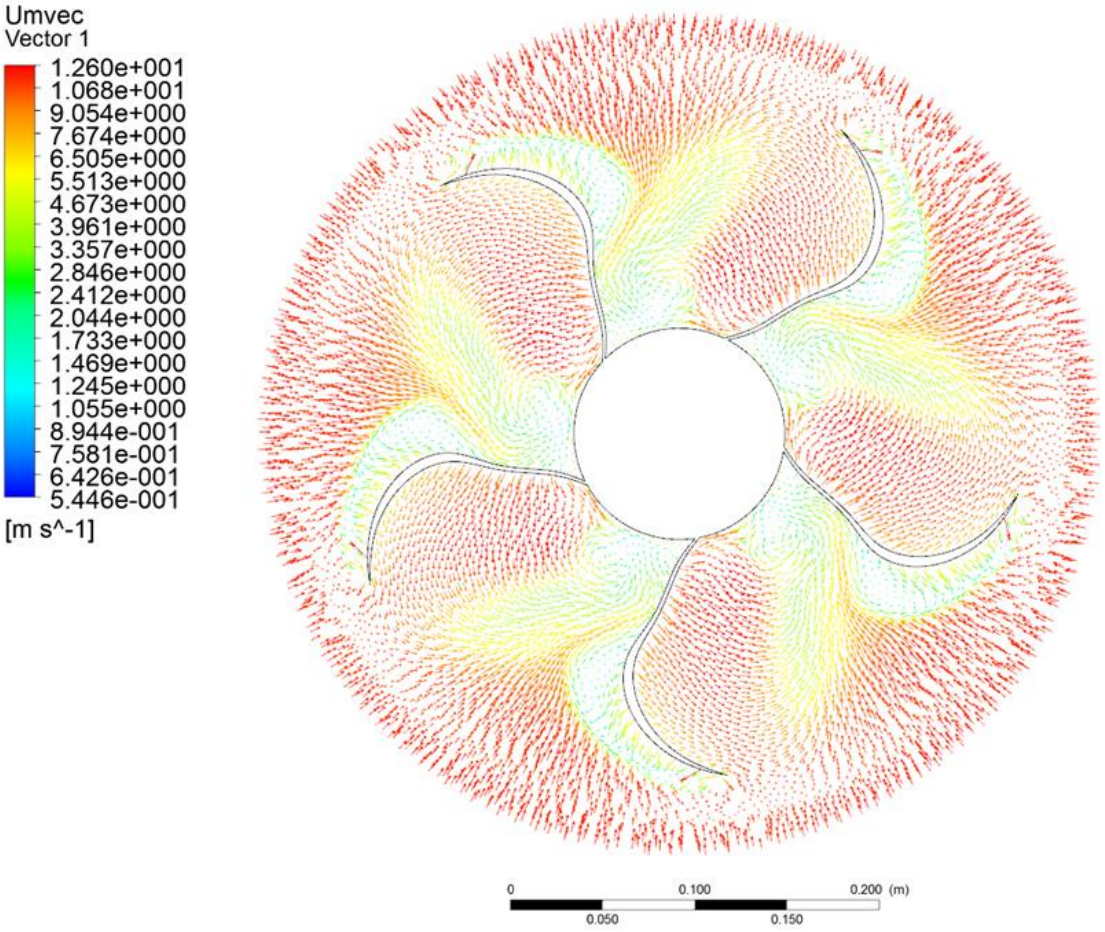

Figure 6-7: Velocity contours and vectors (J = 1.10 at x/R = 0.2386)

.

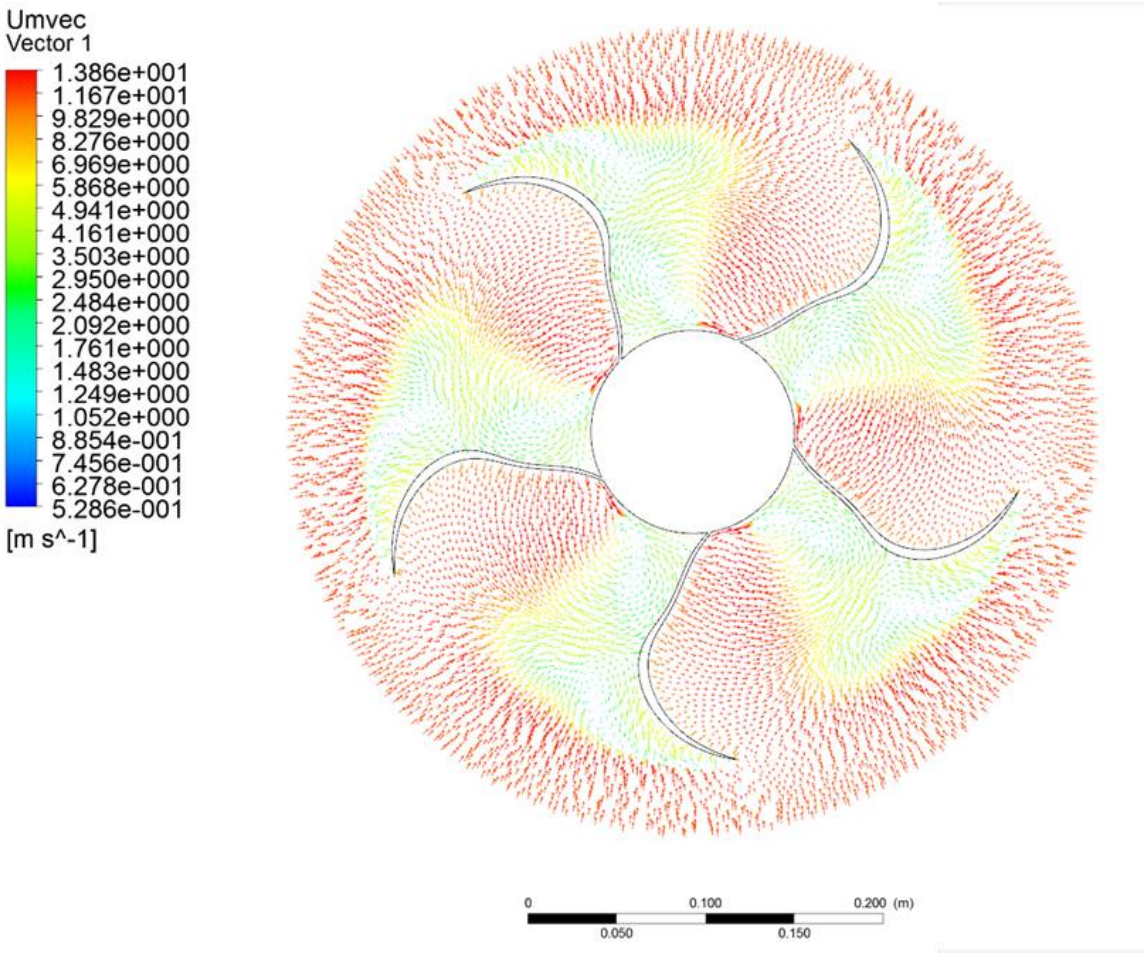

Figure 6-8: Velocity contours and vectors (J = 1.27 at x/R = 0.2386)

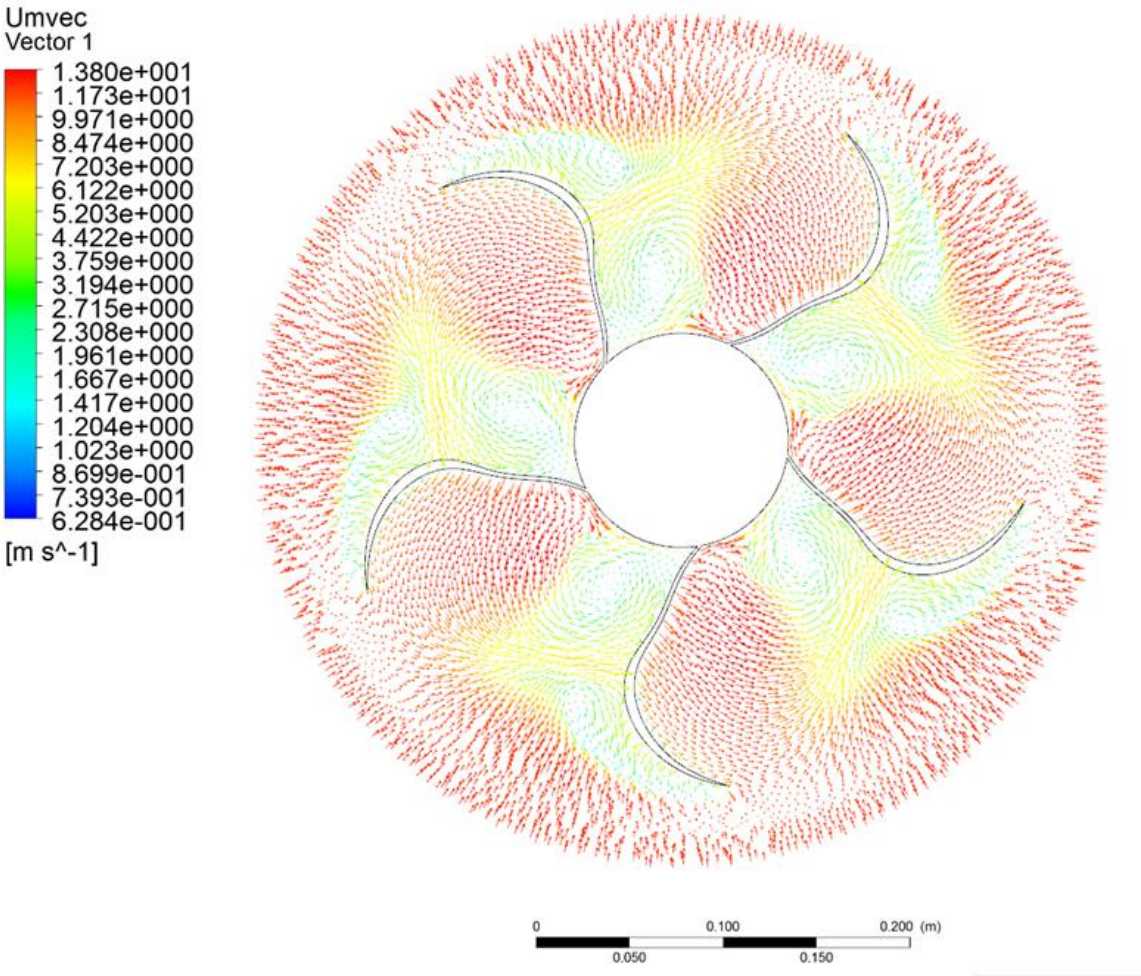

Figure 6-9: Velocity contours and vectors (J = 1.52 at x/R = 0.2386)

Figure 6-10 shows the measured and the CFD results that are circumferentially averaged from normalized axial velocity U_x by U_∞ at x/R = 0.2386 with varying J. The present CFD solutions reproduce the trend well. It can be seen that a large U_x is present with its maximum in the mid-span area, where the blade has its highest pitch angle.

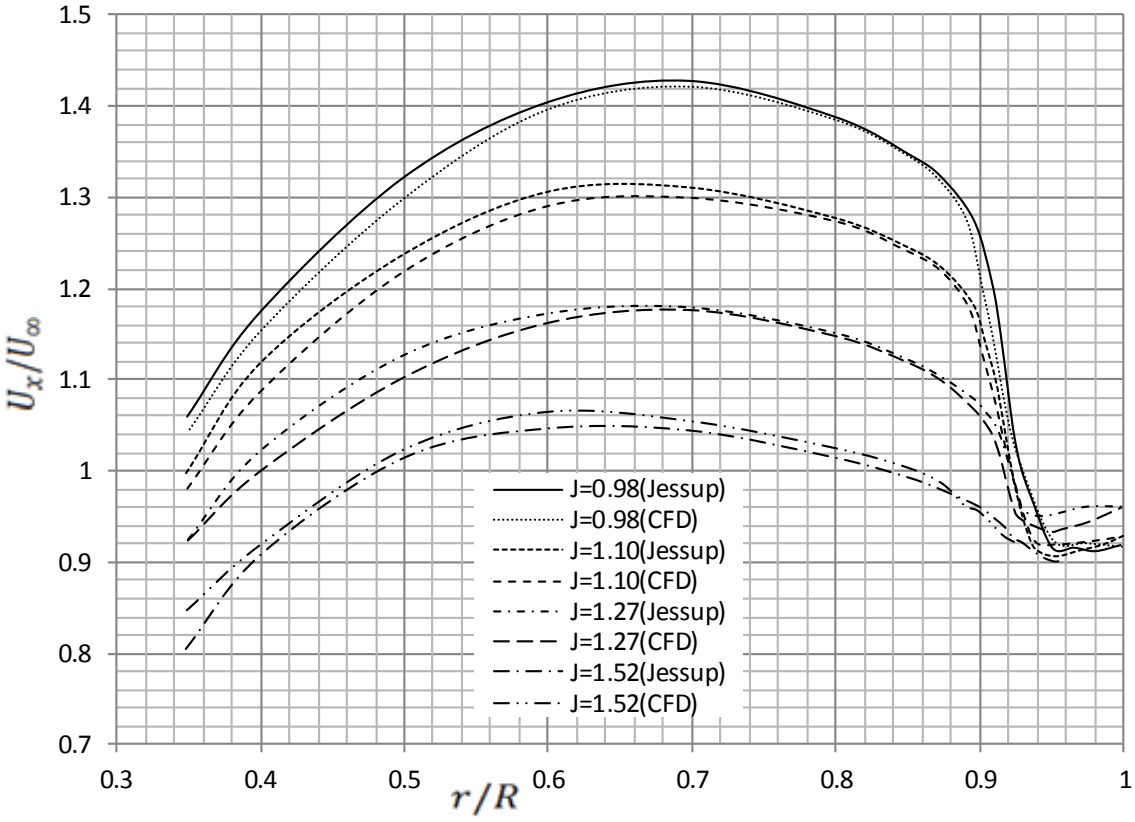

Figure 6-10: U_x/U_∞(normalized axial velocity) vs. *r/R*, *x/R* = 0.2386 [117]

Figure 6-11 shows the circumferentially averaged normalized tangential velocity U_t byU_∞. U_t Increases with an increasing radius and reaches the maximum value at $\mathrm{r/R} = 0.6$, then gradually decreases. The CFD results show good agreement with the measured velocities.

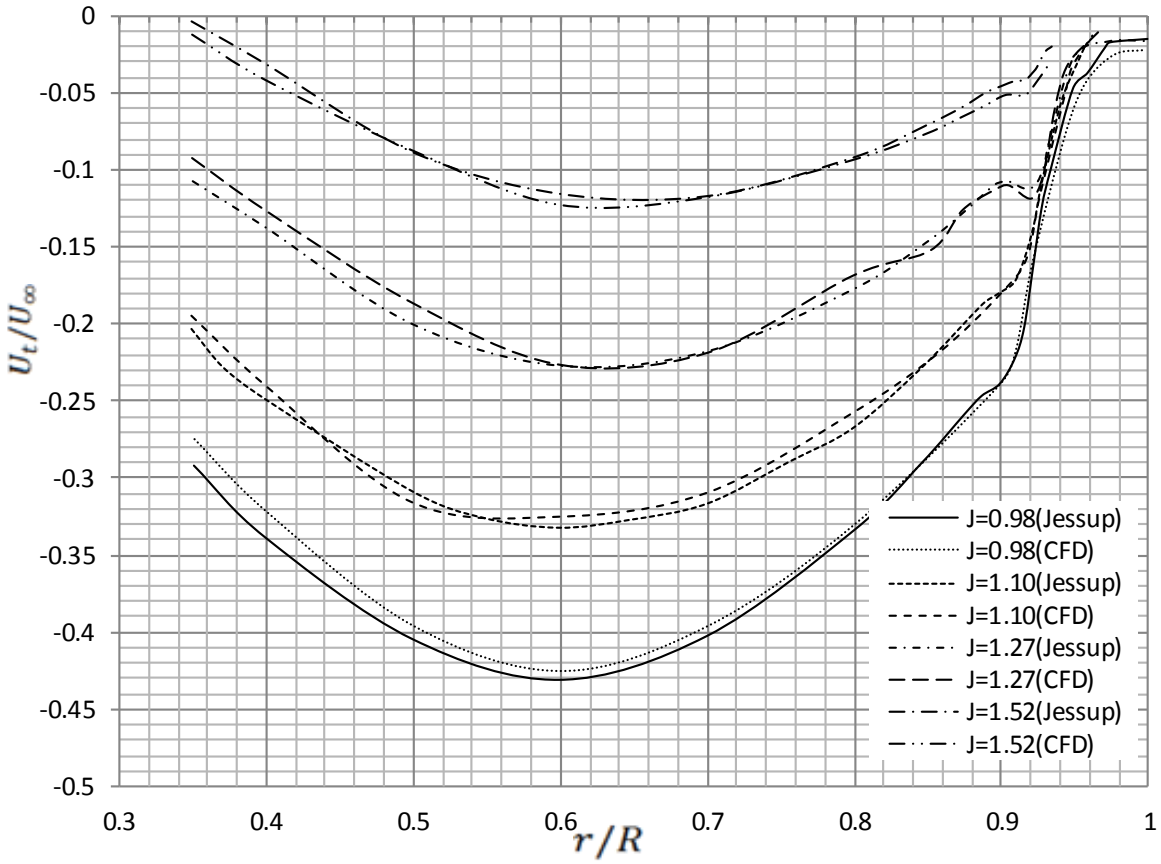

Figure 6-11: U_t/U_∞(Normalized tangential velocity) vs. r/R, x/R = 0.2386 [117]

Figure 6-12 presents the circumferentially averaged radial velocity U_r normalized by U_∞ vs. normalized radial coordinate (r/R) on the x/R = 0.2386 plane. The negative values of U_r indicate the flow contraction due to the propeller action.

The present solutions are consistent with the variation in the measured results. Generally, they show good agreement with test results with modest deviation from the measured data.

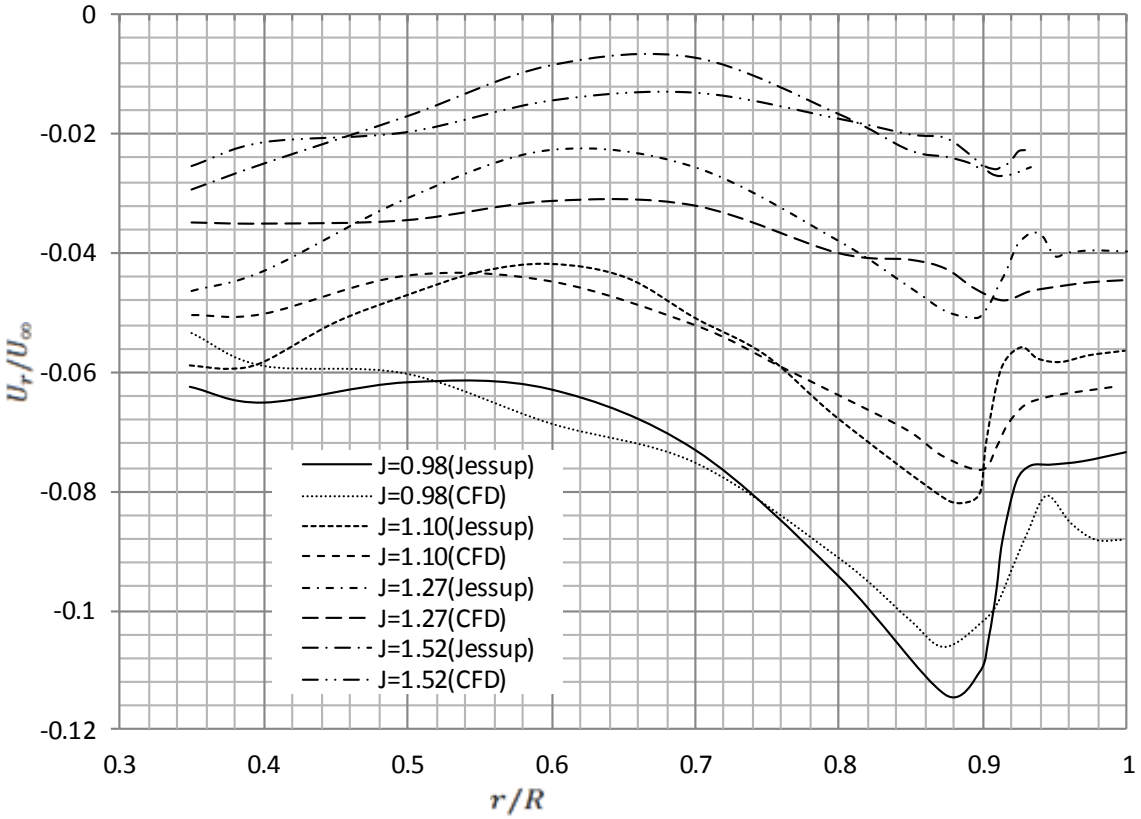

Figure 6-12: U_r/U_∞(Normalized Radial velocity) vs. *r/R*, *x/R* = 0.2386 [117]

Advance ratios J reflect the load exerted on the propeller. These Figures (6-10, 6-11, and 6-12) show that as J decreases, the magnitude of all velocity components increases. At the tip, as U_x approaches 1, U_t approaches zero.

The overall agreement with the measured data for U_x and U_t is very good, except for the region near the hub, that is, at small r/R. This discrepancy is caused by the infinitely long hub with a relatively close inlet boundary to the blade center, which could result in unsatisfactory boundary layer development near the hub. The agreement for U_r is not as good as that for U_x and U_t. However, it should be noted that the values of U_r are smaller than those for U_x and U_t by an order of magnitude, and the trends are reasonably reproduced.

There are several reasons why there are deviations between experimental data and CFD results at the tip of the blades. First cavitation often occurs in the wake of a rotating propeller, like the location at x/R = 0.2386, where the velocity is very high near the tips of the blades, and the pressure is very low in the wake of the propeller. The bubble generation due to the cavitation makes the observation of velocities more difficult and less accurate resulting in the discrepancy from the results of numerical simulations. Second, the highly skewed geometry occurs on the tip of the blades. In order to precisely predict the velocity in the area, higher resolution is required for both experimental and numerical methods. But due to the limits of the computation resource, it is difficult to make the mesh finer, which results in the variation of velocity at the tip.

6.6 Entropy production with propeller P5168

The local irreversibility can be determined using the CFD results. Similar to the NACA hydrofoil case study, one case (J = 1.10 at x/R = 0.2386) is taken to represent each entropy production term in Eq. (5.36) to ascertain the varieties of physical effects in the cavitation flow on entropy production. Because the flow field is based on a 3D geometry, the 2D contours are taken as displaying the entropy and the individual terms of the irreversibility.

Figure 6-13 indicates that entropy production arising from dissipation due to mixture mean flow motion $\mathbf{u}_m$. The logarithmic representation of the mean viscous dissipation Φ_m^{μ} is illustrated. This dissipation is comparable to the viscous dissipation of the mean velocity field in a single-phase turbulent flow case. In two-phase flow, the viscous dissipation is the function of the mixture velocity gradient and the mixture dynamic viscosity, which varies with the volume fraction of the vapor phase. At this

particular location, the order of magnitude of the dissipation is relatively small compared with other terms of the irreversibility. It can be seen that the highest entropy production occurs in the tip region of the blade where the highest velocity gradient occurs. The mixture mean flow motion is illustrated in Fig. 6-6. It can be seen the drastic variations of $\mathbf{u}_m$ around the blade profiles.

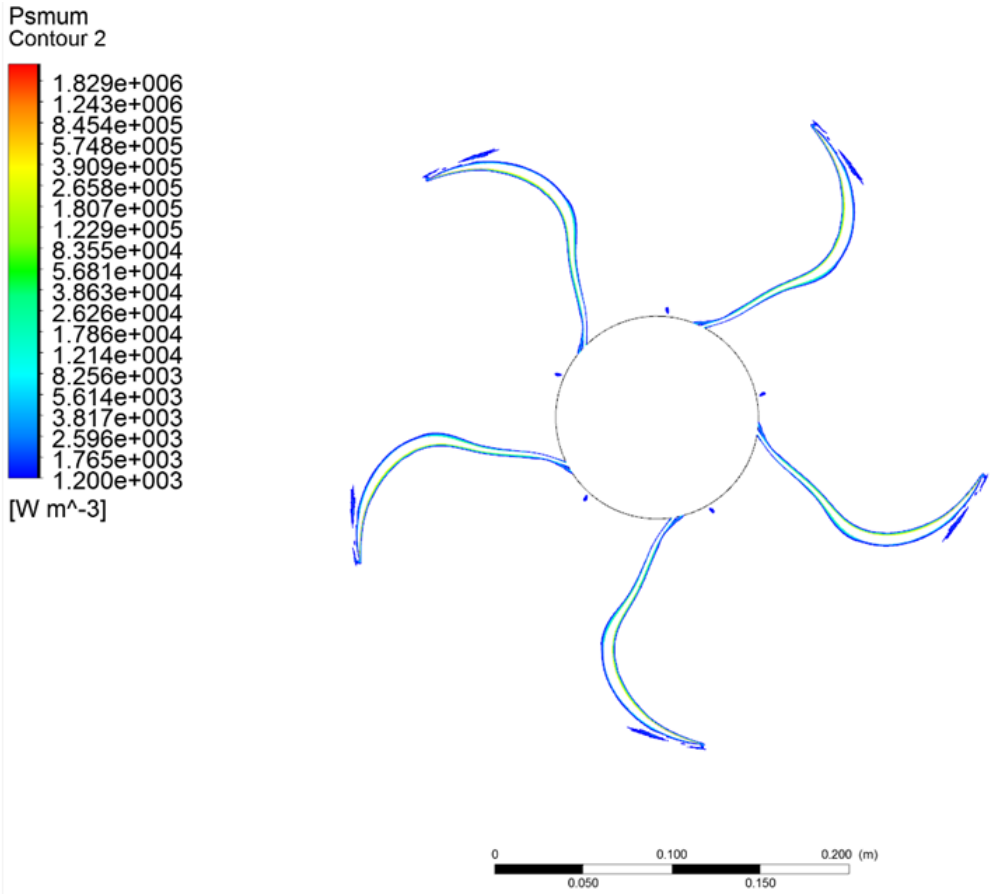

Figure 6-13: Contours of entropy production due to viscous shear stresses Φ_m^{μ} (J=1.10 at x/R=0.2386)

Figure 6-14 shows the contour of dissipation due to the Reynolds shear stress $-\rho\overline{\mathbf{u}_m'\mathbf{u}_m'}$ resulting from the mixture velocity fluctuation. The logarithmic representation of the turbulent dissipation Φ_m^T is illustrated (see Eq. (5.38)). Similar to the 2D hydrofoil

cases, this irreversibility can also be interpreted as the work done by the force $-\nabla(\overline{\mathbf{u}'_m\mathbf{u}'_m})$ in the streamwise direction and dissipated to thermal energy. It is comparable to the turbulent dissipation in a single-phase turbulent flow case. The highest dissipation rate occurs near the tip region of the section hydrofoil.

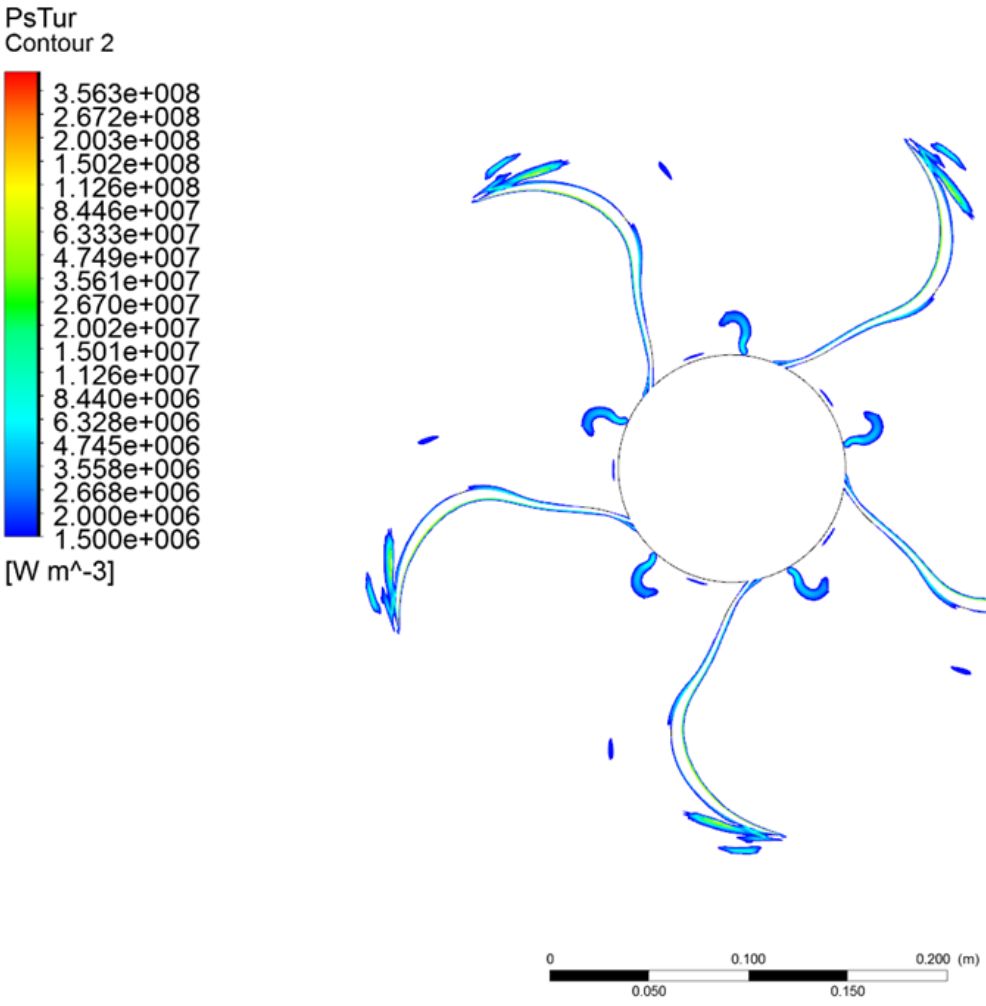

Figure 6-14: Contours of entropy production due to Reynolds shear stresses Φ_m^T(J = 1.10 at x/R = 0.2386)

Figure 6-15 shows the contour of the irreversibility due to the slip velocity between liquid and vapor phases. This term is exclusive to the drift-flux mixture model. This irreversibility exists in two-phase flow, but the mechanism of the physics still

remains an enigma. This term contributes less to the total entropy production because the order of magnitude is much smaller than it is for other production terms. For a homogeneous setting in CFD, this term does not exist because the same velocity field is taken for both liquid and vapor. For industrial applications, the two phase homogenous turbulence model is preferred as it simplifies the modeling of fluid dynamics in CFD and saves computation time.

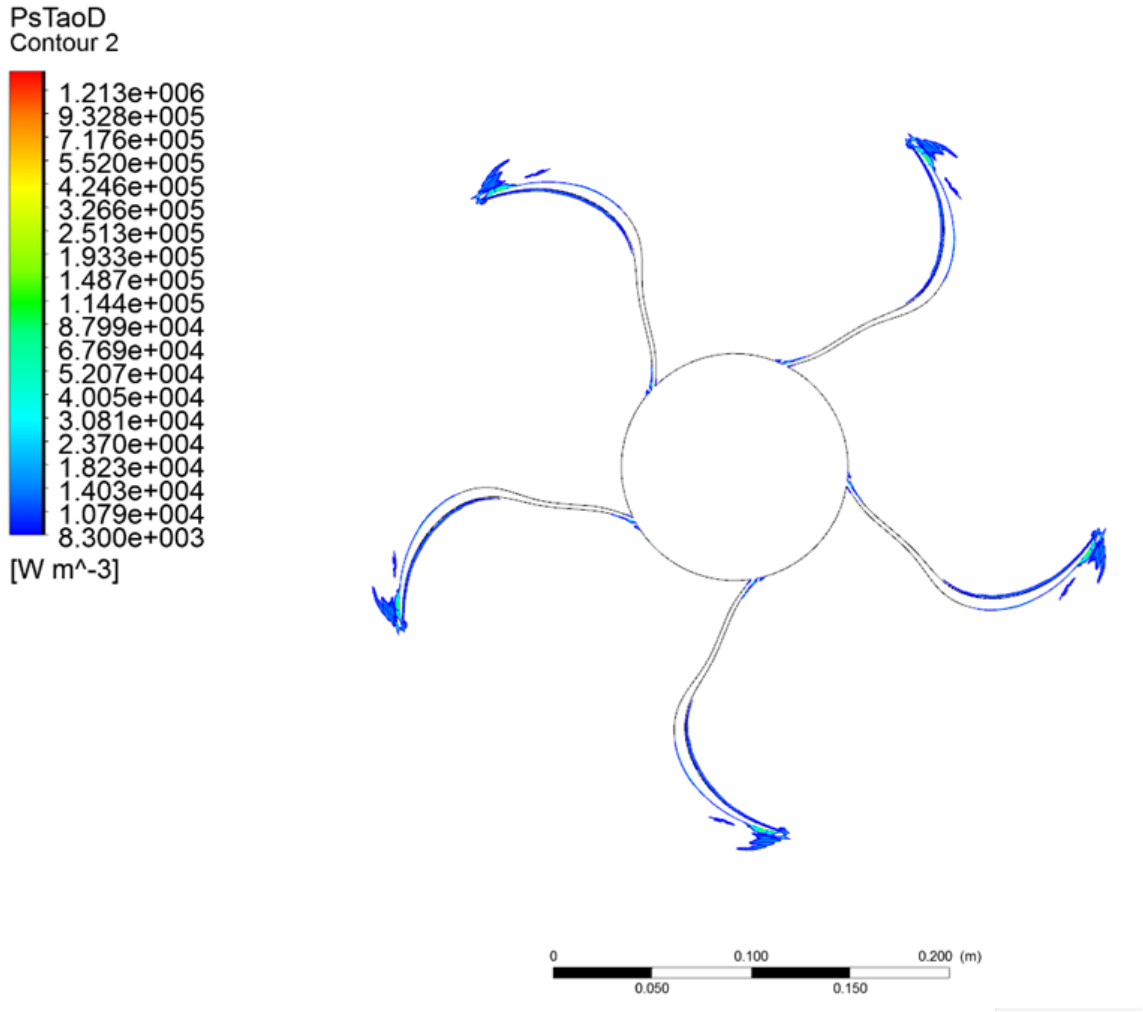

Figure 6-15: Contours of entropy production due to diffusion dissipation Φ_m^D (J = 1.10 at x/R = 0.2386)

Figure 6-16 shows the contours of entropy production due to cavitation. In cavitation flow, the large-energy exchanges are due to the latent heat absorbed during phase change. This process converts kinetic energy into internal energy to compensate for the loss of latent heat.

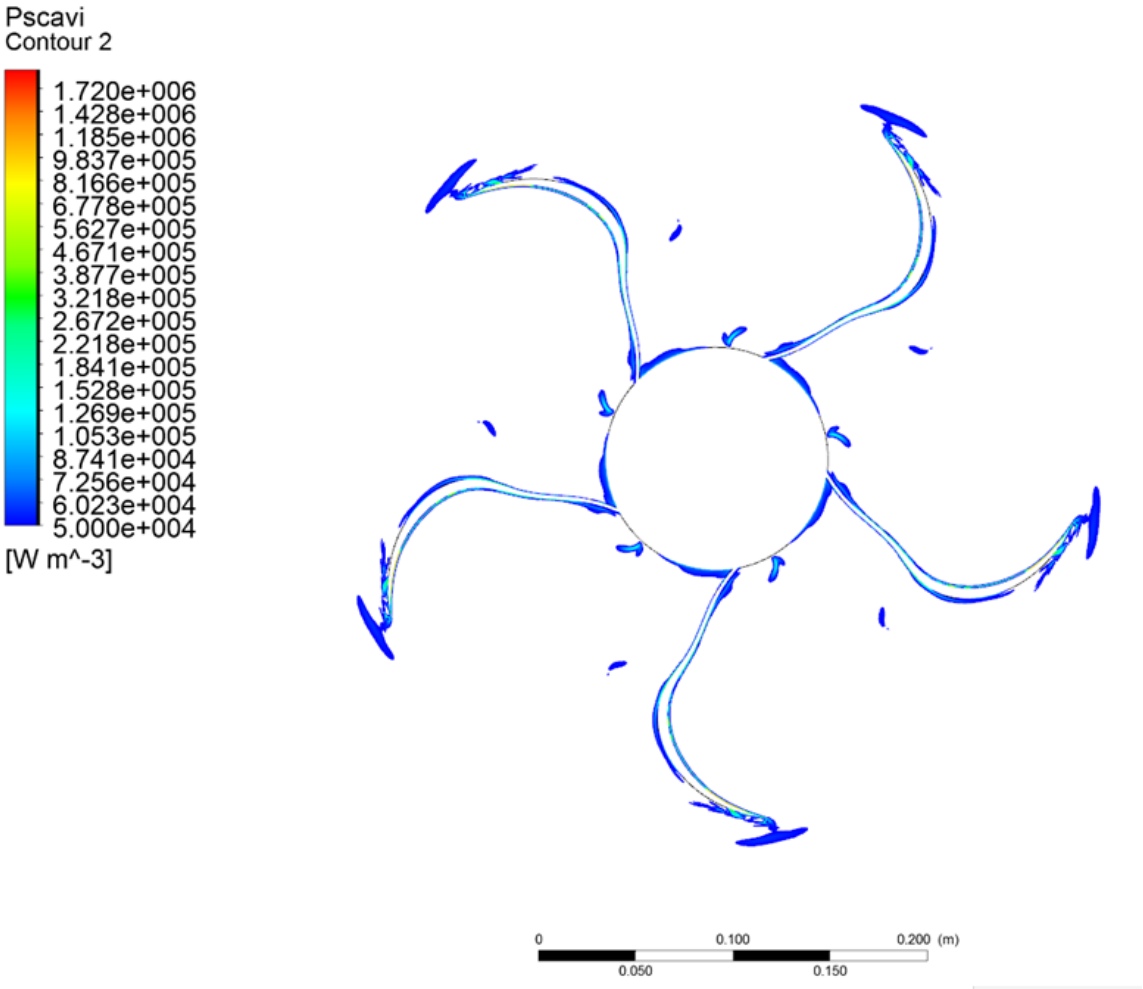

Figure 6-16: Contours of entropy production due to cavitation Φ_m^{σ} (J = 1.10 at x/R = 0.2386)

The energy dissipation due to the cavitation near the tip of the blade has a significant effect when cavitation occurs. The dissipation rates have relatively high values, and then drop off quickly away from the blades. Although this irreversibility occurs only in the regions where the cavitation occurs, the local energy loss has a higher level than the mean viscous dissipation. The formula used for this term is Eq. (5.51), where, the Rayleigh-Plesset equation is used to model cavitation rate.

The total entropy production is obtained by summarizing all production terms from, which are listed as follows:

Φ_m^{μ} Mixture viscous dissipation

Φ_m^{T} Mixture turbulent work effect

Φ_m^{D} Diffusion stress effect

Φ_m^{σ} Cavitation/phase change effect from interfaces

Fig. 6-17 shows the contours of total entropy production at J = 0.98 and x/R = 0.2386 on the plane.

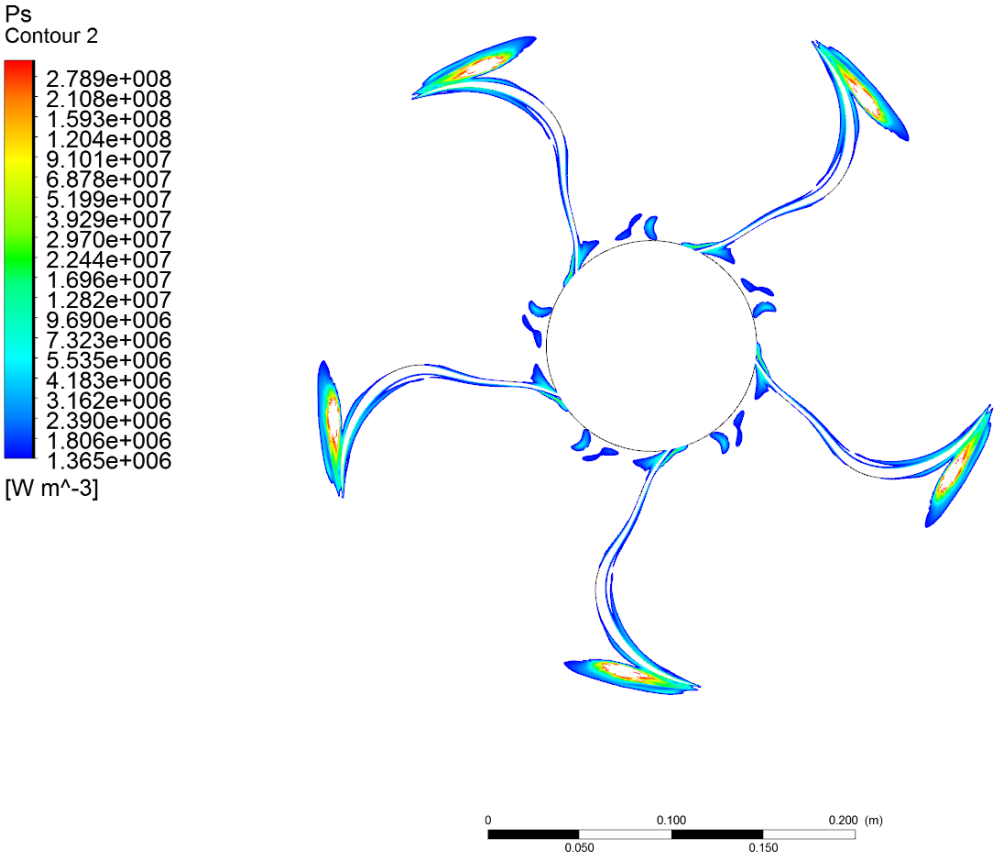

Figure 6-17: Contours of total entropy production (J = 0.98 at x/R = 0.2386)

Fig. 6-18 shows the contours of total entropy production at J = 1.10 and x/R = 0.2386 on the plane.

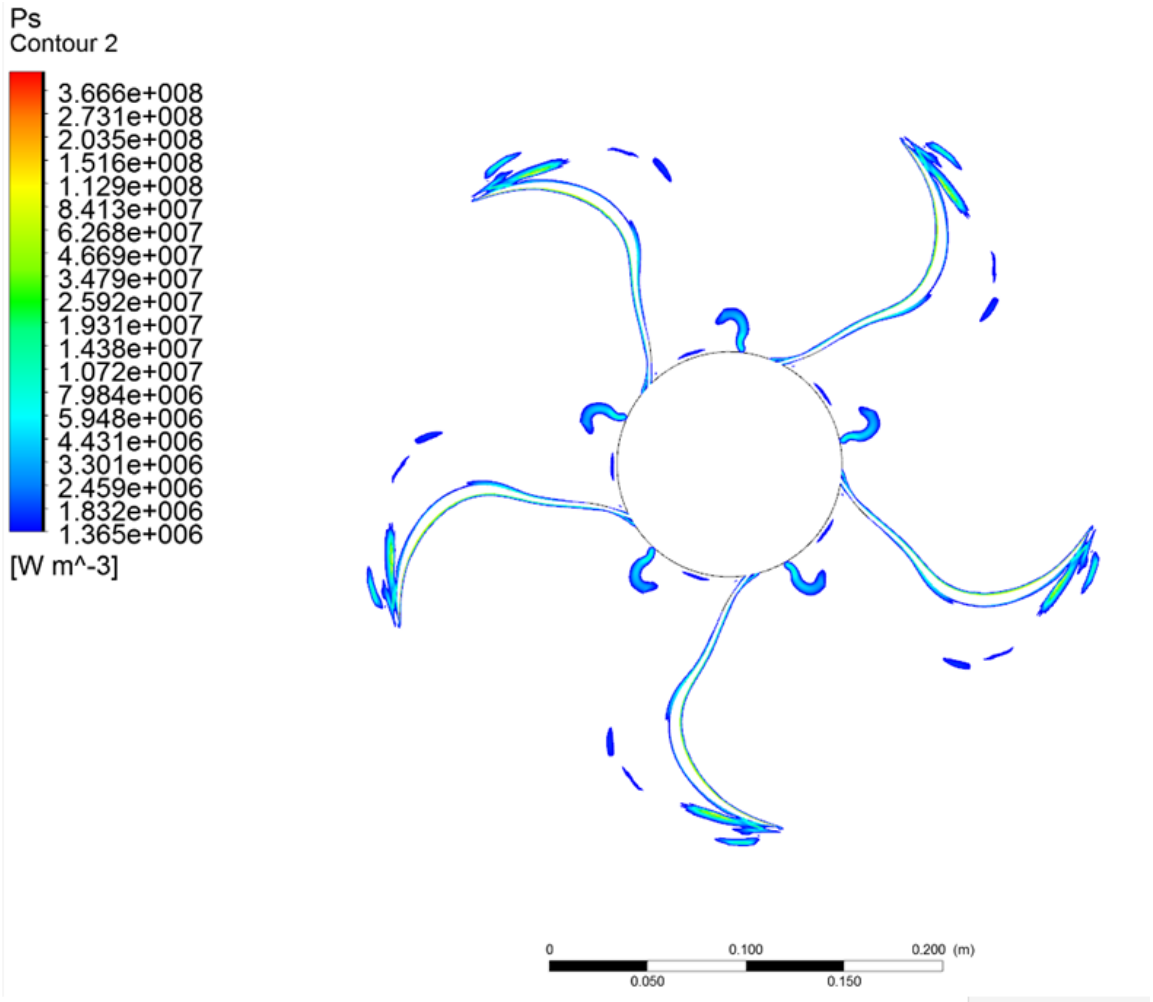

Figure 6-18: Contours of total entropy production (J = 1.10 at x/R = 0.2386)

Fig. 6-19 shows the contours of total entropy production at J = 1.27 and x/R = 0.2386 on the plane.

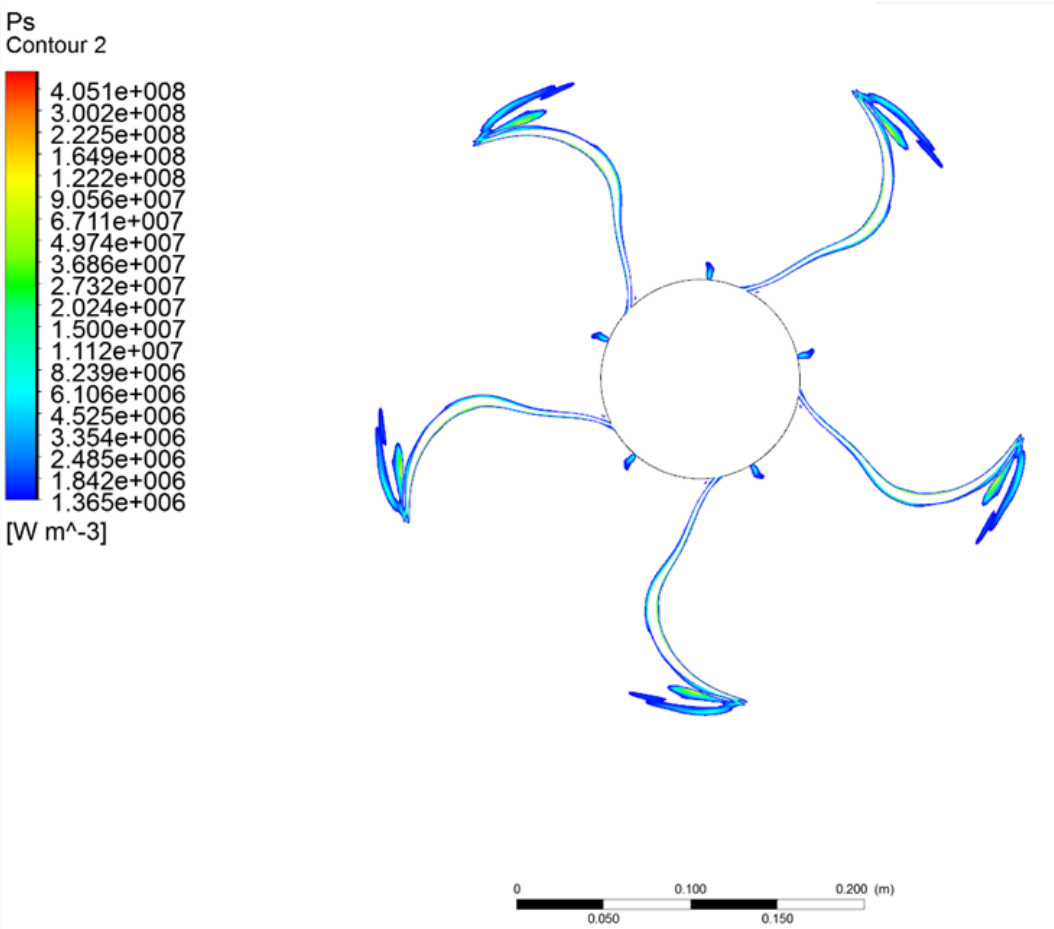

Figure 6-19: Contours of total entropy production (J = 1.27 at x/R = 0.2386)

Fig. 6-20 shows the contours of total entropy production at J = 1.52 and x/R = 0.2386 on the plane.

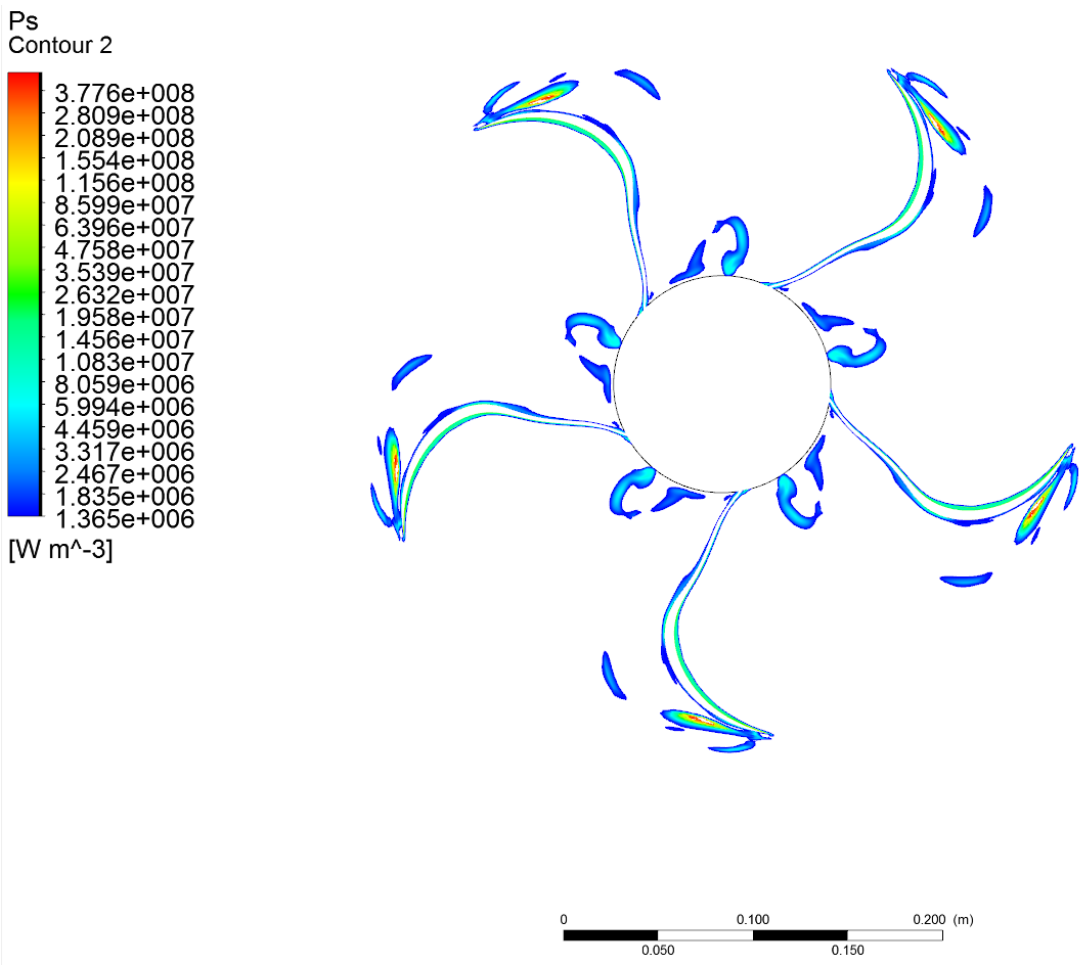

Figure 6-20: Contours of total entropy production (J = 1.52 at x/R = 0.2386)

From Figure 6-18 to 6-20 the variation of the entropy production contours can be analyzed. The highest entropy production occurs on the back of the tip in all cases, especially at J = 0.98. At the tip, flow reversal occurs and a vortex forms with a high velocity gradient and resulting high entropy production. Also, the cavitation intensity at the tip is very high, which can be seen from Fig. 6-16. High entropy production rates also present at the root of the blade.

Figure 6-21 shows entropy production on the cross-section of the blade for different advance ratios. The variations of the values depend on many factors. Because

the highly curved profile and the propeller contraction make the local flows complicated, the entropy production presents the circumstance of fluctuation near the root of the blade and at the tip of the blade. The verification of the entropy model largely depends on the energy balance method.

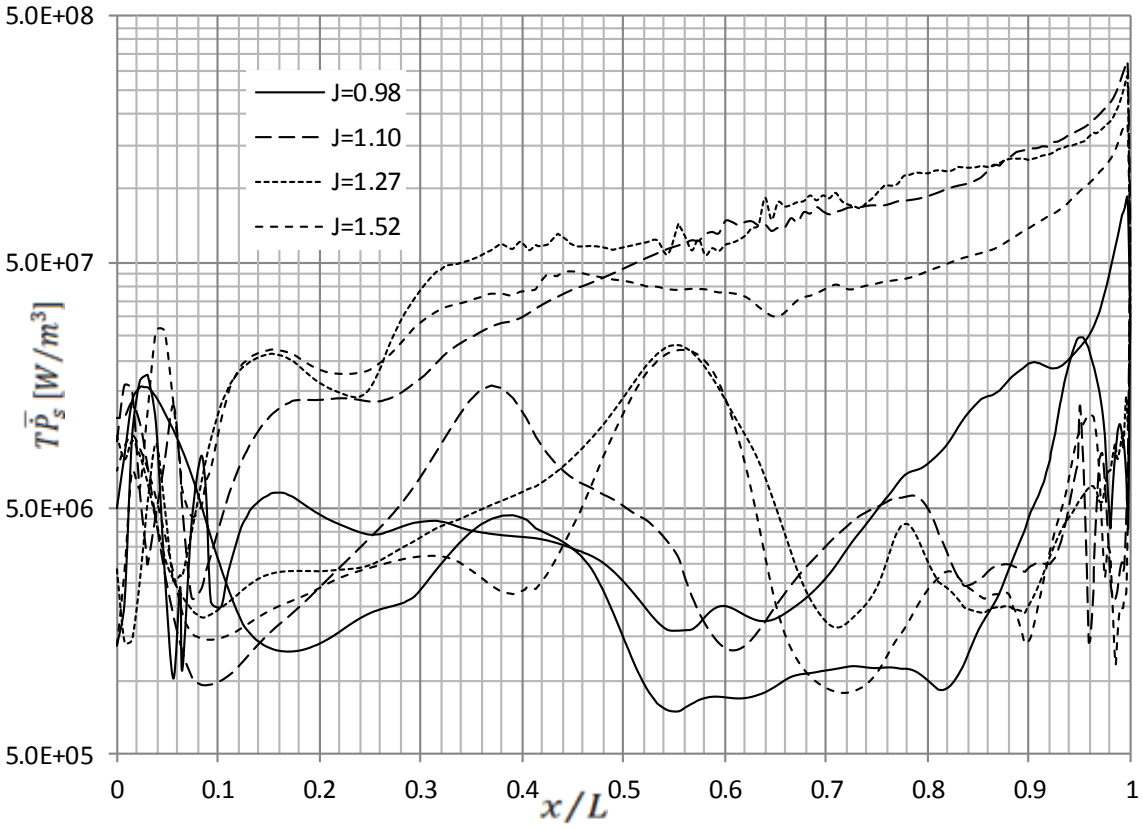

Figure 6-21: Entropy production on the cross-section of the blade

The entropy production contribution of each contributing term was studied for a series of propeller P5168 CFD case studies with different advance ratios as illustrated in Figs. 6-13 to 6-16. These figures show the contours at x/R = 0.2386. The 3D simulation result provides a detailed small scale visualization of the complex physical processes of two-phase flow undergoing mass transfer.

Contours of dynamic viscous dissipation show highest entropy production at the blade tip. The locally high production rate arises from the flow passing the highly curved surface causing a sudden velocity change and a high velocity gradient (see Fig.6-13). Contours shown in Fig.6-14 are turbulent dissipation resulting from mixture velocity fluctuation. The highest dissipation rate occurs near the tip of the blade and the hub area. The flow is perturbed at highly curved profile when passing the tip and trips flow turbulence, while near the hub the flow travels through a narrow channel formed by the rotating blades causing the formation of vortex.

The irreversibility due to the slip velocity between liquid and vapor phases is highest near the tip of blade where the velocity difference between the two phases develops rapidly. The contours in Fig. 6-15 show this entropy production term contributes less to total entropy production compared with previous two items. It should be noted that this term is exclusive in the drift-flux mixture model. In the case of a homogeneous turbulence model, the vapor and liquid phase velocities are assumed identical at same position. This model takes less computing time to obtain convergent results than the drift-flux mixture model especially for 3D rotating simulations.

The contours of entropy production due to cavitation are presented in Fig. 6-16. The energy dissipation near the tip of blade is significant. Also on the back of blade cavitation occurs, the dissipation rates have relatively high values. Although this irreversibility occurs only in the regions where the cavitation occurs, the local energy loss is greater than the mean viscous dissipation (see Figs. 6-13 and 6-16).

The total entropy production is the sum of the individual entropy production terms: mixture viscous dissipation, mixture turbulent work effect, diffusion stress effect, and

cavitation/phase change effect from interfaces. The total entropy production contours are plotted in Figs 6-17 to 6-20 to show the total entropy production with different advance ratios, which is defined here as the ratio between the distance the incoming flow passes through the propeller during one revolution, and the diameter of the propeller. The item is analogous to the angle of attack of NACA 4412 hydrofoil. It is observed that at the same location of section plane, x/R = 0.2386, the total entropy production depends on the angle of attack. At J=0.98, the propeller foil has the smallest advance ratio considered and the flow can pass through the channel formed by the two-blades with less disturbance; hence entropy production mainly stems from mean viscous dissipation while other three term are not dominant. At J=1.52, flow passes maximum the channel with highly disturbance, which causes intensive turbulence near the tip of blade and hub area.

6.7 Validation and Summary

Fluid flow and entropy production past a DTMB propeller model P5168 was simulated using the CFD and entropy production 3-D cavitation model approach developed in Chapter 5. Good agreement over a wide range advance ratio values was found between the flow results of the present study and the experimental data of Chesnakas and Jessup [117]. Entropy production terms (mixture viscous dissipation, mixture turbulent work effect, diffusion stress effect**,** cavitation/phase change effect from interfaces) and total entropy production were discussed in detail for x/R = 0.2386 and a number of advanced ratios. High entropy production rates were found at the blade tip and for some of the entropy production terms at the hub. The dominate entropy production term is the mixture turbulent work effect. The results showed that this model can predict

the energy dissipation for a 3-D rotating machine under two-phase flow, including cavitation flow.

For further validation of the model, additional computations were performed for various advanced ratios under at the experimental conditions of Chesnakas and Jessup [117]. The kinetic energy dissipation in the domain was obtained by verifying the energy loss. The integral values of the entropy production rate were compared with the kinetic energy loss. By calculating the irreversibility, the entropy production model for two-phase cavitation flow was applied based on the energy balance. The destroyed exergy and dissipated thermal energy were compared. They are listed in Table 6-2.

Table 6-2: Error list of entropy production

J	Energy balance [w]	Entropy integral [w]	Propeller torque [Nm]	Propeller rpm	Propeller power [w]	Irreversibility [w]	Error [%]
0.98	1.33E+04	3.34E+03	-78.7	1200	9.89E+03	3.41E+03	2.05
1.10	1.98E+04	4.23E+03	-101.2	1450	1.54 E+04	4.40E+03	3.86
1.27	1.29E+04	4.09E+03	-63.1	1300	8.59E+03	4.31E+03	5.10
1.52	6.34E+03	3.14E+03	-25	1150	3.01E+03	3.33E+03	5.71

In Table 6-2, the energy balance represents the difference of kinetic energy between the inlet and outlet. The kinetic energy from the flowing water can be calculated by the area integral of the mixture velocity at each boundary (inlet and outlet). The propeller torque is calculated by integrating the product of pressure acting on the blade surface and the distance from the rotation centerline. The amount of kinetic energy that the propeller absorbs from the flowing water can be calculated by multiplied the torque

by the propeller's rpm (constant). The irreversibility is the dissipated energy converted to internal energy from the kinetic energy.

The entropy production rate is integrated over the whole domain and it can be treated as such energy which cannot do useful work. The integral values of the entropy production rate were obtained by volume integration of Eq. (5.62). Validation of the entropy production model for two-phase cavitation flow for 3D application was performed based on an energy balance. The comparisons made between the destroyed exergy and dissipated thermal energy. We can see that this new formulation of entropy production for two-phase cavitation flow predicts a local loss with high precision. The errors for different cases were presented for an accuracy comparison. In addition, as expected, the regions near the tip of the blades yielded the highest rates of entropy production.

Chapter 7

Conclusions and summary

7.1 Conclusions

This present thesis has presented a novel mathematic new predictive model of entropy production for two-phase cavitation flows. The Eulerian averaged mixture model was derived for the two-phase flow based on the RANS equations. A Rayleigh-Plesset equation was modeled for the rate equation controlling vapor generation, condensation and growth of a gas bubble in a liquid. Based on the numerical solutions of the partial differential equations of the two-phase flow, the local irreversibility has been successfully determined using this model.

The thesis investigated laminar channel flow with analytical solutions of the flow field. This validation study addresses many key aspects of handling the turbulent single-phase flow and two-phase cavitation flow. The solution of the laminar case was used for validating the model of entropy production, which is derived from the Gibbs free energy combined with the Navier-Stokes equations. The method in this thesis is based on the energy balance method. A comparison of the integrated entropy production rate over the flow cross-section and the internal energy converted from kinetic energy showed that the method of energy balance is consistent with the energy conservation law and can be used for verification of the entropy production model. The calculated results of energy loss resulted in the same mathematical expression. The results indicated that the entropy model for laminar flow predicted local loss through validation by the energy balance method. The specific entropy can also be obtained by analytically solving the entropy transport equation. This method was also applied to turbulent channel flow.

To acquire an appropriate method of handling the fluctuating items in turbulent flow, the entropy production model for single-phase turbulent channel flow was investigated. The DNS solutions to the turbulent channel flow were used to verify the new formulations of entropy production for turbulent flows. Two different models of entropy production rate for turbulent flow were derived from different perspectives based on the energy equations and Gibbs free energy equation. The TVD model predicts that entropy production arises from dissipation because of the mean flow motion, as well as turbulence dissipation.

The RSS model of entropy production was also derived from the RANS equations. The entropy term involves the Reynolds shear dissipation resulting from the velocity fluctuation. It can be interpreted as the work done by the force $-\nabla(\overline{\mathbf{u}'\mathbf{u}'})$ in the streamwise direction and dissipated to thermal energy.The integral values of the entropy production rate were obtained by the integration of the flow cross-section. Validation of the models was performed based on an energy balance. The TVD model predicts local loss with higher precision than the RSS model.

The mean specific entropy was also obtained by integration. The results of the RSS model are consistent with the TVD model beyond the center area, but they have a sharp decrease when approaching the centerline, where the gradient of mean velocity tends toward zero. A comparison between two different models of entropy production for turbulent flow was presented. The errors for different models were presented for an accurate comparison. These models address the viscous layer and results outside of the layer. Both models slightly have under-estimated the irreversibility of the wall-bounded turbulent entropy production, as shown in Table 4-2. However, overall they provided

accurate predictions of the flow irreversibility, especially for center-line losses in the TVD model. The specific entropy for turbulent channel flow was also solved based on the DNS solutions.

The main contribution of this research is that the model has initially revealed the effects of cavitation and velocity difference between vapor and liquid phases on the entropy production rate for cavitation flow. The derivation of this entropy model is based on the two-phase mixture model. The model treats the liquid and vapor as one substance, eliminating the complexity of solving the inter-phase transport. The model was developed using an Eulerian time-averaged formulation. The RANS equations of this mixture model involve mixture velocity, vapor velocity, void fraction, and the slip velocity. At an arbitrary position in the domain, there exist two different velocities.

The entropy production model was derived from the mixture energy equation and Gibbs free energy. The model consists of four main items that contribute to the total kinetic energy dissipation. The mixture mean viscous loss exists but it is present in a different form. The gradient of mixture velocity and the mixture dynamic viscosity were introduced and formed the shear stress. This dissipation can be analogous to the single-phase viscous dissipation, but the dynamic viscosity in the mixture model is the function of void fraction.

The irreversibility due to the Reynolds shear stress, $-\rho\overline{\mathbf{u}'_m\mathbf{u}'_m}$, resulted from the mixture velocity fluctuation. This irreversibility can also be interpreted as the work done by the force $-\nabla(\overline{\mathbf{u}'_m\mathbf{u}'_m})$ in the streamwise direction and dissipated to thermal energy. It is comparable to the turbulent dissipation in a single-phase turbulent flow case.

The consequence of slip velocity caused energy loss as part of the entropy production, an irreversibility due to the slip velocity between liquid and vapor phases. It exists in a two-phase flow, but the mechanism of the physics still remains unclear. The loss is due to the fluid friction between two phases, much like the wall shear stress between the fluid and a solid wall, where the gradient of the velocity has a maximum value.

The last item of the irreversibility resulted from the effects of the energy source and the momentum sources from interfaces. This local loss can be described by the mathematical model without considering the interfacial mechanism because it has been time-averaged in a control volume. For cavitation flow, this item must include the effect of mass transfer because large-energy exchanges involve latent heat with a change of phase. This process converts kinetic energy into internal energy to compensate for the loss of latent heat. The energy dissipations because of the cavitation near the wall have considerable effect when the cavitation occurs.

The total entropy production was found by summarizing all of the four items. This entropy production model has been validated through numerical solutions for the cavitation flow around a standard hydrofoil of NACA 4412. This methodology is also based on an energy balance, the first law of thermodynamics. The total kinetic energy loss when the flow passes the domain of interest should be equal to the irreversibility determined by the model. The energy loss is first calculated by means of the difference between the inlet and the outlet of the domain. Then, the irreversibility is estimated by the integrated entropy production rate throughout the whole domain.

The CFD results of NACA 4412 were broadly validated against experimental data, including lift coefficient, drag coefficient, and momentum coefficient for different Reynolds numbers and angles of attack. The cavitation coefficients were also verified against the measured results. All the CFD results showed strong agreement with the experimental results.

The 3-D applications of this entropy model were also verified by investigating the performance of a P5168 propeller. The CFD data were validated against the measured results. The local loss of exergy in the domain of interest was studied by applying this entropy production model. The results showed that this model can predict the energy dissipation with high accuracy for a 3-D rotating machine under two-phase flow, including cavitation flow. It supported the theory that the entropy production of two-phase cavitating flow around the propeller can be correlated to the loss of propeller power output.

7.2 Recommendations for future research

Based on the cavitation entropy model, several further studies are suggested to improve the model. First, one could modify the current model by taking into account the change in temperature due to the dissipation of kinetic energy. When studying the P5168 propeller, an assumption was made that the domain of interest remains at a constant temperature because of the adiabatic process. This assumption is reasonable for hydro machinery research because the heat transfer is not dominant in the process. However, when studying a propeller mixer in a sealed container, the change in temperature must be taken into account. Research on this topic would have significance because heat transfer through an area of entropy production affects the performance of the system. This effect,

in turn, affects the entropy production. The temperature field varies in terms of both time and space, and the entropy changes with temperature. Because various entropy models for single-phase turbulent flow that take into account temperature fluctuation have been developed, one must have a strong grasp of which model should be applied to two-phase flow.

Second, the current theory that was derived from the Gibbs free energy can be refined and explored. The entropy model involves two notable items that have not been reported by others. The first is the dissipation due to the velocity difference between vapor and liquid phases. The mechanism of the energy loss still remains unclear. Unlike viscous friction in single-phase laminar flow, this "friction" force occurs between two phases. Because we adopted the mixture model for entropy derivation, the mixture media has its own properties, such as dynamic viscosity, density, and so on. Hence, no inter-phase boundary exists between vapor and liquid for the mixture model. This "friction" might be an additional feature to distinguish the real mixture (water and alcohol) and the model mixture (water and vapor/air). The latter exists only in flowing media and separates into two independent phases when it stops flowing. For these sorts of mixtures, the density difference between the two phases is very large, and the slip velocity has an important role in entropy production. Revealing the relationship between slip velocity and entropy production shows great potential for future research.

Third, this research was focused on the entropy production rate for cavitation flow, meaning that the phase change results only from cavitation, not heat transfer. However, the entropy model proposed in this dissertation offers a guideline for future research, suggesting body heating and mass transfer. The difficulty of introducing heat transfer and

mass transfer into the two-phase entropy model lies with handling the fluctuation of the temperature due to the turbulence. The mean entropy production due to the heat/mass transfer temperature needs to be expressed with mean temperature gradients and other fluctuating items.

References

[1] G. F. Naterer and J. A. Camberos, Entorpy Based Design and Analysis of Fluids Engineering Systems, Boca, Raton, London, New York: CRC Press, Taylor & Francis Group, 2008.

[2] K. D. Bailey, "Entropy Systems Theory," University of California, Los Angeles, CA, 2011.

[3] K. D. Bailey, Social Entropy Theory, Albany, NY: State University of New York Press, 1990.

[4] A. Farhang-Mehr and S. Azarm, "Entropy-Based Multi-Objective Genetic Algorithm for Design Optimization," *Structural and Multidisciplinary Optimization*, vol. 24, no. s00158-002-0247-6, p. 351–361, 2002.

[5] E. Mendoza, Reflections on the Motive Power of Fire – and other Papers on the Second Law of Thermodynamics by E. Clapeyron and R. Clausius, New York: Dover Publications, 1988.

[6] A. Bejan, Advanced Engineering Thermodynamics, Hoboken, NJ: Wiley, 2006.

[7] S. R. Groot and P. Mazur, Non-Equilibrium Thermodynamics, Dover Publications; Dover ed edition, 2011.

[8] S. Carnot, Reflections on the Motive Power of Fire, Gloucester: Peter Smith Publisher, 1992.

[9] R. Clausius, The Mechanical Theory of Heat, Charleston: Biblio Bazaar, 2008.

[10] U. Lucia, "Mathematical Consequences and Gyarmati's Principle in Rational Thermodynamics," *Il Nuovo Cimento*, vol. 10, no. B110, pp. 1227-1235, 1995.

[11] L. Boltzmann, Lectures on Gas Theory, New York: Dover Publications, 1995.

[12] E. Schrodinger, Statistical Thermodynamics, New Yoek: Dover Publications, 1989.

[13] H. S. Leff and A. F. Rex, Maxwell's Demon: Entropy, Information, Computing, Bristol: Adam-Hilger, 1990.

[14] U. Lucia, "Irreversibility, Entropy and Incomplete Information," *Physica A: Statistical Mechanics and its Applications*, vol. 388, no. 15, pp. 4025-4033, 2009.

[15] U. Lucia, "Statistical Approach of the Irreversible Entropy Variation," *Physica A: Statistical Mechanics and its Applications*, vol. 387, no. 14, pp. 3454-3460, 2008.

[16] I. Dincer, "Exergy and the Environment: A Global Perspective," *International Journal of Globe Energy*, vol. 15, no. 3/4, p. 363–374, 2001.

[17] M. A. Rosen and I. Dincer, "On Exergy and Environmental Impact," *International Journal of Energy Research*, vol. 21, no. 7, p. 643–654, 1997.

[18] E. T. Jaynes, "Probability Theory as Logic, in Maximum-Entropy and Bayesian Methods," *P.F. Fougére, Ed., Kluwer, Dordrecht*, pp. 1-16, 1991.

[19] J. S. Shiner, Entropy and Entropy Generation: Fundamentals and Applications

(Understanding Chemical Reactivity), New York: Springer, 2001.

[20] S. Watanabe, "Pattern Recognition as a Quest for Minimum Entropy," *Pattern Recognition,* vol. 13, pp. 381-387, 1981.

[21] K. Sasaki, "Constrained Nonlinear Method for Estimating Component Spectra from Multicomponent Mixtures," *Applied Optics,* vol. 22, pp. 3599-3603, 1983.

[22] J. N. Kanpur, Maximum Entropy Models in Science and Engineering, New Delhi: Wiley Eastern Ltd, 1993.

[23] H. Zhang, "Weighted Two-Band Target Entropy Minimization for the Reconstruction of Pure Component Mass Spectra: Simulation Studies and the Application to Real System," M.sc Thesis, National University of Singapore , Singapore , 2003.

[24] A. T. Waele, "Basic Operation of Cryocoolers and Related Thermal Machines," *Journal of Low Temperature Physics,* vol. 164, no. DOI 10.1007/s10909-011-0373-x, p. 179–236, 2011.

[25] E. Johannessen and S. Kjelstrup, "Minimum Entropy Production Rate in Plug flow Reactors: An Optimal Control Problem Solved for SO2 Oxidation," *Energy,* vol. 29, p. 2403–2423, 2004.

[26] A. Røsjorde, S. Kjelstrup, E. Johannessen and R. Hansen, "Minimizing the Entropy Production in a Chemical Process for Dehydrogenation of Propane," *Energy,* vol.

32, p. 335–343, 2007.

[27] J. N. Kapur and H. K. Kesavan, Entropy Optimization Principles with Applications, Academic Press, CA: San Diego, 1992.

[28] A. Bejan, Entropy Generation Minimization: The Method of Thermodynamic Optimization of Finite-Size Systems and Finite-Time Processes, Boca Raton: CRC Press, 1995.

[29] D. J. Moorhouse and C. M. Hoke, "Thermal Analysis of Hypersonic Inlet Flow With Exergy-Based Design Methods," *International Journal of Thermodynamics,* vol. 5, no. 4, pp. 161-168, 2002.

[30] I. Dincer and M. Rosen, "Exergy as a Driver for Achieving Sustainability," *International Journal of Green Energy,* vol. 1, no. 1, pp. 1-19, 2004.

[31] A. Bejan, Advanced Engineering Thermodynamics, 2nd ed., New York: Wiley, 1997.

[32] M. A. Rosen and I. Dincer, "Effect of Varying Dead-State Properties on Energy and Exergy Analyses of Thermal Systems," *International Journal of Thermal Sciences,* vol. 43, no. 2, p. 121–133, 2004.

[33] G. F. Naterer and J. A. Camberos, "Entropy and the Second Law Fluid Flow and Heat Transfer Simulation," *JOURNAL OF THERMOPHYSICS AND HEAT TRANSFER,* Vols. Vol. 17, No. 3 , July–September, 2003.

[34] J. A. Camberos, "On the Construction of Entropy Balance Equations for Arbitrary Thermophysical Processes," *AIAA*, pp. 2001-0815, 2001.

[35] J. A. Camberos, "Alternative Interpretation of Work Potential in Thermophysical Processes," *Journal of Thermophysics and Heat Transfer*, vol. 14, no. 2, p. 177–185, 2000.

[36] V. P. Singh, Entropy-Based Parameter Estimation in Hydrology, New York: Springer, 1998.

[37] J. Cervantes and F. Solorio, "Entropy Generation in a Plane Turbulent Oscillating Jet," *International Journal of Heat and Mass Transfer*, vol. 45, no. 15, pp. 3125-3129, July 2002.

[38] E. Johannessen, L. Nummedal and S. Kjelstrup, "Minimizing the entropy production in heat exchange," *International Journal of Heat and Mass Transfer*, vol. 45, no. 13, p. 2649–2654, June, 2002.

[39] A. Poulikakos and A. Bejan, "Fin Geometry for Minimum Entropy Generation in Forced Convection," *Journal of Heat Transfer*, vol. 104, pp. 616-623, November 1982.

[40] S. M. Zubair, P. V. Kadaba and R. B. Evans, "Second Law-Based Thermoeconomic Optimization of Two-Phase Heat Exchangers," *Journal of Heat Transfer*, vol. 109, p. 287–294, 1987.

[41] E. Sciubba, "Calculating Entropy with CFD," *Mech. Eng.(ASME Mechanical Engineering)*, vol. 119, no. 10, pp. 86-88, 1997.

[42] G. Natalini and E. Sciubba, "Minimization of Local Rates of Entropy Production in the Design of Air-Cooled Gas Turbine Blades," *Journal of Engineering for Gas Turbines and Power*, vol. 121, no. 0742-4795, pp. 466-475, 1999.

[43] S. M. Kresta and P. E. Wood, "The Flow Field Produced By a Pitched Blade Turbine: Characterization of the Turbulence and Estimation of the Dissipation Rate," *Chemical Engineering Science*, vol. 48, pp. 1761-1774, 1993.

[44] Y. Demirel, "Irreversibility Profiles in a Circular Couette Flow of Temperature Dependence Materials," *International Communications in Heat and Mass Transfer*, vol. 26, pp. 75-83, 1999.

[45] A. Z. Sahin, "Entropy Generation in Turbulent Liquid Flow through a Smooth Duct Subjected to Constant Wall Temperature," *International Journal of Heat and Mass Transfer*, vol. 43, p. 1469–1478, 2000.

[46] A. Z. Sahin, "Entropy Generation and Pumping Power in a Turbulent Fluid Flow through a Smooth Pipe Subjected to Constant Heat Flux," *International Journal of Exergy*, vol. 2, pp. 314-321, 2002.

[47] C. H. Cheng, W. P. Ma and W. H. Huang, "Numerical Predictions of Entropy Generation for Mixed Convective Flows in a Vertical Channel with Transverse Fin Arrays," *International Journal of Heat and Mass Transfer*, vol. 21, p. 519–530,

1994.

[48] A. C. Baytas, "Entropy Generation for Natural Convection in an Inclined Porous Cavity," *International Journal of Heat and Mass Transfer,* vol. 43, p. 2089–2099, 2000.

[49] S. Mahmud and R. A. Fraser, "Analysis of Entropy Generation inside Concentric Cylinder Annuli with Relative Rotation," *International Journal of Thermal Sciences,* vol. 42, p. 513–521, 2002.

[50] O. Adeyinka and G. F. Naterer, "Entropy Based Metric for Component Level Energy Management: Application to Diffuser Performance," *International Journal of Energy Research,* vol. 29, no. 11, p. 1007–1024, 2005.

[51] J. Moore and J. G. Moore, "Entropy Production Rates from Viscous Flow Calculations, Part I. A Turbulent Boundary Layer Flow," in *ASME Paper 83-GT-70，ASME Gas Turbine Conference,* Phoenix，AZ, 1983.

[52] J. Moore and J. G. Moore, "Entropy Production Rates from Viscous Flow Calculations Part II. Flow in a Rectangular Elbow.," in *American Society of Mechanical Engineers Gas Turbine Conference, ASME Paper 83-GT-71*, Phoenix, 1983.

[53] M. K. Drost and M. D. White, "Numerical Predictions of Local Entropy Generation in an Impinging Jet," *ASME J. Heat Transfer,* vol. 113, p. 823–829, 1991.

[54] J. Kramer-Bevan, "A Tool for Analysing Fluid Flow Losses," M.Sc. thesis, University of Waterloo, Ontario, Canada, 1992.

[55] O. B. Adeyinka, ""Entropy and Second Law Optimization in Computational Thermofluids with Laser Based Measurements"," M.Sc. thesis, University of Manitoba, Winnipeg, 2002.

[56] T. J. R. Hughes, M. Mallet and L. P. Franca, "Entropy Stable Finite Element Methods for Compressible Fluids: Application to High Mach Number Flows with Shocks , Finite Element Methods for Nonlinear Problem," in *Europe-US Symposium*, Trondheim, Norway, 1985.

[57] R. A. Cox and B. M. Argrow, "Entropy Production in Finite-Difference Schemes," *AIAA Journal*, vol. 31, no. 1, pp. 210-211, 1992.

[58] G. F. Naterer, "Constructing an Entropy-Stable Upwind Scheme for Compressible Fluid Flow Computations," *AIAA Journal*, vol. 37, no. 3, p. 303–312, 1999.

[59] K. E. Jansen, "The Role of Entropy in Turbulence and Stabilized Finite Element Methods," Ph.D. Thesis, Stanford University, CA, 1993.

[60] G. Hauke, "A Unified Approach to Compressible and Incompressible Flows and a New Entropy-Consistent Formulation of the k-epsilon Model," Ph.D. Thesis, Stanford University, CA, 1995.

[61] T. H. Ko and C. S. Cheng, "Numerical Investigation on Developing Laminar

Forced Convection and Entropy Generation in a Wavy Channel," *International Communications in Heat and Mass Transfer*, vol. 34, no. 8, pp. 924-933, October 2007.

[62] J. Herpe, D. Bougeard, S. Russeil and M. Stanciu, "Numerical Investigation of Local Entropy Production Rate of a Finned Oval Tube With Vortex Generators," *International Journal of Thermal Sciences*, vol. 48, no. 5, pp. 922-935, May 2009.

[63] T. H. Ko, "Numerical Investigation on Laminar Forced Convection and Entropy Generation in a Curved Rectangular Duct With Longitudinal Ribs Mounted on Heated Wall," *International Journal of Thermal Sciences*, vol. 45, no. 4, pp. 390-404, April 2006.

[64] F. Kock and H. Herwig, "Local Entropy Production in Turbulent Shear Flows: A High-Reynolds Number Model With Wall Functions," *International Journal of Heat and Mass Transfer*, vol. 47, no. 10-11, pp. 2205-2215, May 2004.

[65] P. D. Lax, "Weak Solutions of Nonlinear Hyperbolic Equations and Their Numerical Computation," *Communications on Pure and Applied Mathematics*, vol. 7, p. 159–193, 1954.

[66] P. D. Lax, "Shock Waves and Entropy," in *Contributions to Non-Linear Functional Analysis*, New York, Academic Press, 1971, pp. 603-634.

[67] C. Y. Borth and B. M. Argrow, "Evaluation of Entropy Production and Numerical Entropy Change in Flow Field Solutions," *HTD, American Society of Mechanical*

Engineers, vol. 191, 1991.

[68] J. M. Herard, "Entropy Consistent Splitting Algorithms for Some Turbulence Compressible Models," *AIAA*, p. 2650, 1998.

[69] C. Charach and I. L. Rubinstein, "On Entropy Generation in Phase Change Heat Conduction," *Journal of Applied Physics*, vol. 66, no. 9, p. 4053–4061, 1989.

[70] G. F. Naterer, "Applying Heat-Entropy Analogies with Experimental Study of Interface Tracking in Phase Change Heat Transfer," *International Journal of Heat and Mass Transfer*, vol. 44, no. 15, p. 2917–2932, 2001.

[71] S. X. Chu and L. H. Liu, "Entropy Generation Analysis of Two-Dimensional High-Temperature Confined Jet," *International Journal of Thermal Sciences*, vol. 48, no. 5, pp. 998-1006, May 2009.

[72] C. L. Iandoli, E. Sciubba and N. Zeoli, "The Computation of the Entropy Generation Rate for Turbomachinery Design Applications: Some Theoretical Remarks and Practical Examples," *International Journal of Energy Technology and Policy*, vol. 6, no. 1-2, pp. 64-95, 2008.

[73] J. D. Denton, "Entropy Generation in Turbomachinery Flows," in *7th Cliff Garrett Turbomachinery Award Lectures*, Long Beach, 1990.

[74] D. M. Paulus, R. A. Gaggioli and W. R. Dunbar, "Entropy Production as a Predictive Performance Measure for Turbomachinery," *Journal of Engineering for*

Gas Turbines and Power, vol. 123, no. 1, p. 17, January 2001.

[75] C. L. Iandoli and E. Sciubba, "3-D Numerical Calculation of the Local Entropy Generation Rates in a Radial Compressor Stage," *International Journal of Thermodynamics,* vol. 8, no. 2, pp. 83-94, June 2005.

[76] R. Courant, K. O. Friedrichs and H. Lewy, "On the Partial Difference Equations of Mathematical Physics," *IBM Journal of Research and Development,* vol. Vol. 11, p. pp. 215–234, 1967.

[77] G. F. Naterer and G. E. Schneider, "Use of the Second Law for Articial Dissipation in Compressible Flow Discrete Analysis," *Journal of Thermophysics and Heat Transfer,* vol. 8, no. 3, pp. 500-506, 1994.

[78] O. B. Adeyinka and G. F. Naterer, "Modeling of Entropy Production in Turbulent Flows," *Journal of Fluids Engineering,* vol. 126, no. 6, pp. 893-899, Nov., 2004.

[79] F. Kock and H. Herwig, "Entropy Production Calculation for Turbulent Shear Flows and their Implementation in CFD Codes," *International Journal of Heat and Fluid Flow,* vol. 26, no. 4, pp. 672-680, August 2005.

[80] C. Dumouchel, "A New Formulation of the Maximum Entropy Formalism to Model Liquid Spray Drop-Size Distribution," *Particle & Particle Systems Characterization,* vol. 23, no. 6, pp. 468 - 479, April 2007.

[81] D. M. McEligot, E. J. Walsh and E. Laurien, "Entropy Generation in the Viscous Layer of a Turbulent Channel Flow," in *5th International Symposium on*

Turbulence, Heat and Mass Transfer, 2006.

[82] G. F. Naterer, "Predictive Entropy Based Correction of Phase Change Computations with Fluid Flow—Part 1: Second Law Formulation," *Numerical Heat Transfer*, vol. 37, no. 4, pp. 393-414, 2000.

[83] M. L. Merriam, An Entropy-Based Approach to Nonlinear Stability, Stanford, CA: Ph.D. Dissertation, Dept. of Mechanical Engineering, Stanford University, 1989.

[84] C. S. Lee, "Prediction of Steady and Unsteady Performance of Martin Propeller with or Without Cavitation by Numerical Lifting Surface Theory," Ph.D. dissertation, MIT, Cambridge, MA, 1979.

[85] S. H. Rhee, T. Kawamura and H. Li, "Propeller Cavitation Study Using an Unstructured Grid Based Navier-Stoker Solver," *Journal of Fluids Engineering*, vol. 127, no. 5, pp. 986-994, September 2005.

[86] J. W. Lindau, D. A. Boger, R. B. Medvitz and R. F. Kunz, "Propeller Cavitation Breakdown Analysis," *Journal of Fluids Engineering*, vol. 127, no. 5, pp. 995-1002, September 2005.

[87] R. B. Medvitz, R. F. Kunz, D. A. Boger, J. W. Lindau and A. M. Yocum, "Performance Analysis of Cavitating Flow in Centrifugal Pumps Using Multiphase CFD," *Journal of Fluids Engineering*, vol. 124, no. 2, pp. 377-383, June 2002.

[88] S. Whitaker, The Method of Volume Averaging, New York: Springer, 1999.

[89] C. Kawakita, R. Takashima and K. Sato, "CFD on Cavitation around Marine Propellers with Energy-Saving Devices," *Mitsubishi Heavy Industries Technical Review*, vol. 49, no. 1, 2012.

[90] A. K. Singhal, M. M. L. H. Y. Athavale and Y. Jiang, "Mathematical Basis and Validation of the Full Cavitation Model," *ASME, Journal of Fluids Engineering*, vol. 124, pp. 617-624, 2002.

[91] M. M. Athavale, H. Y. Li, Y. Jiang and A. K. Singhal, "Application of the Full Cavitation Model to Pumps and Inducers," *International Journal of Rotating Machinery*, vol. 8, no. 1, pp. 45-56, 2002.

[92] N. A. Zuber and J. Findlay, "Average Volumetric Concentration in Two-Phase Flow Systems," *Journal of Heat Transfer*, vol. 87, p. 453 – 468, 1965.

[93] M. Islii, Thermo Fluid Dynamic Theory of Two Phase Flow, Paris: Eyrolles, 1975.

[94] S. Y. Lee, T. Hibiki and M. Ishiib, "Formulation of Time and Volume Averaged Two-Fluid Model Considering Structural Materials in a Control Volume," *Nuclear Engineering and Design*, vol. 239, no. 1, pp. 127-139, 2009.

[95] M. Ishii, "One-Dimensional Drift-Flux Model and Constitutive Equations for Relative Motion between Phases in Various Two-Phase Flow Regimes," Argonne National Laboratory, Argonne, Illinois, 1977.

[96] M. Manninen and V. Taivassalo, "On the Mixture Model for Multiphase Flow,"

VTT Energy, vol. 288, 1996.

[97] T. Hibiki and M. Ishii, "One-Dimensional Drift-Flux Model and Constitutive Equations for Relative Motion between Phases in Various Two-Phase Flow Regimes," *International Journal of Heat and Mass Transfer*, vol. 46, no. 25, pp. 4935-4948, December 2003.

[98] O. J. Simonin, "Eulerian Formulation for Particle Dispersion in Turbulent Two Phase Flows," in *5th Workshop on Two Phase Flow Predictions*, Kernforschungsanlage Julich, 1990.

[99] L. Schiller and Z. Naumann, "A Drag Coefficient Correlation," *Z. Ver. Deutsch. Ing*, vol. 77, no. 318, 1935.

[100] R. Clift, J. R. Grace and M. E. Weber, Bubbles, Drops, and Particles, London: Academic Press, 1978.

[101] S. L. Passman, J. W. Nunziato and E. K. Walsh, A Theory of multiphase Mixture, Rational Thermodynamics, New York: Springer-Verlag, 1984.

[102] A. Malhotra and S. S. Kang, "Turbulent Prandtl Number in Circular Pipes," *Int. J. Heat and Mass Transfer*, vol. 27, pp. 2158-2161, 1984.

[103] C. E. Brennen, Cavitation and Bubble Dynamics, Oxford University Press, 1995.

[104] D. R. Gaskell, Introduction to the Thermodynamics of Materials, New York: Tyler & Francis Group, LLC, 2008.

[105] B. R. Munson, D. F. Young, T. H. Okiishi and W. W. Huebsch, Fundamentals of Fluid Mechanics, Wiley, 2008.

[106] J. Scott and M. Julian, An Introduction to Turbulent Flow, Cambridge University Press, June 26, 2000.

[107] K. Iwamoto, "Database of Fully Developed Channel Flow," Department of Mechanical Engineering, The University of Tokyo, Tokyo, 2002.

[108] G. F. Naterer, Heat Transfer in Single and Multiphase Systems, Boca Raton, FL: CRC Press, 2002.

[109] K. Watanabe, H. Kui and I. Motosu, "Drag of a Sphere in Dilute Polymer Solutions in High Reynolds Number Range," *Rheologica Acta,* vol. 37, no. 4, pp. 328-335, 1998.

[110] K. Akita and F. Yoshida, "Bubble Size, Interfacial Area, and Liquid-Phase Mass Transfer Coefficient in Bubble Columns," *Industrial and Engineering Chemistry Process Design and Development,* vol. 13, pp. 84-91, 1974.

[111] G. Kocamustafaogullari and M. Ishii, "Foundation of the Interfacial Area Transport Equation and its Closure Relations," *International Journal of Heat and Mass Transfer,* vol. 38, p. 481–493, 1995.

[112] F. R. Menter, "Zonal Two Equation k-omiga Turbulence Models for Aerodynamic Flows," in *AIAA Paper #93-2906, 24th Fluid Dynamics Conference*, July 1993.

[113] F. R. Menter, "Two-Equation Eddy-Viscosity Turbulence Models for Engineering Applications," *AIAA Journal*, vol. 32, no. 8, pp. 1598-1605, 1994.

[114] R. T. Knapp and J. W. Daily, "Force and Cavitation Characteristics of the NACA 4412 Hydrofoil," California institute of technology hydraulic machinery laboratory, Pasadena, CA, 1944.

[115] Y. T. Shen and P. E. Dimotakis, "The Influence of Surface Cavitation on Hydrodynamic Forces," in *Proc. 22nd American Towing Tank Conference*, St. John's, Canada, 1989.

[116] ANSYS, "ANSYS CFX-Solver Theory Guide, Release 14.5," Canonsburg, PA, 2012.

[117] C. J. Chesnakas and S. D. Jessup, "Cavitation and 3-D LDV Tip Flow Field Measurements of Propeller 5168," Hydromechanics Directorate Research and Development Report, Carderock Division,Naval Surface Warfare Center, May 1998.

[118] M. Morgut and E. Nobile, "Comparison of Hexa-Structured and Hybrid-Unstructured Meshing Approaches for Numerical Prediction of the Flow Around Marine Propellers," in *First International Symposium on Marine Propulsors*, Trondheim, Norway, June 2009.

[119] "Aeronautics and Astronautics Lecture Notes," MIT Open Course, Cambridge, MA, 2005.

[120] Ansys, "Ansys ICEM CFD 12.1 User Manual," Ansys Inc., Canonsburg, PA, 2009.